Analysis of Lattice Boltzmann Method for Turbulent Flow Simulation on Multi-core GPU Architecture

A Thesis submitted by
Alankar Agarwal

in partial fulfillment of the requirements for the award of the degree of
Doctor of Philosophy

॥ त्वं ज्ञानमयो विज्ञानमयोऽसि ॥

Indian Institute of Technology Jodhpur
Center for Biologically Inspired System Science
Department of Mechanical Engineering
September 2021

Declaration

I hereby declare that the work presented in this Thesis titled *"Analysis of Lattice Boltzmann Method for Turbulent Flow Simulation on Multi-core GPU Architecture"* submitted to the Indian Institute of Technology Jodhpur in partial fulfilment of the requirements for the award of the degree of Doctor of Philosophy, is a bonafide record of the research work carried out under the joint supervision of *Dr. B.Ravindra* and *Dr. Akshay Prakash.* The contents of this Thesis in full or in parts, have not been submitted to, and will not be submitted by me to, any other Institute or University in India or abroad for the award of any degree or diploma.



Alankar Agarwal
P14BS001

Certificate

This is to certify that the Thesis titled *"Analysis of Lattice Boltzmann Method for Turbulent Flow Simulation on Multi-core GPU Architecture"*, submitted by *Alankar Agarwal (P14BS001)* to the Indian Institute of Technology Jodhpur for the award of the degree of *Doctor of Philosophy*, is a bonafide record of the research work done by him under my supervision. To the best of my knowledge, the contents of this report, in full or in parts, have not been submitted to any other Institute or University for the award of any degree or diploma.



Dr. B. Ravindra
Ph.D.Thesis Supervisor



Dr. Akshay Prakash
Ph.D.Thesis Co-Supervisor

Abstract

The present thesis explores the applicability of the lattice Boltzmann Method (LBM) to validate the turbulent flow simulation in the various complex flow domains. LBM in recent years has emerged as an alternative Computational Fluid Dynamics (CFD) approach other than traditional Navier-Stokes (NS) solvers. The method is based on the discrete numerical approach and solves the kinetic equations to discretize the fluid domain. The fluid in LBM is defined as the particle distribution functions. The computational domain of the fluid flow represents the Eulerian grid nodes, each of which consists of a lattice structure. The lattice structure is comprised of the particle distribution functions, which are restricted to move in specific directions.

The research work mainly focuses on modeling large turbulent structures on a grid-scale for high Reynolds number flows with the Large Eddy Simulation (LES) model in the frame of LBM. The turbulent motions smaller than grid size are resolved using the popular Smagorinsky subgrid-scale (SGS) model. The study also gives special attention to investigate the effect of the different discrete velocity models of LBM and boundary conditions on the turbulent flow behavior. The results are presented for various turbulent statistics, including phase-averaged velocities, root-mean-square (RMS) velocity, Reynolds stresses, and turbulent kinetic energy (TKE).

Moreover, another important work reported in the thesis is the turbulent flow simulation in the stirred tank reactor equipped with dual-Rushton impellers. The study shows the LBM capability to simulate the turbulent flow in such complex geometry. The work also investigates the effect of baffles on the flow hydrodynamics at different impeller clearance. The study compares the results at different impeller clearance in the presence and absence of baffles. The obtained results are validated with the experimental data available in the literature.

The thesis work also presents the efficiency of the LBM algorithm on multi-core computer hardware. A highly parallelized computer code was developed using Compute Unified Device Architecture (CUDA) programming language to execute on Graphics Processing Units (GPUs) parallel platform. The computational performance of the algorithm is measured from the Millions Lattice Updates Per Second (MLUPS) parameter. This is obtained from the simulation run-time of the code on the multi-cores of the GPU. The computational scaling of the code is addressed in the study by executing the code at varying numbers of cores. The three-dimensional (3-D) approach of the domain decomposition is employed to increase the scalability.

In conclusion, the research studies performed in the present thesis show the LBM viability as a feasible tool for the turbulent flow simulation at high Reynolds numbers with good accuracy and high computational efficiency for various simple to complex flow domains.

…

Acknowledgment

It has been an incredible experience while pursuing a doctoral degree at the Indian Institute of Technology Jodhpur (IITJ). I have been fortunate to share this experience with many people and express a few words of thanks and gratitude for them.

First of all, I thank my Ph.D. Thesis Supervisors, *Dr. B. Ravindra*, and *Dr. Akshay Prakash*, for introducing me to the area of lattice Boltzmann Method (LBM) and its applications. In the process, I have learnt about the problems associated with turbulent flow, and fluid-structure interaction. I am grateful to them for their help and patience and for constantly reminding me to be perfect in the little things that I do each day. Also, I am indebted to the Members of the Doctoral Committee, *Dr. Anand Krishnan Plappally*, *Dr. Sudipto Mukhopadhyay*, and *Dr. Gaurav Bhatnagar*, for their enthusiastic and continued guidance during the research work. I thank *Dr. Laltu Chandra* for his valuable reviews to my work during his stay at IIT Jodhpur.

Further, I am thankful to the Director of IIT Jodhpur for providing such excellent facilities and making my stay at the Institute comfortable and fruitful. I would also like to thank the Department of Mechanical Engineering for providing the research facilities. I am also thankful to the faculty members of the department who were always supporting and helping. Also, I would like to thank all the staff members of the department for providing all sorts of support during my research work. I am grateful to the Office of Academics and Office of Student for their continuous help and support. I am also grateful to the Ministry of Education (MoE), India, for providing the necessary funding and support to carry out this research work.

I wish to give my special thanks to my seniors *Dr. Vikas Pratap Singh*, and *Dr. Dharmesh Kumar* for their continuous support, suggestions, and for helping me get through the difficult times through this entire journey. I would like to give my heartfelt thanks and appreciation to my friends *Gurveer Singh*, *Ankit Agarwal*, *Amrik Singh*, *Abhishek Sahu*, *Tushar Shankar Shinde*, *Ram Niwas Verma*, and *Aniket Dilip Monde* for listening to me and sometimes tolerating me over the past few years.

I acknowledge the Indian Institute of Technology Kharagpur (IIT KGP) administration for my pleasant stay during my visit to IIT KGP. I am also thankful to all my friends and lab-mates in the Department of Aerospace Engineering, IIT KGP, *Animesh Bhowmik*, *Chandan Kumar Sidhant*, *Parth Thakar*, *Hardik Bhavsar*, and *Apurva Raj* for all the discussions in the lab, or at tea-points, and for sharing beautiful moments.

At this moment of accomplishment, I thank all my well-wishers who have directly or indirectly contributed to my work. I am grateful to my late grandmother for all her blessings and for all the important lessons she taught me to make the right decisions in life. I owe my deep sense of gratitude to my parents, *Smt. Uma Agarwal* and *Shri Komeshwar Dayal Agarwal* for their day-night efforts, their sacrifices for providing me higher education, and for their relentless belief in me. I am highly thankful for the confidence and the inspiration I have received from my sister, *Mrs. Prerana Agarwal*, and my brother, *Mr. Rajat Agarwal*. I acknowledge and express my sincere gratitude to my brother-in-law, *Mr. Arpit Goel*, for being a part of my family and always stand with me during my tough times. I am also thankful to my wife, *Mrs. Dhawal Gupta*, for her unconditional love and trust. In the end, I thank the biggest to *Baba Trivati Nath*, who was always there to listen, to care, and to help me in every situation irrespective of my little knowledge.

Alankar Agarwal
Ph.D. Student

Contents

page

Abstract i
Acknowledgements iii
Contents v
List of Figures vii
List of Tables viii
List of Symbols xiii
List of Abbreviations xv

Chapter 1: Introduction 1
1.1 Background 1
1.2 Research Motiovation 2
1.3 Research Objective and and Contributions 4
1.4 Thesis Layout 5

Chapter 2: Literature Survey 7
2.1 The History of LBM 7
2.2 Collision Models of LBM 8
2.3 LBM in Turbulence Modeling 8
2.3.1 Study of Turbulent Flow Simulation over Bluff body 8
2.3.2 Study of Stirred Tank Reactor Simulation 9
2.4 Issue and Challenges 11
2.5 Summary 13

Chapter 3: Methodology 15
3.1 Simulation Procedure 15
3.1.1 Single-Relaxation-Time (SRT) model 15
3.1.2 LES Turbulent Model in LBM 17
3.2 Boundary Conditions 19
3.2.1 On-site Velocity Boundary Condition 19
3.2.2 Bounce-Back Boundary Conditions 28
3.2.2.1 Full way bounce-back 28
3.2.2.2 Half way bounce-back 29
3.2.2.3 Modified bounce-back 30
3.2.3 Free-Slip Boundary Condition 30
3.2.4 Immersed Boundary Method 30
3.3 GPU Programming 32
3.3.1 Architecture Details of NVIDIA Tesla GP100 GPU 32
3.3.2 Structure of CUDA Programming 33
3.3.3 LBM implementation on GPU cluster 35
3.4 Summary 35

Chapter 4: Turbulent Flow Simulation over a Bluff Body 37
4.1 Simulation Domain and Flow Conditions 37
4.2 Results and Discussion 38
4.2.1 Effect of Discrete Velocity Models of LBM 38
4.2.2 Effect of Boundary Conditions 43
4.3 Summary 48

Chapter 5: Effect of Baffles on the Flow Hydrodynamics of Dual-Rushton Turbine Stirred Tank Bioreactor 49
5.1 Flow System 49
5.2 Simulation Methodology 50
5.3 Aspects of Numerical Setup 51
5.4 Results and Discussion 51
5.4.1 Instantaneous Flow Field 51
5.4.2 Phase-Averaged Flow Field 52
5.4.3 Turbulent Kinetic Energy 58
5.5 Summary 60

Chapter 6: Conclusions and Future Recommendations 61
6.1 Conclusions 61
6.1.1 Effect of Discrete Velocity Models 61
6.1.2 Effect of boundary conditions 61
6.1.3 Effect of baffles on flow hydrodynamics of stirred tank reactor 62
6.2 Recommendations for Future Works 62

References 65

Appendix A: Knowledge Dissemination 71
A1 International Journal 71
A2 Book Chapter 71
A3 Conference Proceedings 71
A4 Solver Development 71

Appendix B: Grid Independence Study 73
B1 Turbulent Flow over Bluff Body 73
B2 Fluid Flow Simulation in Stirred Tank Reactor 73

List of Figures

Figure	*Title*	*page*
3.1	Lattice structure of (a) D_2Q_9, (b) D_3Q_{15}, (c) D_3Q_{19}, and (d) D_3Q_{27} discrete velocity models.	16
3.2	Schematic representation of flow in 3D square duct	19
3.3	2D representation of the full way bounce-back method before (left) and after (right) streaming process.	29
3.4	2D representation of the half way bounce-back method	29
3.5	2D representation of the free-slip boundary condition before (left) and after (right) streaming process.	30
3.6	Illustration of immersed boundary method.	31
3.7	Architecture of Tesla GP100.	33
3.8	Streaming Multiprocessor.	33
3.9	Illustration of CUDA programming model in 3D.	34
4.1	Schematic representation of the flow domain.	38
4.2	Flow behavior of instantaneous streamwise velocity for (a) D_3Q_{15}, (b) D_3Q_{19}, and (c) D_3Q_{27} velocity models.	39
4.3	Centerline distribution of mean streamwise velocity (red plus : D_3Q_{15}, green asterisk : D_3Q_{19}, blue open circle : D_3Q_{27}, open triangle : Kim *et al.* [2004], filled square: Nakagawa *et al.* [1999]).	40
4.4	Profiles of mean streamwise velocity (red plus : D_3Q_{15}, green asterisk : D_3Q_{19}, blue open circle : D_3Q_{27}, open triangle : Kim *et al.* [2004], filled square: Nakagawa *et al.* [1999]) : (a) x^*/d = 1.0, (b) x^*/d = 3.5, (c) x^*/d = 6.0, (d) x^*/d = 8.5.	40
4.5	Profiles of mean normal velocity (red plus : D_3Q_{15}, green asterisk : D_3Q_{19}, blue open circle : D_3Q_{27}, open triangle : Kim *et al.* [2004], filled square: Nakagawa *et al.* [1999]) : (a) x^*/d = 1.0, (b) x^*/d = 3.5, (c) x^*/d = 6.0, (d) x^*/d = 8.5.	41
4.6	Profiles of RMS streamwise velocity fluctuations (red plus : D_3Q_{15}, green asterisk : D_3Q_{19}, blue open circle : D_3Q_{27}, open triangle : Kim *et al.* [2004], filled square: Nakagawa *et al.* [1999]) : (a) x^*/d = 1.0, (b) x^*/d = 3.5, (c) x^*/d = 6.0, (d) x^*/d = 8.5.	41
4.7	Profiles of RMS normal velocity fluctuations (red plus : D_3Q_{15}, green asterisk : D_3Q_{19}, blue open circle : D_3Q_{27}, open triangle : Kim *et al.* [2004], filled square: Nakagawa *et al.* [1999]) : (a) x^*/d = 1.0, (b) x^*/d = 3.5, (c) x^*/d = 6.0, (d) x^*/d = 8.5..	42
4.8	Profiles of Reynolds shear stress (red plus : D_3Q_{15}, green asterisk : D_3Q_{19}, blue open circle : D_3Q_{27}, open triangle : Kim *et al.* [2004], filled square: Nakagawa *et al.* [1999]) : (a) x^*/d = 1.0, (b) x^*/d = 3.5, (c) x^*/d = 6.0, (d) x^*/d = 8.5.	42
4.9	GPU performance of discrete velocity.	44
4.10	Centerline distribution of mean streamwise velocity (asterisk : BB, open circle : IB, open triangle : Kim *et al.* [2004], filled square : Nakagawa *et al.* [1999]).	45
4.11	Profiles of mean streamwise velocity (asterisk : BB, open circle : IB, open triangle : Kim *et al.* [2004], filled square : Nakagawa *et al.* [1999]) : (a) x^*/d = 1.0, (b) x^*/d = 3.5, (c) x^*/d = 6.0, (d) x^*/d = 8.5.	45
4.12	Profiles of mean normal velocity (asterisk : BB, open circle : IB, open triangle : Kim *et al.* [2004], filled square : Nakagawa *et al.* [1999]) : (a) x^*/d = 1.0, (b) x^*/d = 3.5, (c) x^*/d = 6.0, (d) x^*/d = 8.5.	45

4.13 Profiles of RMS streamwise velocity fluctuations (asterisk : BB, open circle : IB, open triangle : Kim *et al.* [2004], filled square : Nakagawa *et al.* [1999]) : (a) x^*/d = 1.0, (b) x^*/d = 3.5, (c) x^*/d = 6.0, (d) x^*/d = 8.5. 46

4.14 Profiles of RMS normal velocity fluctuations (asterisk : BB, open circle : IB, open triangle : Kim *et al.* [2004], filled square : Nakagawa *et al.* [1999]) : (a) x^*/d = 1.0, (b) x^*/d = 3.5, (c) x^*/d = 6.0, (d) x^*/d = 8.5. 46

4.15 Profiles of Reynolds shear stress (asterisk : BB, open circle : IB, open triangle : Kim *et al.* [2004], filled square : Nakagawa *et al.* [1999]) : (a) x^*/d = 1.0, (b) x^*/d = 3.5, (c) x^*/d = 6.0, (d) x^*/d = 8.5. 46

5.1 Schematic representation of the flow domain 50

5.2 Flow Patterns in the stirred tank reactor with dual-Rushton turbines a) Parallel flow, b) Merging flow, and c) Diverging flow for Case 1, Case 2, and Case 3 respectively in Table 5.1. 52

5.3 Instantaneous velocity magnitude contour at upper impeller location for Case 1: (a) with baffles, (b) without baffles. 52

5.4 Instantaneous velocity magnitude contour at upper impeller location for Case 2: (a) with baffles, (b) without baffles. 53

5.5 Instantaneous velocity magnitude contour at upper impeller location for Case 3: (a) with baffles, (b) without baffles. 53

5.6 Phase-averaged velocity magnitude contour at upper impeller location for Case 1: (a) with baffles, (b) without baffles. 54

5.7 Phase-averaged velocity magnitude contour at upper impeller location for Case 2: (a) with baffles, (b) without baffles. 54

5.8 Phase-averaged velocity magnitude contour at upper impeller location for Case 3: (a) with baffles, (b) without baffles. 55

5.9 Phase-averaged velocity magnitude contour at $\theta = 0^\circ$ for Case 1: (a) with baffles, (b) without baffles. 55

5.10 Phase-averaged velocity magnitude contour at $\theta = 0^\circ$ for Case 2: (a) with baffles, (b) without baffles. 56

5.11 Phase-averaged velocity magnitude contour at $\theta = 0^\circ$ for Case 3: (a) with baffles, (b) without baffles. 57

5.12 Comparison of axial profiles of phase-averaged radial velocity in a plane midway between baffles at different radial locations for Case 1. 57

5.13 Comparison of axial profiles of phase-averaged radial velocity in a plane midway between baffles at different radial locations for Case 2. 58

5.14 Comparison of axial profiles of phase-averaged radial velocity in a plane midway between baffles at different radial locations for Case 3 [Agarwal *et al.*, 2021]. 58

5.15 Comparison of axial profiles of turbulent kinetic energy in a plane midway between baffles at different radial locations for Case 1. 59

5.16 Comparison of axial profiles of turbulent kinetic energy in a plane midway between baffles at different radial locations for Case 2. 59

5.17 Comparison of axial profiles of turbulent kinetic energy in a plane midway between baffles at different radial locations for Case 3 60

B1 Centerline distribution of mean streamwise velocity at different grid size (red plus : $1000 \times 200 \times 200$, green asterisk : $800 \times 200 \times 120$, open triangle : Kim *et al.* [2004], filled square: Nakagawa *et al.* [1999]). 73

B2 Profiles of mean streamwise velocity at different grid size (red plus : $1000 \times 200 \times 200$, green asterisk : $800 \times 200 \times 120$, open triangle : Kim *et al.* [2004], filled square: Nakagawa *et al.* [1999]) : (a) x^*/d = 1.0, (b) x^*/d = 3.5, (c) x^*/d = 6.0, (d) x^*/d = 8.5. 74

B3 Profiles of RMS streamwise velocity fluctuations at different grid size (red plus : $1000 \times 200 \times 200$, green asterisk : $800 \times 200 \times 120$, open triangle : Kim *et al.* [2004], filled square: Nakagawa *et al.* [1999]) : (a) x^*/d = 1.0, (b) x^*/d = 3.5, (c) x^*/d = 6.0, (d) x^*/d = 8.5. 74

B4 Profiles of Reynolds shear stress at different grid size (red plus : $1000 \times 200 \times 200$, green asterisk : $800 \times 200 \times 120$, open triangle : Kim *et al.* [2004], filled square: Nakagawa *et al.* [1999]) : (a) x^*/d = 1.0, (b) x^*/d = 3.5, (c) x^*/d = 6.0, (d) x^*/d = 8.5. 74

B5 Comparison of axial profiles of phase-averaged radial velocity at different radial locations for Case 1 at different grid sizes a) with baffles, and b) without baffles. 75

List of Tables

Table	*Title*	*page*
3.1	NVIDIA Tesla GP100 specifications	34
4.1	Comparison of drag coefficient	43
4.2	Computational efficiency of discrete velocity models on GPU cluster	44
4.3	Comparison of drag coefficient	47
4.4	Computational efficiency of BB and IB method on GPU cluster	47
5.1	Reactor and impellers dimensions [Rutherford *et al.*, 1996]	50

List of Symbols

Symbol	Description
c	lattice speed
$\overline{C}_D$	mean drag coefficient
c_s	speed of sound
C_s	Smagorinsky constant
C_1, C_2, C_3	impeller clearance (cm)
d	diameter of square cylinder (mm)
D	impeller diameter (cm)
D_c	circular disk diameter (cm)
D_f	discrete delta function
D_s	shaft diameter (cm)
$\vec{e}_k$	particle velocity vector in the kth direction
f_k	particle distribution function along direction k
f_k^{eq}	equilibrium distribution function along direction k
$f_k^{'}$	post-collision states of the particle distribution function along direction k
$f_k^{''}$	post-forcing particle distribution function along direction k
$\overline{f}_k$	filtered particle distribution function
$\overline{f}_k^{eq}$	filtered equilibrium distribution function
F_k	discrete force distribution function along direction k
$\vec{F}_b$	force vector on the boundary nodes
G	kernel function
H	height of the square duct (mm)
H_w	water level (cm)
k	spatial direction
$\mathbf{k}$	turbulent kinetic energy (m^2/s^2)
i, j, k	indexing in x, y, and z direction, respectively
L	length of the square duct (mm)
L_{bf}	baffle length (cm)
L_{bl}	blade length (cm)
N	rotational speed of the impeller (rpm)
N_{bf}	number of baffles plate
N_{bl}	number of blades
n	width of mapping window
n_x, n_y, n_z	domain size in x, y, z dimension, respectively
r	radial location (cm)
Re	Reynolds number
$\overline{S}$	characteristic filtered rate of strain
S_{ij}	filtered strain rate tensor at grid location, i, j
T	diameter of the cylindrical tank (cm)
t_r	simulation run time (sec)
$\vec{u}$	macroscopic fluid velocity vector (m/s)
u_x, u_y, u_z	magnitude of velocity in x, y, and z direction, respectively (m/s)

Symbol	Description
$\vec{U}_b$	velocity vector on the lagrangian markers at boundary surface (m/s)
$\vec{U}_b^{uf}$	unforced velocity vector at boundary nodes (m/s)
$< u >$	mean streamwise velocity (m/s)
$< v >$	mean normal velocity (m/s)
$\vec{u}^{uf}$	unforced fluid velocity vector (m/s)
U_m	Mean velocity (m/s)
U_{rad}	radial velocity of fluid flow (m/s)
U_{tip}	tip velocity of impeller blades (m/s)
V_w	water volume (l)
W	width of the square duct (mm)
W_{bf}	baffle width (cm)
W_{bl}	blade width (cm)
w_k	weight factor along direction k
$\vec{x}$	position vector of Eulerian fluid nodes
$\vec{x}_b$	position vector of boundary nodes
x^*	streamwise distance from the downstream face of the cylinder (mm)
x	streamwise dimension (mm)
y	cross-stream dimension (mm)
y	spanwise dimension (mm)
Δ	filter width
$\Delta x, \Delta y, \Delta x$	size of the lattice/grid spacing in x, y, and z directions, respectively
Δt	time-step size
$\overline{\phi}$	spatial dependent uantity
ρ	density of fluid (kg/m^3)
τ	relaxation time parameter
τ_t	total Relaxation time
ν	kinematic viscosity of the fluid (m/s^2)
ν_{SGS}	eddy viscosity (m/s^2)
ν_t	total effective viscosity (m/s^2)
$\overline{\Pi}_{ij}$	non-equilibrium momentum flux tensor at grid location, i, j
$< \cdot >$	time-and spanwise-averaging

List of Abbreviation

Abbreviation	Full form
$2-D$	Two-Dimensional
$3-D$	Three-Dimensional
$4-D$	Four-Dimensional
BB	Bounce-Back
BBL	Bounce-Back on the Link
BTE	Boltzmann Transport Equation
CFD	Computational Fluid Dynamics
CPU	Central Processing Unit
$CUDA$	Compute Unified Device Architecture
D_2Q_7	Two-dimensional lattice structure with seven velocities
D_2Q_9	Two-dimensional lattice structure with nine velocities
D_3Q_{13}	Three-dimensional lattice structure with thirteen velocities
D_3Q_{15}	Three-dimensional lattice structure with fifteen velocities
D_3Q_{19}	Three-dimensional lattice structure with nineteen velocities
D_3Q_{27}	Three-dimensional lattice structure with twenty-seven velocities
D_mQ_n	Lattice structure of m-dimensional and n-directions
DNS	Direct Numerical Simulation
$ELBM$	Entropic Lattice Boltzmann Method
$FCHC$	Face-Centered Hyper Cubic
FD	Finite Difference
FE	Finite Element
FV	Finite Volume
FHP	Frisch, Hasslacher, and Pomeau
$GPCs$	Graphics Processing Cluster
$GPUs$	Graphics Processing UnitsS
ID	Index
IB	Immersed Boundary
$IB-LBM$	Immersed Boundary-Lattice Boltzmann Method
LBE	Lattice Boltzmann Equation
$LBGK$	Lattice Bhatnagar-Gross-Krook
LBM	Lattice Boltzmann Method
LDA	Laser Doppler Anemometry
LDV	Laser Doppler Velocimetry
LES	Large Eddy Simulation
$LGCA$	Lattice Gas Cellular Automata
$MLUPS$	Millions Lattice Updates Per Second
MRT	Multi-Relaxation Time
NS	Navier-Stokes
$PDEs$	Partial Differential Equations
$PE's$	Processing Elements
PIV	Particle Image Velocimetry
$QELBM$	Quasi-Equilibrium Lattice Boltzmann Method

RANS	Reynolds-Averaged Navier-Stokes
RMS	Root-Mean-Square
RPM	Revolution Per Minute
SGS	Subgrid-Scale
SG	Sliding Grid
IO	Inner-outer
SIMD	Single Instruction Multiple Data
SM	Sliding Mesh
SMs	Streaming Multiprocessors
SRT	Single-Relaxation Time
SRT − LBM	Single-Relaxation Time-Lattice Boltzmann Method
SST	Shear-Stress-Transport
TPCs	Texture Processing Clusters
TKE	Turbulent Kinetic Energy

1
Introduction

1.1 BACKGROUND

A fluid can be described as a substance that cannot experience any shearing or tangential force at rest, whereas it starts deforming continuously under the applied shear stress. The popular Navier-Stokes (NS) equations are the fundamental basis of Computational Fluid Dynamics (CFD) to define fluid flow behavior. The fluid flow regimes are characterised by the Reynolds number in laminar, transition, and turbulent flows. The Reynolds number, abbreviated as *Re*, is a dimensionless quantity that represents the ratio of inertial to viscous force. It efficiently suppresses the small perturbations in the fluid flow resulting in the laminar flow regime; however, the larger value of the Reynolds number indicates the low viscous force within the fluid. As a result, it amplifies the perturbations that tend the flow regime from transition to turbulent.

As mentioned in the above para, the most successful and popular way of modeling incompressible flows in CFD is to solve the incompressible NS equations numerically. These equations are sets of second-order non-linear partial differential equations (PDEs) and satisfy the conservation principles of mass, momentum, and energy. The equations are based on the continuum assumption and describe the fluid flow dynamics at the macroscopic scale. The NS equations incorporate diffusive and convective transport of certain variables. The equations are solved with different numerical approaches, such as finite difference (FD) and finite volume (FV) methods. These methods discretize the governing NS equations for the fluid domain. The fluid domain is also discretized (or decomposed) into several sub-domains defined as the computational mesh. It results in algebraic equations that can be solved numerically for each of the sub-domain. The iterative procedures are generally used to solve these algebraic equations to obtain the macroscopic properties of fluid, such as density, velocity, and pressure for each of the mesh points of interest.

Although numerical studies on NS solvers have achieved significant successes, a number of difficulties and challenges remain. Firstly, solving the NS equations is a challenging task due to the non-linear terms in the equations. Secondly, it is not easy to get optimum solutions with the NS solvers for industrial applications, where geometry is much more complex [Hou *et al.*, 2019]. Moreover, the NS equations are particularly suitable for low Knudsen numbers (Kn «1). The Knudsen number is defined as the ratio mean free path of the molecule to the characteristic length of the system. The formulations of NS do not provide the converged solution for the high Knudsen numbers [Raabe, 2004].

From the past three decades, LBM has gained significant popularity as an alternative numerical approach to obtain continuum flow quantities [Aidun and Clausen, 2010a]. It became popular among researchers and scientists due to its wide range of applicability to simulate various chemical and physical processes associated with the fluid flow, multiphase flows [Grunau *et al.*, 1993], immiscible fluids [Gunstensen *et al.*, 1991], heat transfer [Han-Taw and Jae-Yuh, 1993; Ho *et al.*, 2002], and turbulent flows [Jahanshaloo *et al.*, 2013]. The method is initially evolved from the Lattice Gas Cellular Automata (LCGA), considered the fluid as a collection of particles [Sharma *et al.*, 2019]. The method introduced the concept of the averaged distribution function in its solution, which means a single distribution function contains all those fluid particles that are at the same

position at the same time moving with the same velocity despite solving the macroscopic flow variable like velocity, density, momentum, and temperature in other CFD solvers. This simplicity in the formulation of the LBM makes it exceedingly easy to code and particularly suitable for massively parallel computation.

The governing mathematical formulation of the lattice Boltzmann equation (LBE) includes the two-step procedure: streaming of the particle distribution functions and their collision. The idea behind the method is that a set of particle distribution functions residing on a lattice node stream to neighboring lattice sites, and collide with particle distribution functions coming from other directions resulting in the exchange of momentum. The net mass and momentum remain conserved during the collision process [Agrawal *et al.*, 2006]. The LBM method is justified by the fact the the collective behavior of many microscopic particles is not especially dependent on the specifics of microscopic processes of the individual molecules underlying the macroscopic dynamics of fluids. The method provides stable and local arithmetic operations for the macroscopic behavior of fluid and recovers NS equations.

Furthermore, the LBM depends on the lattice structure of the discrete velocity models for accuracy and stability. The discrete velocity models in LBM notation can be distinguished with D_mQ_n reference, where m represents the domain dimension, and n is the number of directions a particle is restricted to stream. The popular discrete velocity models are: seven velocities (D_2Q_7) and nine velocities (D_2Q_9) LB models for the simulation of two-dimensional (2-D) flows on the 2-D square lattice structure. For the three-dimensional (3-D) flows, fifteen velocities (D_3Q_{15}), nineteen velocities (D_3Q_{19}), and twenty-seven velocities (D_3Q_{27}) models on the cubic lattice structure are quite common. All of the aforementioned LB models include a resting particle in the discrete velocity set [Perumal and Dass, 2015]. In general, LBE models containing a rest particle have higher computational stability. These discrete velocity models play an essential role in obtaining the solutions to fluid flow problems. For example, reductions in the velocity model can significantly decrease the calculation effort but deteriorate the stability and accuracy of the findings. As a result, to achieve a more precise solution, the calculation grids or the number of velocities must be increased.

1.2 RESEARCH MOTIOVATION

In the present thesis work, numerical simulations has performed with LBM to examined its viability for the turbulent flow simulation on different geometry cases. The LBM has a number of appealing characteristics that distinguish it from the conventional NS solvers and make it a viable choice for modeling complex turbulent flows.

- The convection term in the governing equation of LBM is linear; however, the NS equations consist of a non-linear convection term that takes a long time to solve numerically.
- The LBM shows isotropic nature to the second order. It means the solution experiences the minimal influence of the orientation of the computational grid. This factor provides an advantage for the simulation of turbulent flow since the turbulent structures are three-dimensional. In other words, if the solution of the numerical scheme is prone to the orientation of the computational grid, it also influenced the direction of turbulent structures [Bespalko, 2011].
- Another advantage of LBM over NS solvers is that the LBE involves local collision operation, compared to the coupled equations in conventional NS solvers, which makes LBM highly parallelizable. This also ensures good scaling performance of computational code with the increasing number of parallel processors and can be used efficiently for parallel computation

on a multi-core GPU platform. This advantage is especially useful for modeling turbulent flows, where the computational domain consists of a large number of grid points.

In the literature, many studies have been reported for the turbulent flow simulation using LBM. One of the earliest works in this field was reported by Benzi and Succi [1990] by simulating 2-D forced isotropic turbulence with LBM. Later, Lammers *et al.* [2006] used the direct numerical simulation (DNS) turbulence model to simulate a turbulent plane-channel flow within the incompressible limit ($Re_\tau = 180$) using D_3Q_{19} SRT-LBE. Their results demonstrated excellent agreement with the past DNS and pseudo-spectral data. Another numerical study has been performed by Fernandino *et al.* [2009] using the LES-LBM for the investigation of turbulent fow in an open duct. Chikatamarla *et al.* [2010] used the LBM for the DNS of turbulent fows. Wang *et al*. [2014] presented the comparative study of DNS and LES for the wall-bounded turbulent fow and developed the parallelized computer code suitable to run on multiple GPUs platform. In a recent study Peng *et al.* [2018] presented the DNS results of turbulent flow simulation in a pipe using the LBM.

The studies mentioned above confirm that numerous studies have been carried out for the turbulent flow in the frame of LBM. In particular, for the turbulent flow simulation in the 3-D computation domain, the D_3Q_{19} lattice velocity model was primarily adopted by the researchers [Bespalko, 2011; Lammers *et al.*, 2006; Pattison *et al.*, 2009], as it produces higher stable and accurate results comparable to the D_3Q_{15} velocity model [Mayer and Házi, 2006; Mei *et al.*, 2000] and offers better computational efficiency in terms of memory and run time than the D_3Q_{27} velocity model. However, to the best knowledge of the author, the detailed comparison of different discrete velocity models of LBM with the inclusion of turbulence has not been made so far. Very few studies are available in the literature for the comparison of different discrete velocity models. Mei *et al.* [2000] presented a study for the comparison of discrete velocity models for 3D flows with curved boundaries. The results reported the computational efficiency and stability for all the discrete velocity models. The result obtained showed that the D_3Q_{15} velocity is more prone to numerical stability. However, D_3Q_{27} is more computationally expensive, and D_3Q_{19} shown a balance between numerical stability and computational efficiency. Yasuda *et al.* [2014] performed a study to compare the accuracy and computational efficiency of D_3Q_{13} and D_3Q_{19} velocity model using the different (lattice Bhatnagar–Gross–Krook (LBGK), the quasi-equilibrium lattice Boltzmann model (QELBM) and multi-relaxation time (MRT)) collision models of LBM for homogeneous isotropic decaying turbulence. The results reported by Yasuda *et al.* [2014] showed a higher computational performance of D_3Q_{13} velocity model. However, the model suffers from the limitation of less accurate results compared to the D_3Q_{19} velocity model. Later, Yasuda *et al.* [2017] repeated the same study for the homogeneous isotropic decaying turbulence with some more discrete velocity and collision models. The study reported a comprehensive comparison of D_3Q_{13}, D_3Q_{15}, D_3Q_{19}, and D_3Q_{27} velocity models along with QELBM, LBGK, MRT, and ELBM collision models. The obtained results showed that the decrease in the velocities considerably decreases the computational effort, but it provides less accurate results and compromises stability.

Furthermore, the handling of boundary nodes is a critical parameter for flow simulation in simple and complex geometry. Thus, the boundary conditions play a significant role in the CFD and are essential in modeling fluid flow problems. It is because the accuracy, time complexity, and applicability of the numerical method in CFD depend on how the boundary nodes are treated with the relevant boundary condition. Also, the boundary conditions are such an important part of defining a problem that fluid flow behavior shows a completely different flow field because of the implication of different boundary conditions on the boundary nodes, despite the fluid domain being simulated with the same numerical method. A variety of methods are developed for the treatment of stationary and moving boundaries in LBM [Zou and He, 1997; Kao and Yang, 2008; Kang and Hassan, 2011]. The LGCA technique was first considered to determine the boundary

conditions at the wall nodes in the LBM. The bounce-back (BB) rule, for example, was utilized to provide a no-slip velocity condition at the boundary walls. The approach is extensively described in the literature [Wolfram, 1986; Lavallee *et al.*, 1991; Cornubert *et al.*, 1991; Ziegler, 1993; Ginzbourg and Adler, 1994]. The idea behind the approach is that the particle distribution functions that propagate along the boundary wall are BB with an appropriate momentum adjustment. The ease of implementing the BB rule for the no-slip boundary condition at the boundary wall supports the notion that the LBM is suitable for modeling fluid flows in complex geometries. However, the method shows first-order numerical accuracy. It degrades the LBM overall accuracy for the interior fluid nodes, where the governing LBE is second-order accurate.

Following that, significant work was expanded in developing more precise boundary conditions than the bounce-back rule. And, the researchers proposed several other methods for the treatment of boundary nodes to enhance the numerical accuracy of the LBM. Noble *et al.* [1995] suggested that a pressure restraint be applied on non-slip walls with hydrodynamic boundary conditions. The BB condition was expanded by Zou and He [1997] for the non-equilibrium component of the particle distribution functions. Ziegler [1993] proposed the half-way bounce-back rule. The method showed that placing the boundary wall at half of the mesh distance of the fluid gives second-order accuracy. The other notable works in this direction are Skordos [1993]; Chen *et al.* [1996]. However, numerous boundary schemes are developed by researchers in the past few years to treat boundary nodes in LBM. A detailed comparison of the impact of these boundary conditions for the wall-bounded turbulent flow is not yet reported in the literature.

The current research has also been motivated to visualize the fluid flow behavior, utilizing LBM as a numerical tool in complex geometry. Thus, the simulations to analyze the fluid flow pattern in the stirred tank reactor equipped with dual-Rushton impellers were carried out. For a stirred tank bioreactor, the presence of a high-speed rotating impeller and stationary baffles makes the flow structure highly turbulent. As a result, CFD modeling of turbulent flow in a stirred vessel provides a sufficient amount of useful data to analyze flow behavior, vortex formations, circulation patterns, Reynolds stresses, etc. In addition, the user may easily comprehend the flow-related reactor operations by visualizing all of the above characteristics. Furthermore, one of the multiple flow-associated processes, mixing, is utterly dependent on the fluid flow behavior, which further identifies the possible problems in advance.

1.3 RESEARCH OBJECTIVE AND AND CONTRIBUTIONS

This section describes the major goals of our research and the thesis contributions. The thesis objectives are:

- **Effect of different discrete velocity models of LBM for the turbulent flow simulations:** In the literature, many studies have been reported for the turbulent flow simulation using LBM. Moreover, as mentioned earlier, the LBM depends on the lattice structure of the discrete velocity models. To this end, the first objective of the thesis is to investigates the efficiency of discrete velocity models of LBM for the turbulent flow simulation. And to achieve it, a comparative study with three other 3-D discrete velocity models has been performed for turbulent flow over a bluff body at Re_d = 3000. The study reported the results for various turbulent statistics for all the three discrete velocity models and also presented the computational efficiency of each.

- **Effect of different boundary conditions on the predicted results:** Our objective is to study the effect of different boundary conditions in LBM for the turbulent flow simulation. And, to meet the goal, the impact of two different versions of boundary conditions in LBM used to impose the no-slip condition on the boundary walls is presented. A similar flow

configuration of turbulent flow over a bluff body mentioned in the above para is used for comparison.

- **Applications of the developed model to flow in complicated geometries:** As discussed in Section 1.2, CFD plays an essential role in numerous contexts for optimizing reactor design. Thus, the third objective of the present research work is to validate the applicability of the LBM for the modeling of turbulent flow involved in the fluid flow process of stirred tank reactor. A comprehensive study of the stirred tank reactor equipped with a dual Rushton turbine using LBM has been reported in this work. In a stirred tank reactor, it is usually seen that the impeller swirls the whole liquid volume as a homogeneous body in the tank during the stirring processes, resulting in inefficient agitation. The problem can be easily resolved by installing the flat sheet-like structure commonly called 'baffles' on the wall of the reactor tank. The baffles produce shear stresses in the tank, preventing the mass swirling of the liquid volume and using the energy to mix the fluid. The current study presents the flow characteristics in a stirred tank equipped with two six-blade Rushton impeller, and acknowledges the impact of baffles on the flow. Furthermore, the study also shows the effect of baffles with different impeller clearance on the flow characteristics and their influence on mixing.

In addition to the above contributions, the present thesis work also reports the computational efficiency of the LBM algorithm on shared machines. A highly parallel LBM solver is developed using CUDA programming model to execute the simulations on a multi-core GPU architecture.

1.4 THESIS LAYOUT

The remainder of the thesis is structured as follows:

Chapter 2 provides an extensive review of the previous studies carried out on the application of the LBM for simulation of turbulent flow. The chapter mainly discusses the available literature on the use of LBM for the turbulent flow simulation over the bluff body and for investigating liquid phase hydrodynamics in stirred tank reactors.

Chapter 3 provides a detailed description of the methodology used in the present thesis work to study the problems mentioned in the section above. We discuss the governing equations of LBM to discrete the fluid domain, turbulence model, boundary conditions, and the process of parallelization of code on the GPU platform.

Chapter 4 discusses the influence of discrete velocity models of LBM and boundary conditions on the benchmark fluid flow problem of turbulent flow over a bluff body.

Chapter 5 discusses the results obtained from the study to show the effect of baffles on the flow hydrodynamics of dual-Rushton turbine stirred tank bioreactor.

Chapter 6 presents the conclusion of the thesis and recommended list of relevant fields for future work.

…

2
Literature Survey

The present thesis aims to investigate the viability of the LBM for the turbulent flow simulation. The modeling of turbulent flow using LBM has been an active area of research for several years, and multiple attempts are documented in the literature. The literature survey presented in this chapter reviews the studies carried out in the past few years for the benchmark problem of turbulent flow over a bluff body and turbulent flow simulation in a stirred tank reactor. The chapter discusses the various essential aspects and quality results obtained by researchers in recent times.

The remainder of the chapter is organized as follows: Section 2.1 describes the origin of LBM. A brief description on the collision models of LBM is presented in Section 2.2. Section 2.3 reviews the past attempts made to model the turbulent flow using LBM. Section 2.4 summarizes the chapter.

2.1 THE HISTORY OF LBM

The LBM was originated from the LGCA. It is a type of cellular automaton used to simulate fluid flow problems. The dynamics of the LGCA are governed by the principle of discrete kinetics utilizing a discrete lattice and discrete-time, with the local collision rules for the conservation of mass and momentum [Guo and Shu, 2013; Succi *et al.*, 1991]. Later, it was found that LBM can also be derived by using a special standard FD method for the kinetic equation of the discrete velocity distribution function [He and Luo, 1997; Chen and Doolen, 1998]. The first step in this direction was taken by Broadwell [1964] to provide a discrete velocity model for studying the shock structures in a one-dimensional lattice. Here the velocity was chosen in a discrete form, with space and time kept continuous [Benzi *et al.*, 1992]. The full discrete particle velocity model of lattice Boltzmann named HPP primarily coined by Hardy *et al.* [1973, 1976], where space and time both were discretized in a square lattice. The model was used to simulate the particle moving in the axis-parallel direction in a square lattice. However, due to a lack of isotropy in the lattice, the HPP model was found unsuitable to reproduces the non-linear and dissipative terms in the NS equations [Benzi *et al.*, 1992]. In 1986, a group of French and American scientists, Frisch, Hasslacher, and Pomeau (FHP) used the LGCA principles for 2-D hydrodynamics to recover the proper NS equations on a hexagonal lattice. [Frisch *et al.*, 1986]. The model used the LBE in the frame of LGCA to calculate viscosity [Perumal and Dass, 2015]. However, the 3D extension of the FHP model had not shown the required lattice symmetries for the 3D simulations. Further, a 3D model for simulating the NS equations on lattices was proposed by d'Humieres *et al.* [1986] on a four-dimensional (4-D) face-centered-hyper-cubic (FCHC) lattice with all the required symmetries for 3D simulations.

The term lattice in LGCA denotes that one is working on a *d*-dimensional, regular lattice. The word gas implies that gas particles are moving through the lattice. The gas particles are defined by the Boolean variables (0 and 1), residing on a regular lattice node, and the evolution is primarily explained by a set of collision rules that possess suitable conservation laws [Benzi *et al.*, 1992]. The LGCA model has discrete space, time, and particle velocities. A collision and

propagation step is included in each iteration of LGCA. However, the LGCA showed significant shortcomings of statistical noise, non-Galilean invariance, an unphysical velocity that is reliant on huge numerical viscosities and pressure, and implementation difficulty in three dimensions [Perumal and Dass, 2015]. McNamara and Zanetti [1988] replaced the particle occupation variables (Boolean variables) with a single-particle distribution function and ignored individual particle motion and particle-particle correlations in the kinetic equations to reduce statistical noise in LBM [Chen and Doolen, 1998]. Afterward, Higuera and Jimenez [1989] made a significant contribution by incorporating the linearized collision operator under the assumption that the particle-distribution function is close to the local equilibrium state [Perumal and Dass, 2015]. This linearized collision operator includes a non-dimensional relaxation time parameter due to the fluid-particle collision, which describes the time taken by the fluid particle to reach equilibrium [Kang and Hassan, 2011].

2.2 COLLISION MODELS OF LBM

In the past few years, researchers have developed variants of collision models of LBM. The simplified version of the linearized collision operator is the LBGK based on the single-relaxation time (SRT) approximation, which was introduced independently by several authors [Bhatnagar *et al.*, 1954; Qian, 1990; Koelman, 1991; Chen *et al.*, 1991]. The LBGK model recovers the NS equations using the local equilibrium distribution function. The model is also known as the SRT model of LBM. LBGK is the most popular model of the LBM due to its extremely simple formulation. However, the model has several inherent deficiencies, including numerical instability in complex flows at finite Knudsen, K_n or high Reynolds, Re number, and inaccurate boundary conditions [Luo *et al.*, 2011]. As a result, the researchers proposed several other collision models, including the multiple relaxation time (MRT) model [Lallemand and Luo, 2000; d'Humieres, 1994; d'Humières *et al.*, 2001; d'Humières, 2002; Lallemand *et al.*, 2003], two-relaxation time model [Ginzburg *et al.*, 2008b,a; Ginzburg and d'Humieres, 2003]. A detailed description of all these LB models can be found in the review article of Aidun and Clausen [2010b]

2.3 LBM IN TURBULENCE MODELING

This section reviews the studies reported in the literature related to the turbulent flow modeling using LBM. First, attempts are made to address the work done by the researchers using LBM on the benchmark fluid flow problem of turbulent flow over a bluff body. Secondly, the available literature on the turbulent flow simulation in the complex domain of stirred tank reactor using LBM has been reviewed.

2.3.1 Study of Turbulent Flow Simulation over Bluff body

A notable experimental work with the laser-Doppler measurements was conducted by Lyn *et al.* [1995] to explore the ensemble-averaged turbulence features near the wake of a square-cylinder. Another significant contribution in this area was made by Srinivas *et al.* [2006]. Srinivas *et al.* [2006] performed numerical simulation on flow past over a square cylinder at Reynolds number (Re) = 21,400. The authors employed the LES approach to model the turbulence, and a dynamic subgrid-scale stress model was applied to resolve the small-scale turbulent structures. The results for time- and span-averaged axial and transverse velocities at the downstream face of the cylinder were provided. The research work also reported on the distribution of turbulent normal and shear stress. The results were compared with the experimental findings of Lyn *et al.* [1995] and found to be in good agreement. Hamane *et al.* [2015] presented LBM result for two-dimesional turbulent flow around a circular cylinder. SRT-LBM model was used in the simulation. LES model was used to model the turbulent structures. The Smagorinsky

SGS model was adopted for small-scale eddies. The results showed that the small-scale vortices were successfully captured. Wei and Hu [2017] proposed a modified version of LBM and used it to investigate the turbulent flow behavior past over a row of cylinders in 2-D. The results were presented for velocity, vorticity difference, energy density enstrophy spectra. The numerical findings corresponded well with the experimental results of Kellay *et al.* [1998].

Koda and Lien [2015] implemented the LBM on the GPU platform to study the turbulent flow behavior past over a square cylinder confined in a channel. The particular SRT-LBM model was used in the study to discretize the fluid domain. The D_3Q_{19} discrete velocity model was adopted for the 3D computational domain. The authors used the LES method to model the large-scale turbulent structures, and the Smagorisnky SGS model was adopted to resolve the small-scale turbulent motions. The Reynolds number based on the diameter of the cylinder was 3000. The simulations were performed for two different spanwise dimensions. The authors reported that the simulation performed on smaller spanwise dimensions over-predicted the turbulent statistics. However, for other spanwise dimensions, the results were in good agreement with the experimental findings of Nakagawa *et al.* [1999], and the numerical results of Kim *et al.* [2004].

Some other notable works in turbulent flow simulation past over a bluff body include those of Kajzer and Pozorski [2017], Feuchter *et al.* [2019], and An *et al.* [2020]. Although they are more theoretically interesting, there appears to be very little work done on the turbulent flow over a bluff body by LBM.

2.3.2 Study of Stirred Tank Reactor Simulation

This subsection presents a detailed insight into the research studies done in the past years to understand the hydrodynamics of the stirred tank reactor using LBM as a numerical tool. The scope of this review is limited to the studies reported only on the simulation of single (liquid) phase hydrodynamics in stirred tank reactor.

Eggels [1996] took the first step in this direction to visualize the flow behavior in a stirred tank bioreactor using LBM. The author reported the isothermal, single-phase, turbulent flow in a standard configuration stirred tank reactor consisting of a cylindrical vessel fitted with four baffles and a 6-blade disc turbine using a LES turbulence model. The scheme of LBM given by Eggels and Somers [1995] was adopted to discretize the fluid domain. The author presented the use of a new LBM scheme for the turbulent flow simulation. The conventional Smagorinsky model was used in the study with Smagorinsky constant $C_s = 0.1$ to model the subgrid-scale stresses [Smagorinsky, 1963]. The author performed two simulations on largely the same geometry that only differs in some simulation parameters and blade thickness. The results were presented for various turbulent statistics, such as instantaneous and time-averaged vector fields, mean and RMS radial and axial velocity profiles at various radial and impeller midplane locations. The results were validated with the experimental data of Wu and Patterson [1989], and Bakker Bakker [1995]. The results were in good accord with the experimental data. The author concluded that the new LB scheme allows researchers to simulate reactors of different geometries with different impeller shapes. Also, the model is suitable for performing scale-up studies for a single-phase reactor.

Another work in this direction to study the turbulent flow in a stirred tank reactor was done by Derksen and Van den Akker [1998]. The authors used LES to simulate turbulent flow in a baffled stirred tank reactor of standard configuration with a 6-blade Rushton turbine. LBM proposed by Eggels and Somers [1995] was used as a numerical approach for the simulation of the fluid domain. The simulations were performed up to Reynolds number, $Re = 10000$ on a cubic computational grid of 120^3. An adaptive force field approach proposed by Derksen *et al.* [1997] was adopted for defining the effect of the non-square or rotational objects on the liquid flow field.

The parallel computer code based on Single Instruction Multiple Data (SIMD) was developed to run on the HP-Convex S-Class machine equipped with four processing elements (PE's). The results were presented for the velocity and vorticity components. The wakes were observed behind the impeller blades. Moreover, the two counter-rotating vortices were also seen behind the blades that deliberately dissolved in the turbulent flow as we move away from the impeller region in the radial direction. The power number was calculated to represent the power drawn by the impeller. The power-number versus Reynolds number plot was compared with experimental results of Rushton *et al.* [1950]. The results were consistent with the experimental data. .

Later, Derksen and Van den Akker [1999] performed another LES study to investigate the turbulent flow characteristics in a stirred tank reactor at Reynolds number, $Re = 29000$. The study reported the results for the phase-resolved average flows and different turbulence characteristics. The results were compared with experimental data of Wu and Patterson [1989], and Derksen *et al.* [1998]. The obtained results showed that the maximum radial velocity as a function of radial position was in good agreement with the experimental data. However, the simulations overestimated the maximum tangential velocity by $\sim 15\%$ compared to the experimental results. Also, the authors noticed that the random kinetic energy shows significant deviation from both the experimental results Wu and Patterson [1989]; Derksen *et al.* [1998] at a radial location closer to the impeller. However, the maximum level of kinetic energy achieves a good comparison with the experimental data.

Lu *et al.* [2002] had carried out an LES study for the stirred tank reactor using LBM on a non-uniform grid. The standard configuration of the stirred tank reactor equipped with a 6-blade Rushton turbine and four baffles mounted on the wall of the tank was chosen. Eggels and Somers [1995] LBM model was used as a numerical approach to discretize the fluid domain. A parallel computer code was developed to perform the simulation. The computer program also used the Smagorinsky SGS model to account for the turbulent eddies smaller in length scale compared to the computational lattice size.

In the results, the authors reported the axial profiles of time-averaged radial and tangential velocity components at different radial locations. The results revealed an acceptable agreement with the experimental results of Wu and Patterson [1989]. Moreover, the accuracy of the results was found comparable with the simulated results of Eggels [1996] and Derksen and Van den Akker [1999]. The results also show that the maximum tangential velocities are in better agreement with the experimental results of Wu and Patterson [1989] compared to the results of Eggels [1996] and, Derksen and Van den Akker [1999].

Hartmann *et al.* [2004] studied the turbulent flow within a baffled tank stirred tank reactor powered by a 6-blade Rushton turbine at $Re = 7300$ using the LES and RANS turbulence models. The LBM scheme suggested by Eggels and Somers [1995] was applied to discretize the liquid flow field. Smagorinsky and Voke subgrid-scale models were employed in LES to resolve the small-scale turbulence motions. The influence of the reactor components (i.e., impeller, baffles, and tank wall) on the liquid flow field was represented using an adaptive force-field approach. As a working fluid, silicon oil was used in the investigation with a density of 1039 kg/m^3. To solve the NS equations for the RANS simulation, the CFD algorithm CFX 5.5.1 based on the FV method was used. However, the turbulence was modeled by using the shear-stress-transport (SST) model given by Menter [1994]. The author also conducted the LDA experiment for the validation of simulation results. The results demonstrated excellent agreement for phase-averaged radial velocity obtained from both the RANS and LES models with the experimental findings. However, the RANS findings revealed deviations in the tangential velocity component and overprediction of the tangential velocity component near the center of the impeller tip in all simulated results. In addition, the LES results for the levels and structure of the TKE were more consistent with experimental data in

impeller discharge flow than with RANS calculations.

Gillissen and Van den Akker [2012] performed the DNS study to investigate the turbulent flow in a baffled stirred tank reactor equipped with a 6-blade Rushton turbine. The authors compared the obtained results with simulation results of LES and RANS turbulence models and with the experimental data of Laser Doppler Velocimetry (LDV) and Particle Image Velocimetry (PIV) from the literature. The LB scheme of Eggels and Somers [1995] was used for discretizing the liquid flow field. Two DNS cases were performed, one at a coarse grid and the other at a fine grid. Moreover, the authors also performed two simulations with LES to compare the DNS results with LES. In LES1, in order to resolve the small-scale turbulent structure, Smagorinsky SGS with a Smagorinsky constant $C_s = 0.12$ was used. However, in LES2, the Smagorinsky constant was computed dynamically, and the Van Driest wall model was applied. All the simulations were performed at Reynolds number $Re = 7300$. The authors computed the Kolmogorov length scale to verify whether the simulations fully resolve all scales of turbulent eddies. The study revealed that the minimum Kolmogorov length scale in the turbulent wake of the turbine blades was smaller than the grid spacing The authors presented the results for instantaneous vorticity to address this issue, which showed the smooth structures for all the length scale turbulent eddies. The presented results confirmed the well-resolved turbulent flow field. The study also showed that at certain locations, RANS and LES results for the TKE and turbulent energy dissipation rate were consistent with the experimental results compared to the DNS results. The authors suggested that more experimental and numerical work needs to be done to avoid the above-unexpected observation and to accurately predict the turbulent energy dissipation rate close to the turbine.

Shu and Yang [2018] investigated the computational performance of the parallel LBM algorithm on the multi-core GPU architecture for the turbulent flow simulation in a stirred tank reactor. The study was performed on the baffled stirred tank reactor of standard configuration equipped with a 6-blade Rushton impeller at Reynolds number, $Re = 7300$. The MRT scheme of LBM with D_3Q_{19} discrete velocity model was used to discretize the NS equations. LES was used to model the turbulence. However, to resolve the small-scale turbulent structures, three different cases were performed, one with the Smagorinsky SGS model and the other two with Coherent LES model[Kobayashi, 2005]. The immersed boundary (IB) method was used for representing the impact of the reactor components on the fluid domain Kang and Hassan [2011]. The study also performed the three simulation cases on commercial Ansys software.

The results were presented for the axial distribution phase-averaged velocity components and TKE at different radial locations and compared with the data obtained by Hartmann *et al.* [2004] from the laser Doppler anemometry (LDA) experiment and SRT-LBM simulation. The results were in fair agreement with the experimental results. However, it was noticed that results obtained from the coherent LES at reasonable grid resolution for the high turbulence region resolved more than 95% of the total TKE. The results were much better than the Smagorinsky SGS model for reproducing the monotonic decrease of TKE along the radial direction. Furthermore, GPU accelerated LBM simulation on a desktop computer was observed to be computationally efficient compared with conventional CFD solvers. The simulation for the LBM was 1500 times faster than standard CFD simulation at 16 CPU cores, even for the grid resolution of about 8.8 times the Kolmogorov length scale.

2.4 ISSUE AND CHALLENGES

- **Flow over bluff body:** It is discussed in Section 1.1 that LBM is a discrete particle-based method. It consists of the particle distribution functions arranged in a lattice structure of the discrete velocity models. Researchers proposed variants of the discrete velocity models that differ on the dimension of the lattice structure and the number of directions it contains

in which the particle distribution functions are restricted to stream. Thus, discrete velocity models of LBM play an essential role in the prediction of flow behavior. Several studies are present in the literature that used different collision and discrete velocity models to perform the simulations. However, the detailed comparison of the effect of discrete velocity models for the turbulent flow behavior past over a bluff body has not been made so far. This is addressed in the present thesis.

- **Flow simulation in stirred tank reactor:** The studies carried out by the researchers in the past two decades for the investigation of single (liquid)-phase hydrodynamics in the stirred tank reactor using LBM were performed either with the LB scheme proposed by Eggels and Somers [1995] or with the MRT-LBM collision model. Both the models have some advantages and limitations over other collision models of LBM. An advantage of the models is that these models provide better stability for the flow simulation at high Reynolds numbers. The limitations of these models are that despite the models offer higher stability, the algorithms of these models are complex to implement, and the models are less computationally efficient than the SRT-LBM model. Thus, modeling the large-scale reactor with these models is a challenging task and requires high computational power. It emphasizes the importance of using the SRT-LBM model for flow simulation in a large-scale reactor. Thus, in this thesis work, the SRT-LBM model is used to discretize the flow domain. And, LES turbulence model is incorporated in the LBE of the SRT-LBM model to model the turbulent structures.

  Furthermore, a review of previous research studies revealed that most of the works had been done on the stirred tank reactor equipped with a single impeller. However, multiple impellers are usually preferred in the industrial unit for efficient mixing and better productivity. In the past few decades, researchers have used numerous experimental techniques to observe the flow characteristics in stirred tank reactors, such as LDA and particle image velocimetry (PIV). The first experimental study using LDA techniques to observe the flow characteristics in a stirred tank equipped with two-Rushton impellers was performed by Rutherford *et al.* [1996]. This study investigated the flow characteristics, power consumption, and mixing time in the dual Rushton impeller stirred tank reactor at Reynolds number (Re = 40,000). A set of experiments were performed for different spacing between two impellers and at different impeller clearance from the vessel bottom. The other experimental works to understand the flow processes in the stirred tank reactor equipped with dual-impellers are described by Bonvillani *et al.* [2006]; Chunmei *et al.* [2008]; Xinhong *et al.* [2008]. However, relatively fewer numerical studies are available in the literature for a stirred tank reactor fitted with the dual impeller. Some of the works in this direction are presented by Micale *et al.* [1999]; Zadghaffari *et al.* [2009]; Li *et al.* [2012]. Micale *et al.* [1999] reported the numerical results of the flow behavior in the stirred tank reactor fitted with dual-Rushton impellers. The geometric configuration of the stirred tank reactor was similar to that used by Rutherford *et al.* [1996]. The authors used two numerical methods to perform the simulations.: the sliding grid (SG) and the inner-outer (IO) iterative procedure. The presented results showed the comparison between the two numerical approaches and the validation with experimental findings of Rutherford *et al.* [1996]. Zadghaffari *et al.* [2009] performed the numerical simulation on a fully baffled stirred tank reactor with two six-blade Rushton impellers using the sliding mesh (SM) approach. LES was used in the study to model the turbulence eddies. The study also conducted a PIV experiment to validate the simulation results. The authors considered three different speeds of the impeller's rotation in the study, i.e., 224, 300, and 400 rpm. The study reported the results for the flow field, power consumption, and mixing time. Li *et al.* [2012] conducted the PIV experiment and also performed LES simulation on the same geometry used by Rutherford *et al.* [1996] for the merging flow characteristics. The study validated the obtained experimental findings and numerical results with Rutherford *et al.* [1996] and Micale *et al.* [1999].

In this thesis, numerical simulations are carried out using LBM to predict the flow pattern and study the flow properties on a stirred tank reactor of similar configuration to that employed by Rutherford *et al.* [1996] in the experiment. And, to the best knowledge of the author of this work, the comprehensive study of the stirred tank reactor equipped with a dual Rushton turbine using LBM has not yet been reported in the literature. The current study not only presents the flow characteristics in the dual Rushton stirred tank but also acknowledges the impact of baffles on the flow. The study also shows the effect of baffles with different impeller clearance on the flow characteristics and its influence on mixing, which has not been studied so far. The research work reported by Rutherford *et al.* [1996]; Micale *et al.* [1999] are used to validate the results with the experimental observations of Rutherford *et al.* [1996] for the numerous fluid flow properties, including flow averaged velocity and TKE.

2.5 SUMMARY

This chapter provides a detailed review, analysis, and research gaps on the application of LBM in turbulent flow simulation. First, the chapter detailed the development of the LBM and discussed the various types of LBM collision models. Further, the research studies available in the literature for the simulations of turbulent flow over bluff bodies and in stirred tank reactors using LBM have been reviewed. The reviewed studies explored the feasibility of LBM for turbulent flow simulation at various geometrical and simulation parameters. Lastly, the issue and typical challenges in the LBM simulations of turbulent flow over buff bodies and stirred tank reactors are discussed. In a nutshell, the literature survey is described mainly to address the research goals of the thesis. The solutions to the research objectives are discussed in the subsequent chapters.

…

3
Methodology

This chapter provides a detailed description of the methodology used in the present thesis work to simulate various fluid flow problems using LBM. First, the formulation for governing equations of the particular SRT-LBM is introduced in detail. Secondly, the incorporation of LES turbulence model in LBE is explained. Later, a comprehensive overview of the different boundary conditions is also described in detail. Lastly, an explanation of the CUDA programming model for parallelizing LBM code to make it suitable to run on multi-threaded GPU platform is presented.

The remainder of the chapter is organized as follows: Section 3.1 provides a detailed description to the formulation of LBM, followed by the explanation of incorporating the LES turbulence model in the LBM framework. The details of the boundary conditions are presented in Section 3.2. Section 3.3 includes the information of the GPU architecture and the implementation of the LBM algorithm on the GPU platform. Section 3.4 summarizes the chapter.

3.1 SIMULATION PROCEDURE

In this section, a comprehensive description of the methodology used in the thesis work has been presented. The section starts with the detailed introduction of the SRT-LBM collision model of LBM, used in the present thesis work to discretize the fluid domain, followed by the explanation for incorporating the LES turbulence model in the LBE.

3.1.1 Single-Relaxation-Time (SRT) model

This subsection discussed the single relaxation time (SRT) model of LBM. SRT is the most commonly used model of LBM for solving fluid flow problems [Qian *et al.*, 1992]. SRT-LBM is described here for D_2Q_9, D_3Q_{15}, D_3Q_{19}, and D_3Q_{27} discrete velocity models of LBM [Yasuda *et al.*, 2017]. Figure 2.2 shows the lattice structure of D_2Q_9, D_3Q_{15}, D_3Q_{19}, and D_3Q_{27} discrete velocity models. The governing LBE for the SRT-LBM can be written as:

$$f_k(\vec{x}+\vec{e}_k\Delta t, t+\Delta t) = f_k(\vec{x},t) + \frac{1}{\tau}[f_k^{eq}(\vec{x},t) - f_k(\vec{x},t)] \tag{3.1}$$

where, f_k and f_k^{eq} are the particle and equilibrium distribution function along direction k at $(\vec{x},t)$, $\vec{e}_k$ is the particle velocity vector in the kth direction, Δt is the time step size, and τ is the single-relaxation time parameter that controls the rate of approach to equilibrium [Perumal and Dass, 2015]. The above equation for SRT-LBM consists of two essential steps, namely streaming and collision steps.

Collision step: In the step particle collides locally, The step relaxes the particle distribution function f_k to the equilibrium distribution value f_k^{eq} at each lattice location [Hecht and Harting, 2010]. The mathematical expression for the step can be written as:

$$f_k^{'}(\vec{x},t) = f_k(\vec{x},t) - \frac{1}{\tau}[f_k(\vec{x},t) - f_k^{eq}(\vec{x},t)] \tag{3.2}$$

Streaming step: The step is not local, and each of the particle distribution f_k propagate to

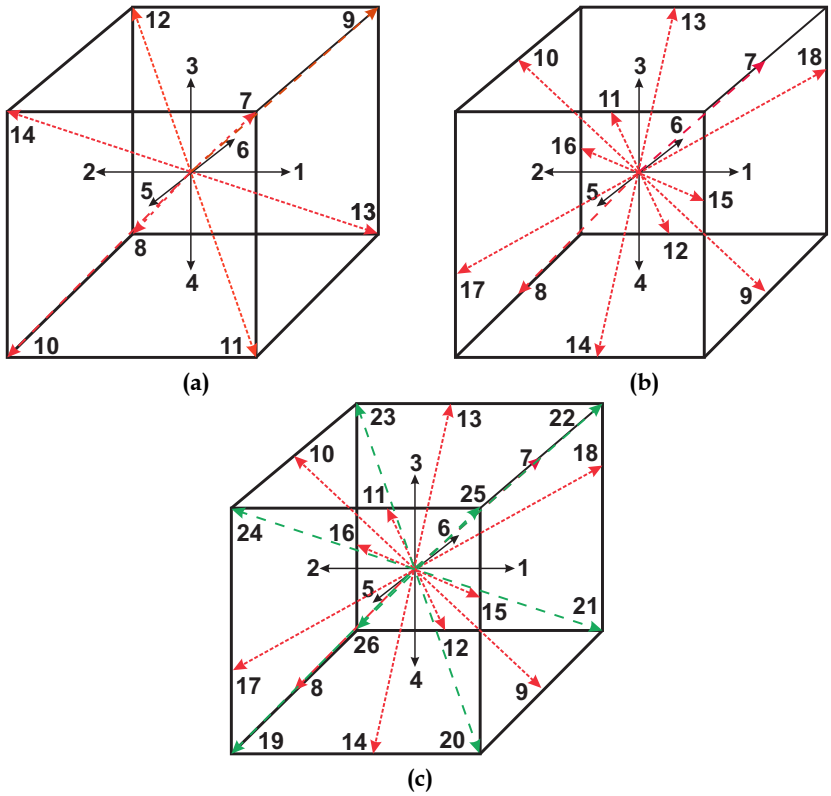

Figure 3.1 : Lattice structure of (a) D_2Q_9, (b) D_3Q_{15}, (c) D_3Q_{19}, and (d) D_3Q_{27} discrete velocity models.

neighboring lattice site in the assigned direction of particle velocity vector $\vec{e}_k$.

$$f_k(\vec{x}+\vec{e}_k\Delta t, t+\Delta t) = f_k^{'}(\vec{x},t) \tag{3.3}$$

where f_k and $f_k^{'}$ represent the particle distribution function at the pre-collision and post-collision states, respectively [Perumal and Dass, 2015]. The corresponding equation to obtain equilibrium distribution function f_k^{eq} is given as:

$$f_k^{eq} = w_k\rho\left[1+\frac{\vec{e}_k.\vec{u}}{c_s^2}+\frac{(\vec{e}_k\cdot\vec{u})^2}{2c_s^4}-\frac{\vec{u}\cdot\vec{u}}{2c_s^2}\right] \tag{3.4}$$

where, w is the weight factor, ρ is the fluid density , $\vec{u}$ = (u_x, u_y, u_z) is the macroscopic fluid velocity vector, and c_s is the speed of sound which is related to lattice speed, c, and equal to $c_s = \frac{c}{\sqrt{3}}$ for D_3Q_{15}, D_3Q_{19}, and D_3Q_{27} discrete velocity models. Also, the lattice speed, $c = \frac{\Delta x}{\Delta t}$, and Δx represent the size of the lattice and Δt is the time-step size. The corresponding discrete velocity vector $\vec{e}_k$ and weights w_k for the D_3Q_{15} lattice structure are given as:

$$\vec{e}_k = \begin{cases} c(\pm1,0,0), c(0,\pm1,0), c(0,0,\pm1), & k = 1....6 \\ c(\pm1,\pm1,\pm1), & k = 7....14 \\ c(0,0,0), & k = 15 \end{cases} \tag{3.5}$$

$$w_k = \begin{cases} \frac{1}{9}, & k = 1....6 \\ \frac{1}{72}, & k = 7....14 \\ \frac{2}{9}, & k = 15 \end{cases} \tag{3.6}$$

For D_3Q_{19} lattice structure, the discrete velocity vector $\vec{e}_k$ and weights w_k are expressed as:

$$\vec{e}_k = \begin{cases} c(\pm1,0,0), c(0,\pm1,0), c(0,0,\pm1), & k = 1....6 \\ c(\pm1,\pm1,0), c(\pm1,0,\pm1), c(0,\pm1,\pm1), & k = 7....18 \\ c(0,0,0), & k = 19 \end{cases} \tag{3.7}$$

$$w_k = \begin{cases} \frac{1}{18}, & k = 1....6 \\ \frac{1}{36}, & k = 7....18 \\ \frac{1}{3}, & k = 19 \end{cases} \tag{3.8}$$

For D_3Q_{27} lattice structure, the discrete velocity vector $\vec{e}_k$ and weights w_k are expressed as:

$$\vec{e}_k = \begin{cases} c(\pm1,0,0), c(0,\pm1,0), c(0,0,\pm1), & k = 1....6 \\ c(\pm1,\pm1,0), c(\pm1,0,\pm1), c(0,\pm1,\pm1), & k = 7....18 \\ c(\pm1,\pm1,\pm1), & k = 19....26 \\ c(0,0,0), & k = 27 \end{cases} \tag{3.9}$$

$$w_k = \begin{cases} \frac{2}{27}, & k = 1....6 \\ \frac{1}{54}, & k = 7....18 \\ \frac{1}{216}, & k = 19....26 \\ \frac{8}{27}, & k = 27 \end{cases} \tag{3.10}$$

The relaxation time parameter in Eqn. (3.1) depends on the kinematic viscosity of the fluid is given as:

$$\nu = \left(\frac{2\tau - 1}{6}\right) \frac{(\Delta x)^2}{\Delta t} \tag{3.11}$$

The hydrodynamic fields i.e. density ρ and momentum density $\rho\vec{u}$ can be calculated from the particle distribution function f_k as follows:

$$\rho = \sum_k f_k = \sum_k f_k^{eq},\ \rho\vec{u} = \sum_k \vec{e}_k f_k = \sum_k \vec{e}_k f_k^{eq} \tag{3.12}$$

3.1.2 LES Turbulent Model in LBM

An essential aspect of the present thesis work is the modeling of turbulent eddies, as the Reynolds number used in the simulations indicates a robust, turbulent flow. The direct simulation is not feasible due to the limitation of the computational resources. DNS would require a fine meshing of the domain and an enormous number of time steps to model the turbulent flow. Thus, LES is chosen in the present thesis work for the modeling of turbulent flow. LES has been widely accepted by researchers for the simulation of turbulent flows because it is flexible for implementation on complex geometries, provides comprehensive information for different turbulent statistics, and requires less computational power as compared to DNS [Ayranci *et al.*, 2012]. The idea behind the approach is to decompose the flow variables into large and small-scale structures by specifying a filtering procedure [Stephen B., 2000]. In LES, the process assumed that small-scale flow structures are universal and of isotropic nature (i.e., independent of the flow geometry). As a result, it provides an advantage to the method for modeling turbulent flow with relative ease [Derksen and Van den Akker, 1999]. The procedure enables large-scale structures to be resolved explicitly in grid calculation and uses the SGS model for the small-scale, turbulent structures. The general filtering operation is given as:

$$\overline{\phi}(x) = \int \phi(x') G(x,x') dx' \tag{3.13}$$

where ϕ is the spatial dependent quantity and G is the kernel function and integral is extended over the entire domain [Hou *et al.*, 1994; Koda and Lien, 2015]. The filtered SRT-LBM equation can be written as:

$$\overline{f}_k(\vec{x}+\vec{e}_k\Delta t, t+\Delta t) = \overline{f}_k(\vec{x},t) - \frac{1}{\tau_t}[\overline{f}_k(\vec{x},t) - \overline{f}_k^{eq}(\vec{x},t)] \tag{3.14}$$

where $\overline{f}_k^{eq}$ and $\overline{f}_k$ and the filtered quilibrium distribution function and particle distribution function, respectively. In the present thesis work, the SGS model (also known as the eddy-viscosity model) is adopted to resolve small-scale structures. The eddy viscosity term ν_{SGS} can be obtained from filter width Δ (with a size equal to grid spacing Δx) and characteristic filtered rate of strain $\overline{S}$. The expression for the same is given as:

$$\begin{aligned} \nu_{SGS} &= (C_s\Delta)^2\overline{S} \\ \overline{S} &= \sqrt{2\sum_{ij} S_{ij}S_{ij}} \end{aligned} \tag{3.15}$$

where C_s is the Smagorinsky constant, $S_{ij} = (\partial_j\vec{u}_i + \partial_i\vec{u}_j)$ is the filtered strain rate tensor. The subgrid closure can be implemented directly in the LBM equation by simply replacing physical kinematic viscosity ν, with the total effective viscosity ν_t in collision step [Koda and Lien, 2015]. The expression for total effective viscosity ν_t is given as:

$$\nu_t = \nu + \nu_{SGS} \tag{3.16}$$

In LBM, the viscosity of fluid is related to the relaxation time parameter as given in Eq.(3.11). Thus,

$$\nu_t = \left(\frac{2\tau_t - 1}{6}\right)\frac{(\Delta x)^2}{\Delta t} \tag{3.17}$$

on solving Eqn.(3.11),(3.15)-(3.17), we get:

$$\tau_t = \tau + \frac{3\Delta t(C_s\Delta)^2\overline{S}}{(\Delta x)^2} \tag{3.18}$$

where τ_t is total value of the relaxation time. The filtered strain rate tensor S_{ij} can be obtained directly from the non-equilibrium momentum flux tensor $\overline{\Pi}_{ij}$ given as:

$$\overline{\Pi}_{ij} = \sum_k \vec{e}_{ki}\vec{e}_{kj}(\overline{f}_i - \overline{f}_i^{eq}) = \frac{-2\overline{\rho}\tau_t(\Delta x)^2 S_{ij}}{3\Delta t} \tag{3.19}$$

Also,

$$Q^{1/2} = \sqrt{\overline{\Pi}_{ij} : \overline{\Pi}_{ij}} = \frac{\sqrt{2}\overline{\rho}\tau_t(\Delta x)^2\overline{S}}{3\Delta t} \tag{3.20}$$

Substituting Eq. (3.18) in Eq. (3.20) gives the expression for the characteristic filtered rate of strain $\overline{S}$:

$$\overline{S} = \frac{-\tau\overline{\rho}c\Delta x + \sqrt{(\tau\overline{\rho}c\Delta x)^2 + 18\sqrt{2}(C_s\Delta)^2 Q^{1/2}}}{6\overline{\rho}(C_s\Delta)^2} \tag{3.21}$$

Finally, on substituting Eq. (3.21) in Eq. (3.18) gives:

$$\tau_t = \frac{\tau}{2} + \frac{\sqrt{(\tau\overline{\rho}c\Delta x)^2 + 18\sqrt{2}(C_s\Delta)^2 Q^{1/2}}}{2\overline{\rho}c} \tag{3.22}$$

3.2 BOUNDARY CONDITIONS

Boundary conditions play a vital role in lattice Boltzmann simulation. An individual used distribution functions (f_k) to implement boundary conditions in LBM instead of using hydrodynamics variables [Mussa *et al.*, 2009]. Therefore, the appropriate mathematical expressions need to be determined to obtain the distribution functions at the boundary nodes. The researchers developed various methods to implement constant velocity inlet, no-slip, free-slip boundary conditions in the frame of LBM. The details of some of the boundary conditions used in the present thesis work are described below:

3.2.1 On-site Velocity Boundary Condition

Zou and He [1997] was the first who proposed the on-site velocity boundary condition for the D_2Q_9 lattice structure in order to simulate 2-D flow. The work presented by Zou and He [1997] also provides an overview of the on-site velocity boundary condition for the D_3Q_{15} lattice model for 3-D flow simulation. The work was further studied by Kutay *et al.* [2006] to demonstrate the velocity boundary condition for the D_3Q_{19} lattice model. The boundary condition proposed by Kutay *et al.* [2006] suffers from the limitation of inflow being perpendicular to the boundary plane. Later, Hecht and Harting [2010] modified the on-site velocity boundary condition with variable influx directions for the D_3Q_{19} lattice structure. The present section discussed the on-site velocity boundary conditions for the different three-dimension lattice structures of LBM. The geometry for the D_3Q_{15}, D_3Q_{19}, and D_3Q_{27} lattice structure are shown in Figure 3.1. The benchmark case of incompressible laminar flow through a 3-D square duct, as shown in Figure 3.2, has been chosen to derive the boundary condition. The mathematical expression for the on-site velocity boundary for each of the D_3Q_{15}, D_3Q_{19}, and D_3Q_{27} lattice structure can be written as:

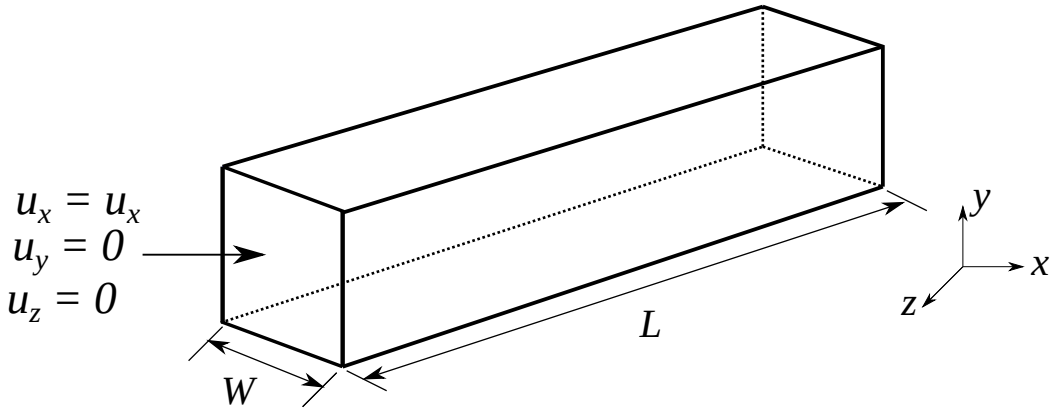

Figure 3.2 : Schematic representation of flow in 3D square duct

- **For D_3Q_{15} lattice structure**: The on-site velocity boundary condition for the D_3Q_{15} lattice structure can be expressed as follows:

  1. Consider the left boundary (i.e x = 0) as inlet as shown in Figure 3.2. The inlet is on the yz plane. The density ρ for the D_3Q_{15} lattice structure from Eqn.(3.12) can be written as:

$$\begin{aligned}\rho = {} & f_1 + f_2 + f_3 + f_4 + f_5 + f_6 + f_7 + f_8 + f_9 + f_{10} \\ & + f_{11} + f_{12} + f_{13} + f_{14} + f_{15}\end{aligned} \tag{3.23}$$

$$\begin{aligned}\rho u_x = {} & f_1 + f_7 + f_9 + f_{11} + f_{13} \\ & - (f_2 + f_8 + f_{10} + f_{12} + f_{14})\end{aligned} \tag{3.24}$$

  After the streaming steps in the LBE, the distribution functions f_k, $(k = 2,3,4,5,6,8,10,12,14,15)$ are known. The velocity components u_y = u_z = 0 are fixed at

inlet of the square duct. The velocity component u_x and unknown fluid populations, f_k, $(k = 1, 7, 9, 11, 13)$ needs to be determined. These can be obtained as follows:

On subtracting Eqn.(3.24) from Eqn.(3.23) we get

$$\rho = \frac{1}{1-u_x}\big[f_3 + f_4 + f_5 + f_6 + f_{15} + 2(f_2 + f_8 + f_{10} + f_{12} + f_{14})\big] \tag{3.25}$$

or

$$u_x = 1 - \frac{1}{\rho}\big[f_3 + f_4 + f_5 + f_6 + f_{15} + 2(f_2 + f_8 + f_{10} + f_{12} + f_{14})\big] \tag{3.26}$$

Considering the bounce-back rule suggested by Zou and He [1997] for the non-equilibrium part of the particle distribution function f_k (k = 1, 7, 9, 11, 13) we have:

$$f_1 - f_1^{eq} = f_2 - f_2^{eq} \tag{3.27}$$

It gives:

$$f_1 = f_2 + \frac{2}{3}\rho u_x \tag{3.28}$$

Also,

$$f_7 = f_8 + + \frac{1}{12}\rho u_x - \frac{1}{4}\big[(f_3 - f_4) + (f_5 - f_6)\big] \tag{3.29}$$

$$f_9 = f_1 0 + + \frac{1}{12}\rho u_x - \frac{1}{4}\big[(f_3 - f_4) - (f_5 - f_6)\big] \tag{3.30}$$

$$f_1 1 = f_1 2 + + \frac{1}{12}\rho u_x - \frac{1}{4}\big[-(f_3 - f_4) + (f_5 - f_6)\big] \tag{3.31}$$

$$f_1 3 = f_1 4 + + \frac{1}{12}\rho u_x - \frac{1}{4}\big[-(f_3 - f_4) - (f_5 - f_6)\big] \tag{3.32}$$

The on-site velocity boundary conditions for the other sides of the geometry can be obtained using the same approach and similarly, we can derive the expressions for the unknown distribution functions in the D_3Q_{19} and D_3Q_{27} lattice structure. These are given as follows:

- **For D_3Q_{19} lattice structure**: Hecht and Harting [2010] presented the on-site velocity boundary condition for the D_3Q_{19} lattice structure. The mathematical expressions are given as:

  1. **At the left boundary (i.e x = 0) as inlet**:

$$\rho = \frac{1}{1-u_x}\big[f_3 + f_4 + f_5 + f_6 + f_{15} + f_{16} + f_{17} + f_{18} + f_{19} + 2(f_2 + f_{11} + f_{12} + f_{13} + f_{14})\big] \tag{3.33}$$

  or

$$u_x = 1 - \frac{1}{\rho}\big[f_3 + f_4 + f_5 + f_6 + f_{15} + f_{16} + f_{17} + f_{18} + f_{19} + 2(f_2 + f_{11} + f_{12} + f_{13} + f_{14})\big] \tag{3.34}$$

and

$$f_1 = f_2 + \frac{1}{3}\rho u_x \tag{3.35}$$

Similarly, we get

$$f_8 = f_{11} + \frac{\rho}{6}(u_x - u_y) + N_y^x \tag{3.36}$$

$$f_7 = f_{12} + \frac{\rho}{6}(u_x + u_y) - N_y^x \tag{3.37}$$

$$f_9 = f_{14} + \frac{\rho}{6}(u_x + u_z) - N_z^x \tag{3.38}$$

$$f_{10} = f_{13} + \frac{\rho}{6}(u_x - u_z) + N_z^x \tag{3.39}$$

where

$$N_y^x = \frac{1}{2}\left[f_3 + f_{15} + f_{16} - (f_4 + f_{17} + f_{18})\right] - \frac{1}{3}\rho u_y \tag{3.40}$$

$$N_z^x = \frac{1}{2}\left[f_5 + f_{11} + f_{15} - (f_6 + f_{16} + f_{18})\right] - \frac{1}{3}\rho u_z \tag{3.41}$$

2. **For the right boundary ((i.e. x = n_x) as outlet**:

$$\begin{aligned}\rho = \frac{1}{u_x + 1}\big[&f_3 + f_4 + f_5 + f_6 + f_{15} + f_{16} + f_{17} + f_{18} + f_{19} \\ &+ 2(f_1 + f_7 + f_8 + f_9 + f_{10})\big]\end{aligned} \tag{3.42}$$

or

$$\begin{aligned}u_x = -1 + \frac{1}{\rho}\big[&f_3 + f_4 + f_5 + f_6 + f_{15} + f_{16} + f_{17} + f_{18} + f_{19} \\ &+ 2(f_1 + f_7 + f_8 + f_9 + f_{10})\big]\end{aligned} \tag{3.43}$$

and

$$f_2 = f_1 - \frac{1}{3}\rho u_x \tag{3.44}$$

$$f_{11} = f_8 + \frac{\rho}{6}(u_y - u_x) - N_y^x \tag{3.45}$$

$$f_{12} = f_7 + \frac{\rho}{6}(-u_x - u_y) + N_y^x \tag{3.46}$$

$$f_{14} = f_9 + \frac{\rho}{6}(-u_x - u_z) + N_z^x \tag{3.47}$$

$$f_{13} = f_{10} + \frac{\rho}{6}(u_z - u_x) - N_z^x \tag{3.48}$$

3. **For the front boundary ((i.e. y = 0) as inlet**:

$$\begin{aligned}\rho = \frac{1}{1 - u_y}\big[&f_1 + f_2 + f_5 + f_6 + f_9 + f_{10} + f_{13} + f_{14} + f_{19} \\ &+ 2(f_4 + f_8 + f_{12} + f_{17} + f_{18})\big]\end{aligned} \tag{3.49}$$

or

$$u_y = 1 - \frac{1}{\rho}\big[f_1 + f_2 + f_5 + f_6 + f_9 + f_{10} + f_{13} + f_{14} + f_{19} + 2(f_4 + f_8 + f_{12} + f_{17} + f_{18})\big] \tag{3.50}$$

and

$$f_3 = f_4 + \frac{1}{3}\rho u_y \tag{3.51}$$

$$f_7 = f_{12} + \frac{\rho}{6}(u_y + u_x) - N_x^y \tag{3.52}$$

$$f_{11} = f_8 + \frac{\rho}{6}(u_y - u_x) + N_x^y \tag{3.53}$$

$$f_{15} = f_{18} + \frac{\rho}{6}(u_y + u_z) - N_z^y \tag{3.54}$$

$$f_{16} = f_{17} + \frac{\rho}{6}(u_y - u_z) + N_z^y \tag{3.55}$$

where

$$N_x^y = \frac{1}{2}\big[f_1 + f_9 + f_{10} - (f_2 + f_{13} + f_{14})\big] - \frac{1}{3}\rho u_x \tag{3.56}$$

$$N_z^y = \frac{1}{2}\big[f_5 + f_9 + f_{13} - (f_6 + f_{10} + f_{14})\big] - \frac{1}{3}\rho u_z \tag{3.57}$$

4. **At the back boundary ((i.e. y = n_y) as outlet**:

$$\rho = \frac{1}{u_y + 1}\big[f_1 + f_2 + f_5 + f_6 + f_9 + f_{10} + f_{13} + f_{14} + f_{19} + 2(f_3 + f_7 + f_{11} + f_{15} + f_{16})\big] \tag{3.58}$$

or

$$u_y = \frac{1}{1 - \rho}\big[f_1 + f_2 + f_5 + f_6 + f_9 + f_{10} + f_{13} + f_{14} + f_{19} + 2(f_3 + f_7 + f_{11} + f_{15} + f_{16})\big] \tag{3.59}$$

and

$$f_4 = f_3 - \frac{1}{3}\rho u_y \tag{3.60}$$

$$f_{12} = f_7 + \frac{\rho}{6}(-u_y - u_x) + N_x^y \tag{3.61}$$

$$f_8 = f_{11} + \frac{\rho}{6}(-u_y + u_x) - N_x^y \tag{3.62}$$

$$f_{18} = f_{15} + \frac{\rho}{6}(-u_y - u_z) + N_z^y \tag{3.63}$$

$$f_{17} = f_{16} + \frac{\rho}{6}(-u_y + u_z) - N_z^y \tag{3.64}$$

5. **For the bottom boundary ((i.e. z = 0) as inlet**:

$$\rho = \frac{1}{1-u_z}\big[f_1+f_2+f_3+f_4+f_7+f_8+f_{11}+f_{12}+f_{19} \\ +2(f_6+f_{10}+f_{14}+f_{16}+f_{18})\big] \tag{3.65}$$

or

$$u_z = 1-\frac{1}{\rho}\big[f_1+f_2+f_3+f_4+f_7+f_8+f_{11}+f_{12}+f_{19} \\ +2(f_6+f_{10}+f_{14}+f_{16}+f_{18})\big] \tag{3.66}$$

and

$$f_5 = f_6+\frac{1}{3}\rho u_z \tag{3.67}$$

$$f_9 = f_{14}+\frac{\rho}{6}(u_z+u_x)-N_x^z \tag{3.68}$$

$$f_{13} = f_{10}+\frac{\rho}{6}(u_z-u_x)+N_x^z \tag{3.69}$$

$$f_{15} = f_{18}+\frac{\rho}{6}(u_z+u_y)-N_y^z \tag{3.70}$$

$$f_{17} = f_{16}+\frac{\rho}{6}(u_z-u_y)+N_y^z \tag{3.71}$$

where

$$N_x^z = \frac{1}{2}\big[f_1+f_7+f_8-(f_2+f_{11}+f_{12})\big]-\frac{1}{3}\rho u_x \tag{3.72}$$

$$N_y^z = \frac{1}{2}\big[f_3+f_7+f_{11}-(f_4+f_8+f_{12})\big]-\frac{1}{3}\rho u_y \tag{3.73}$$

6. **For the top boundary ((i.e. z = n_z) as outlet**:

$$\rho = \frac{1}{1-u_z}\big[f_1+f_2+f_3+f_4+f_7+f_8+f_{11}+f_{12}+f_{19} \\ +2(f_5+f_9+f_{13}+f_{15}+f_{17})\big] \tag{3.74}$$

or

$$u_z = -1+\frac{1}{\rho}\big[f_1+f_2+f_3+f_4+f_7+f_8+f_{11}+f_{12}+f_{19} \\ +2(f_5+f_9+f_{13}+f_{15}+f_{17})\big] \tag{3.75}$$

and

$$f_6 = f_5-\frac{1}{3}\rho u_z \tag{3.76}$$

$$f_{10} = f_{13}+\frac{\rho}{6}(-u_z+u_x)+N_x^z \tag{3.77}$$

$$f_{14} = f_9+\frac{\rho}{6}(-u_z-u_x)-N_x^z \tag{3.78}$$

$$f_{16} = f_{17}+\frac{\rho}{6}(-u_z+u_y)+N_y^z \tag{3.79}$$

$$f_{18} = f_{15}+\frac{\rho}{6}(-u_z-u_y)-N_y^z \tag{3.80}$$

- **For D_3Q_{27} lattice structure**:

  1. **At the left boundary (i.e x = 0) as inlet**:

$$\begin{aligned}\rho = \frac{1}{1-u_x}\big[&f_3+f_4+f_5+f_6+f_{15}\\&+f_{16}+f_{17}+f_{18}+f_{19}+2(f_2+f_{11}+f_{12}\\&+f_{13}+f_{14}+f_{21}+f_{23}+f_{25}+f_{27})\big]\end{aligned} \tag{3.81}$$

  or

$$\begin{aligned}u_x = 1-\frac{1}{\rho}\big[&f_3+f_4+f_5+f_6+f_{15}\\&+f_{16}+f_{17}+f_{18}+f_{19}+2(f_2+f_{11}+f_{12}\\&+f_{13}+f_{14}+f_{21}+f_{23}+f_{25}+f_{27})\big]\end{aligned} \tag{3.82}$$

$$f_1 = f_2+\frac{4}{9}\rho u_x \tag{3.83}$$

  Similarly, we get

$$f_7 = f_{12}+\frac{\rho}{9}(u_x+u_y)-N_y^x \tag{3.84}$$

$$f_8 = f_{11}+\frac{\rho}{9}(u_x-u_y)+N_y^x \tag{3.85}$$

$$f_9 = f_{14}+\frac{\rho}{9}(u_x+u_z)-N_z^x \tag{3.86}$$

$$f_{10} = f_{13}+\frac{\rho}{9}(u_x-u_z)+N_z^x \tag{3.87}$$

$$f_{20} = f_{21}+\frac{\rho}{36}\big[u_x+(u_y+u_z)\big]-N_y^x-N_z^x \tag{3.88}$$

$$f_{22} = f_{23}+\frac{\rho}{36}\big[u_x+(u_y-u_z)\big]-N_y^x+N_z^x \tag{3.89}$$

$$f_{24} = f_{25}+\frac{\rho}{36}\big[u_x-(u_y-u_z)\big]+N_y^x-N_z^x \tag{3.90}$$

$$f_{26} = f_{27}+\frac{\rho}{36}\big[u_x-(u_y+u_z)\big]+N_y^x+N_z^x \tag{3.91}$$

  where

$$N_y^x = \frac{1}{6}\big[f_3+f_{15}+f_{16}-(f_4+f_{17}+f_{18})\big]-\frac{1}{9}\rho u_y \tag{3.92}$$

$$N_z^x = \frac{1}{6}\big[f_5+f_{15}+f_{17}-(f_6+f_{16}+f_{18})\big]-\frac{1}{9}\rho u_z \tag{3.93}$$

  Similar to the left boundary, the on-site velocity boundary conditions on other sides for the D_3Q_{27} lattice structure is given as:

  2. **At the right boundary (i.e. x = n_x) as outlet**: we get

$$\begin{aligned}\rho = \frac{1}{u_x+1}\big[&f_3+f_4+f_5+f_6+f_{15}+f_{16}+f_{17}+f_{18}+f_{19}\\&+2(f_1+f_7+f_8+f_9+f_{10}+f_{20}+f_{22}+f_{24}+f_{26})\big]\end{aligned} \tag{3.94}$$

gives

$$u_x = -1 + \frac{1}{\rho}\big[f_3 + f_4 + f_5 + f_6 + f_{15} + f_{16} + f_{17} + f_{18} + f_{19} + 2(f_1 + f_7 + f_8 + f_9 + f_{10} + f_{20} + f_{22} + f_{24} + f_{26})\big] \tag{3.95}$$

And, the unknown distributions are:

$$f_2 = f_1 - \frac{4}{9}\rho u_x \tag{3.96}$$

And,

$$f_{12} = f_7 - \frac{\rho}{9}(u_y + u_x) + N_y^x \tag{3.97}$$

$$f_{11} = f_8 + \frac{\rho}{9}(u_y - u_x) - N_y^x \tag{3.98}$$

$$f_{14} = f_9 - \frac{\rho}{9}(u_z + u_x) + N_z^x \tag{3.99}$$

$$f_{13} = f_{10} + \frac{\rho}{9}(u_z - u_x) - N_z^x \tag{3.100}$$

$$f_{21} = f_{20} - \frac{\rho}{36}\big[u_x + (u_y + u_z)\big] + N_y^x + N_z^x \tag{3.101}$$

$$f_{23} = f_{22} - \frac{\rho}{36}\big[u_x + (u_y - u_z)\big] + N_y^x - N_z^x \tag{3.102}$$

$$f_{25} = f_{24} - \frac{\rho}{36}\big[u_x - (u_y - u_z)\big] - N_y^x + N_z^x \tag{3.103}$$

$$f_{27} = f_{26} - \frac{\rho}{36}\big[u_x - (u_y + u_z)\big] - N_y^x - N_z^x \tag{3.104}$$

3. **At the front boundary (i.e. y = 0) as inlet**: we obtain

$$\rho = \frac{1}{1 - u_y}\big[f_1 + f_2 + f_5 + f_6 + f_9 + f_{10} + f_{13} + f_{14} + f_{19} + 2(f_4 + f_8 + f_{12} + f_{17} + f_{18} + f_{21} + f_{23} + f_{24} + f_{26})\big] \tag{3.105}$$

gives

$$u_y = 1 - \frac{1}{\rho}\big[f_1 + f_2 + f_5 + f_6 + f_9 + f_{10} + f_{13} + f_{14} + f_{19} + 2(f_4 + f_8 + f_{12} + f_{17} + f_{18} + f_{21} + f_{23} + f_{24} + f_{26})\big] \tag{3.106}$$

And, the unknown density distribution functions are:

$$f_3 = f_4 + \frac{4}{9}\rho u_y \tag{3.107}$$

Also,

$$f_7 = f_{12} + \frac{\rho}{9}(u_y + u_x) - N_x^y \tag{3.108}$$

$$f_{11} = f_8 + \frac{\rho}{9}(u_y - u_x) + N_x^y \tag{3.109}$$

$$f_{15} = f_{18} + \frac{\rho}{9}(u_y + u_z) - N_z^y \tag{3.110}$$

$$f_{16} = f_{17} + \frac{\rho}{9}(u_y - u_z) + N_z^y \tag{3.111}$$

$$f_{20} = f_{21} + \frac{\rho}{36}\left[u_y + (u_x + u_z)\right] - N_x^y - N_z^y \tag{3.112}$$

$$f_{22} = f_{23} + \frac{\rho}{36}\left[u_y + (u_x - u_z)\right] - N_x^y + N_z^y \tag{3.113}$$

$$f_{25} = f_{24} + \frac{\rho}{36}\left[u_y - (u_x + u_z)\right] + N_x^y + N_z^y \tag{3.114}$$

$$f_{27} = f_{26} + \frac{\rho}{36}\left[u_y - (u_x - u_z)\right] + N_x^y - N_z^y \tag{3.115}$$

where

$$N_x^y = \frac{1}{6}\left[f_1 + f_9 + f_{10} - (f_2 + f_{13} + f_{14})\right] - \frac{1}{9}\rho u_x \tag{3.116}$$

$$N_z^y = \frac{1}{6}\left[f_5 + f_9 + f_{13} - (f_6 + f_{10} + f_{14})\right] - \frac{1}{9}\rho u_z \tag{3.117}$$

4. **At the back boundary (i.e. y = n_y) as outlet**: we have

$$\begin{aligned}\rho = \frac{1}{u_y + 1}\big[&f_1 + f_2 + f_5 + f_6 + f_9 + f_{10} + f_{13} + f_{14} + f_{19} \\ &+ 2(f_3 + f_7 + f_{11} + f_{15} + f_{16} + f_{20} + f_{22} + f_{25} + f_{27})\big]\end{aligned} \tag{3.118}$$

gives

$$\begin{aligned}u_y = -1 + \frac{1}{\rho}\big[&f_1 + f_2 + f_5 + f_6 + f_9 + f_{10} + f_{13} + f_{14} + f_{19} \\ &+ 2(f_3 + f_7 + f_{11} + f_{15} + f_{16} + f_{20} + f_{22} + f_{25} + f_{27})\big]\end{aligned} \tag{3.119}$$

And, the unknown fluid populations are:

$$f_4 = f_3 - \frac{4}{9}\rho u_y \tag{3.120}$$

Also,

$$f_{12} = f_7 - \frac{\rho}{9}(u_x + u_y) + N_x^y \tag{3.121}$$

$$f_8 = f_{11} + \frac{\rho}{9}(u_x - u_y) - N_x^y \tag{3.122}$$

$$f_{18} = f_{15} - \frac{\rho}{9}(u_z + u_y) + N_z^y \tag{3.123}$$

$$f_{17} = f_{16} + \frac{\rho}{9}(u_z - u_y) - N_z^y \tag{3.124}$$

$$f_{21} = f_{20} - \frac{\rho}{36}\left[u_y + (u_x + u_z)\right] + N_x^y + N_z^y \tag{3.125}$$

$$f_{23} = f_{22} - \frac{\rho}{36}\left[u_y + (u_x - u_z)\right] + N_x^y - N_z^y \tag{3.126}$$

$$f_{24} = f_{25} - \frac{\rho}{36}\left[u_y - (u_x + u_z)\right] - N_x^y - N_z^y \tag{3.127}$$

$$f_{26} = f_{27} - \frac{\rho}{36}\left[u_y - (u_x - u_z)\right] - N_x^y + N_z^y \tag{3.128}$$

5. **At the bottom boundary (i.e. z = 0) as inlet**:

The density ρ expression is given by

$$\rho = \frac{1}{1-u_z}\big[f_1+f_2+f_3+f_4+f_7+f_8+f_{11}+f_{12}+f_{19} \\ +2(f_6+f_{10}+f_{14}+f_{16}+f_{18}+f_{21}+f_{22}+f_{25}+f_{26})\big] \tag{3.129}$$

gives

$$u_z = 1-\frac{1}{\rho}\big[f_1+f_2+f_3+f_4+f_7+f_8+f_{11}+f_{12}+f_{19} \\ +2(f_6+f_{10}+f_{14}+f_{16}+f_{18}+f_{21}+f_{22}+f_{25}+f_{26})\big] \tag{3.130}$$

Thus,

$$f_5 = f_6+\frac{4}{9}\rho u_z \tag{3.131}$$

Also,

$$f_9 = f_{14}+\frac{\rho}{9}(u_z+u_x)-N_x^z \tag{3.132}$$

$$f_{13} = f_{10}+\frac{\rho}{9}(u_z-u_x)+N_x^z \tag{3.133}$$

$$f_{15} = f_{18}+\frac{\rho}{9}(u_z+u_y)-N_y^z \tag{3.134}$$

$$f_{17} = f_{16}+\frac{\rho}{9}(u_z-u_y)+N_y^z \tag{3.135}$$

$$f_{20} = f_{21}+\frac{\rho}{36}\big[u_z+(u_x+u_y)\big]-N_x^z-N_y^z \tag{3.136}$$

$$f_{23} = f_{22}+\frac{\rho}{36}\big[u_z-(u_x+u_y)\big]+N_x^z+N_y^z \tag{3.137}$$

$$f_{24} = f_{25}+\frac{\rho}{36}\big[u_z+(u_x-u_y)\big]-N_x^z+N_y^z \tag{3.138}$$

$$f_{27} = f_{26}+\frac{\rho}{36}\big[u_z-(u_x-u_y)\big]+N_x^z-N_y^z \tag{3.139}$$

where

$$N_x^z = \frac{1}{6}\big[f_1+f_7+f_8-(f_2+f_{11}+f_{12})\big]-\frac{1}{9}\rho u_x \tag{3.140}$$

$$N_y^z = \frac{1}{6}\big[f_3+f_7+f_{11}-(f_4+f_8+f_{12})\big]-\frac{1}{9}\rho u_y \tag{3.141}$$

6. **At the top (i.e. z = n_z) boundary as outlet**: we have

$$\rho = \frac{1}{u_z+1}\big[f_1+f_2+f_3+f_4+f_7+f_8+f_{11}+f_{12}+f_{19} \\ +2(f_5+f_9+f_{13}+f_{15}+f_{17}+f_{20}+f_{23}+f_{24}+f_{27})\big] \tag{3.142}$$

This can be rewritten as:

$$u_z = -1 + \frac{1}{\rho}\big[f_1 + f_2 + f_3 + f_4 + f_7 + f_8 + f_{11} + f_{12} + f_{19} + 2(f_5 + f_9 + f_{13} + f_{15} + f_{17} + f_{20} + f_{23} + f_{24} + f_{27})\big] \tag{3.143}$$

The unknown density distribution functions can be computed as:

$$f_6 = f_5 - \frac{4}{9}\rho u_z \tag{3.144}$$

Also,

$$f_{14} = f_9 - \frac{\rho}{9}(u_x + u_z) + N_x^z \tag{3.145}$$

$$f_{10} = f_{13} + \frac{\rho}{9}(u_x - u_z) - N_x^z \tag{3.146}$$

$$f_{18} = f_{15} - \frac{\rho}{9}(u_y + u_z) + N_y^z \tag{3.147}$$

$$f_{16} = f_{17} + \frac{\rho}{9}(u_y - u_z) - N_y^z \tag{3.148}$$

$$f_{21} = f_{20} - \frac{\rho}{36}\big[u_z + (u_x + u_y)\big] + N_x^z + N_y^z \tag{3.149}$$

$$f_{22} = f_{23} - \frac{\rho}{36}\big[u_z - (u_x + u_y)\big] - N_x^z - N_y^z \tag{3.150}$$

$$f_{25} = f_{24} - \frac{\rho}{36}\big[u_z + (u_x - u_y)\big] + N_x^z - N_y^z \tag{3.151}$$

$$f_{26} = f_{27} - \frac{\rho}{36}\big[u_z - (u_x - u_y)\big] - N_x^z + N_y^z \tag{3.152}$$

3.2.2 Bounce-Back Boundary Conditions

The BB boundary condition is the most commonly used boundary condition in LBM to obtain a no-slip condition at the boundary walls. The key idea is to BB fluid particles in the opposite direction once the fluid particles reach the boundary. There are several ways to implement the BB schemes at the boundary. These are explained as below:

3.2.2 Full way bounce-back

The scheme is also referred to as the standard BB method [Guo and Shu, 2013]. The full way BB method is the easiest to implement. In this method, the lattice points are located on the fluid boundary, and after the streaming process, the unknown fluid populations at the boundary nodes take the value of the fluid populations opposite in direction, as shown in Figure 3.3.

The method sees no collision operation on the fluid node at the wall boundary during its implementation. The method provides the first-order accuracy to the solution. Despite the popularity of this scheme due to its simplicity, the scheme is not flawless since it is not truly mass-conservative. The scheme can be defined mathematically as:

$$f_k(\vec{x}, t + \Delta t) = f_{\bar{k}}(\vec{x}, t + \Delta t) \tag{3.153}$$

where, f is the post-streaming state of the distribution function, and $(k, \bar{k})$ are the distribution functions (fluid population) in the direction opposite to each other.

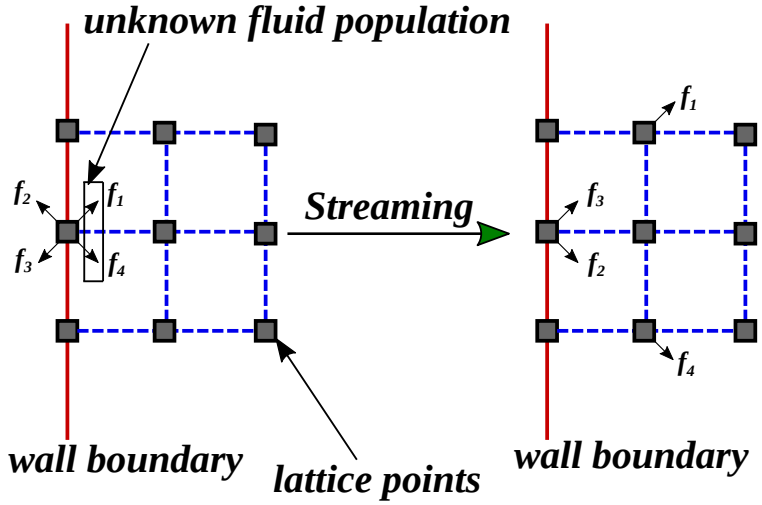

Figure 3.3 : 2D representation of the full way bounce-back method before (left) and after (right) streaming process.

3.2.2 Half way bounce-back

In this approach, wall boundary is simply placed at a half distance between two lattice sites. In other words, the wall boundary is located in between the ghost nodes and fluid nodes (or lattice points) as shown in Figure 3.4. The collision operation is performed on all lattice sites. The method is also called as bounce-back on the link (BBL) [Behrend, 1995]. Moreover, the significant features of this boundary condition that it can provide second order accuracy and also conserve the mass at the boundary wall. The scheme is defined with the expression given as:

$$f_k(\vec{x}, t + \Delta t) = f_{\bar{k}}(\vec{x}, t^+) \tag{3.154}$$

where $f_{\bar{k}}(\vec{x}, t^+)$ represents the post-collision distribution function.

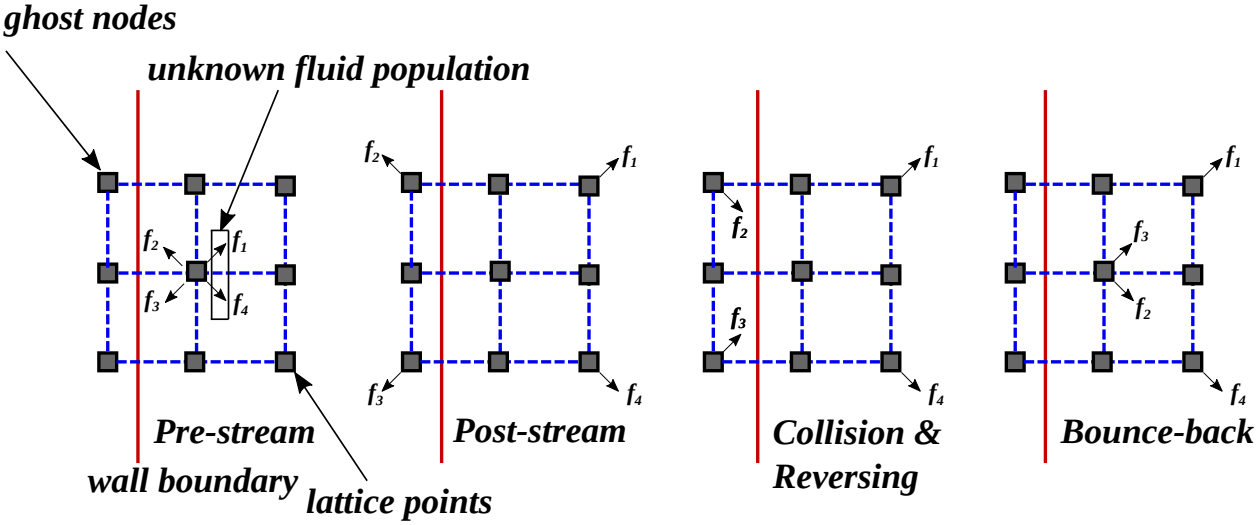

Figure 3.4 : 2D representation of the half way bounce-back method

3.2.2 Modified bounce-back

The implementation of the modified BB boundary condition is similar to the full-way bounce-back method. It differs only in the sense that it includes collision operation at the wall nodes during the process.

3.2.3 Free-Slip Boundary Condition

The boundary condition is also known as specular reflection. The boundary condition is generally used to the situation of a smooth boundaries of zero friction. In the case of free-slip boundary condition, the implementation is similar to that used in the full-way BB boundary condition. However, instead of performing the complete reflection, the outgoing particle distribution functions are reoriented via specular reflection as shown in Figure 3.5.

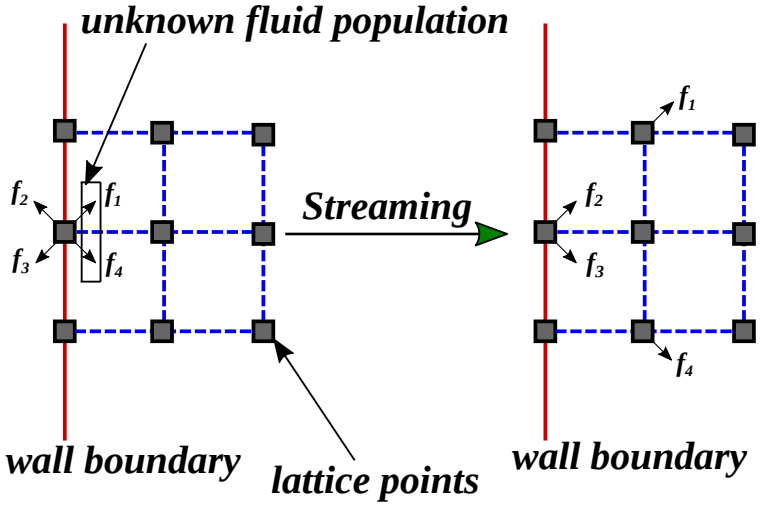

Figure 3.5 : 2D representation of the free-slip boundary condition before (left) and after (right) streaming process.

The mathematical formulation for the scheme can be written as:

$$f_k(\vec{x}, t+\Delta t) = f_{\bar{k}}(\vec{x}, t+\Delta t) \tag{3.155}$$

where, $f_{\bar{k}}$ is the specular reflection of the unknown fluid populations at the boundary nodes.

3.2.4 Immersed Boundary Method

The IB method can be described as a non-body conformal grid method for implementing no-slip conditions at the boundary surface by adding a forcing term to the governing flow equation either explicitly or implicitly. The concept behind the method is that the boundary nodes are represented as Lagrangian markers independent of the mesh used in flow solver [Peng and Luo, 2008] as shown in Figure 3.6. Additionally, the IB method needs interface schemes since the boundary nodes generally do not correspond to the Eulerian grid nodes. The most popular interface scheme for the IB method is the diffuse interface scheme. In the diffuse interface scheme, the Lagrangian markers are located on the boundary surface at which the boundary force is evaluated, and the Eulerian grid nodes represent the flow field. Hence, interpolation between the Lagrangian markers and Eulerian nodes is required to interpolate the fluid velocity at the neighboring Eulerian nodes on boundary nodes for calculating the force exerted by the flow on the boundary surface and for the distribution of boundary force on the neighboring Eulerian nodes. The distributed forces are added as an external force term in the governing fluid flow equations.

The governing LBE for the SRT-LBM in the presence of an external force, can be rewritten as [Kang and Hassan, 2011]:

$$f_k(\vec{x}+\vec{e}_k\Delta t, t+\Delta t) = f_k(\vec{x},t) - \frac{1}{\tau}[f_k(\vec{x},t) - f_k^{eq}(\vec{x},t)] + F_k(\vec{x},t)\Delta t \tag{3.156}$$

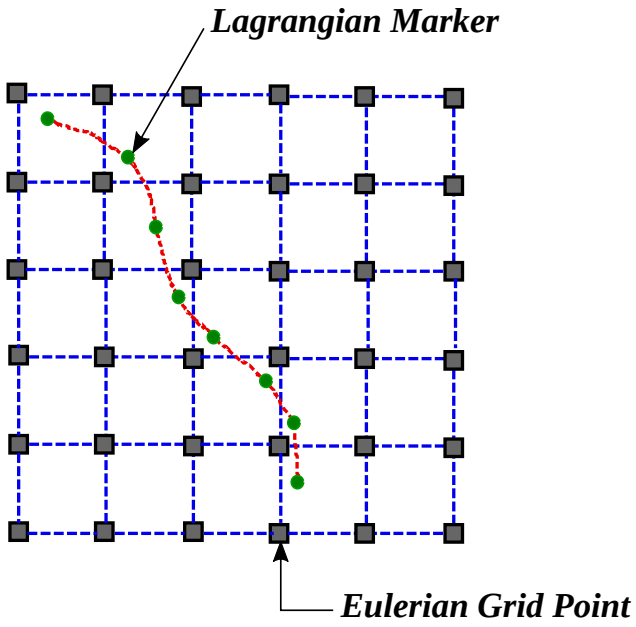

Figure 3.6 : Illustration of immersed boundary method.

where F_k is the discrete force distribution function along direction k, that can be computed with the given expression [Kang and Hassan, 2011]:

$$F_k(\vec{x},t) = \left(1 - \frac{1}{2\tau}\right) w_k \left[\frac{\vec{e}_k - \vec{u}(\vec{x},t)}{c_s^2} + \frac{\vec{e}_k \cdot \vec{u}(\vec{x},t)}{c_s^4}\vec{e}_k\right] \cdot \mathbf{F}(\vec{x},t) \tag{3.157}$$

Moreover, the following steps are used in the numerical calculations to solve the LBE with a forcing term [Guo *et al.*, 2002; Kang and Hassan, 2011].

- **First-forcing step**:

$$\rho(\vec{x},t)\vec{u}(\vec{x},t) = \sum_k \vec{e}_k f_k(\vec{x},t) + \frac{\Delta t}{2}\mathbf{F}(\vec{x},t) \tag{3.158}$$

- **Collision step**:

$$f_k^{'}(\vec{x},t) = f_k(\vec{x},t) - \frac{1}{\tau}[f_k(\vec{x},t) - f_k^{eq}(\vec{x},t)] \tag{3.159}$$

- **Second-forcing step**:

$$f_k^{''}(\vec{x},t) = f_k^{'}(\vec{x},t) + \Delta t F_k(\vec{x},t) \tag{3.160}$$

- **Streaming step**:

$$f_k(\vec{x}+\vec{e}_k\Delta t, t+\Delta t) = f_k^{''}(\vec{x},t) \tag{3.161}$$

where $f_k^{'}$ and $f_k^{''}$ are defined as the post-collision and post-forcing distribution functions, respectively. However, the forcing term on the right hand side of Eq.(3.157) is the boundary force distribution on the neighboring Eulerian nodes. This can be computed with the following procedure:

i. Firstly, the unforced velocity $\vec{U}_b^{uf}$ at the boundary nodes $\vec{x}_b$ is obtained by interpolating the unforced fluid velocity $\vec{u}^{uf}$ from the neighboring Eulerian nodes. This can be given as:

$$\vec{U}_b^{uf} = \sum_{i,j,k} \vec{u}_{ijk}^{uf} D_f(\vec{x}_{ijk} - \vec{x}_b)\Delta x \Delta y \Delta z \tag{3.162}$$

where, D_f is the cheap-clipped polynomial mapping function [Deen *et al.*, 2004], $\vec{x}$ is the position vector of the Eulerian fluid nodes, and $\vec{x}_b$ represent the position vector of the control points on the boundary surface of the reactor components. The mathematical expression for the cheap-clipped polynomial mapping function can be written as:

$$D_f(\vec{x}_{ijk} - \vec{x}_b) = d\Big(x_i - x_b\Big)d\Big(y_j - y_b\Big)d\Big(z_k - z_b\Big) \tag{3.163}$$

And,

$$d(x_i - x_b) = \begin{cases} \frac{15}{16}\left[\frac{(x_i - x_b)^5}{n^5} - 2\frac{(x_i - x_b)^2}{n^3} + \frac{1}{n}\right] & -n \leq (x_i - x_b) \leq +n \\ 0, & otherwise \end{cases} \tag{3.164}$$

ii. Then, the forces on the boundary nodes $\vec{F}_b$ are obtained using the expression given below:

$$\vec{F}_b = 2\rho \frac{\vec{U}_b - \vec{U}_b^{uf}}{\Delta t} \tag{3.165}$$

where $\vec{U}_b$ is the velocity vector on the lagrangian markers at boundary surface.

iii. Finally, forcing term **F** on the right-hand side of equation Eq.(3.157) for the distribution of the boundary forces $\vec{F}_b$ on the neighboring Eulerian nodes can be computed as:

$$\mathbf{F} = \sum_b \vec{F}_b D_f(\vec{x}_{ijk} - \vec{x}_b)\Delta x \tag{3.166}$$

3.3 GPU PROGRAMMING

3.3.1 Architecture Details of NVIDIA Tesla GP100 GPU

The simulations for the present thesis work have been carried out on a Tesla P100 accelerator of NVIDIA GP100 GPU card.

As shown in Figure 3.7, the NVIDIA GP100 architecture contains Graphical Processing Clusters (GPCs), Texture Processing Clusters (TPCs), Streaming Multiprocessors (SMs), and memory controllers. A complete GP100 is made up of 6 GPCs, 30 TPCs, 60 Pascal SMs. It consists of eight memory controllers of 512 bits each. (total of 4096 bits). Each GPC comprises five TPCs, each of which includes two SMs. Each SM consists of 32 double-precision CUDA cores that is half of the single-precision CUDA cores and four texture units as illustrated in Figure 3.8. A complete GP100 GPU features has 1920 double-precision CUDA cores (also 3840 single precision CUDA cores) and 240 texture units over 60 SMs. Each memory controller has 512 KB of L2 cache linked to it. Morever, each HBM2 DRAM stack is managed by two memory controllers. The entire GPU is comprised of a total of 4096 KB of L2 cache. The Tesla P100 accelerator employs 56 SMs. For more details about the architecture of the Tesla GP100 card, one can refer to NVIDIA [2016]. The technical specifications of the NVIDIA Tesla GP100 GPU are given in Table 3.1.

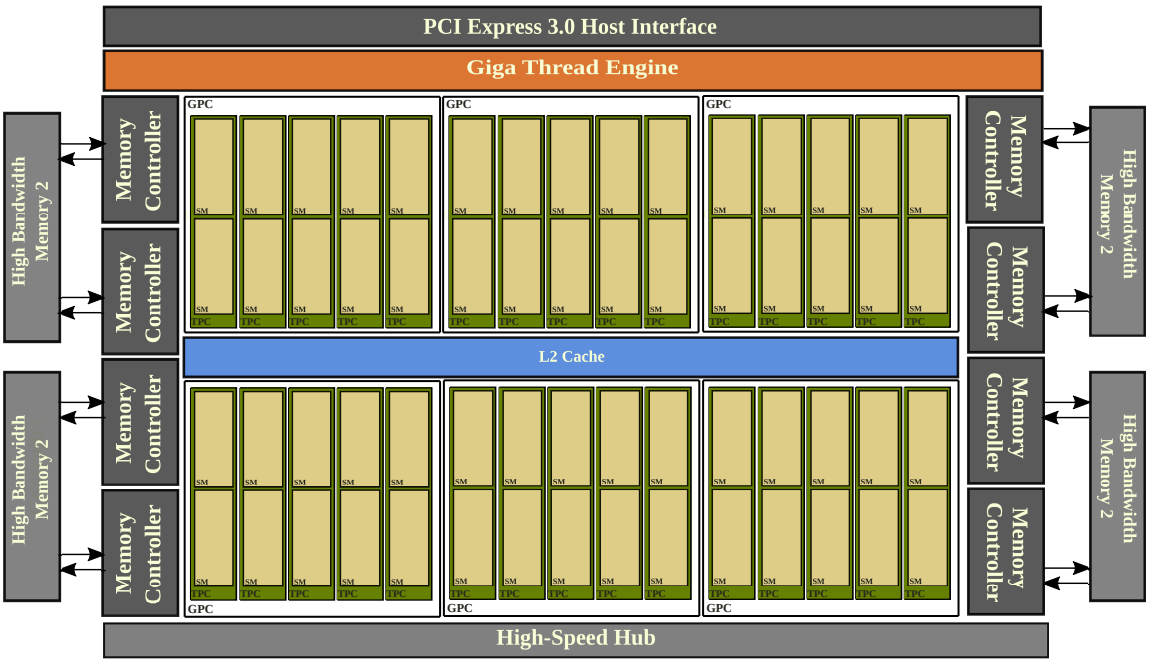

Figure 3.7 : Architecture of Tesla GP100.



Figure 3.8 : Streaming Multiprocessor.

3.3.2 Structure of CUDA Programming

The CUDA programming model developed by NVIDIA has been used to develop the code suitable for parallel computation on GPU architecture [Guide, 2013; Cheng *et al.*, 2014]. The CUDA programming model represents CPU architecture as a host unit and GPU architecture as a device unit. CUDA programming model uses the kernel function for the execution of the program. The

Table 3.1 : NVIDIA Tesla GP100 specifications

GPU Architecture	NVIDIA Pascal
NVIDIA CUDA Cores	3840
Memory Size	16 GB
Memory Bandwidth	732 GB/s
Double-Precision Performance	4.7 TeraFLOPS
Single-Precision Performance	9.3 TeraFLOPS
Half-Precision Performance	18.7 TeraFLOPS

kernel function in the CUDA programming model is a call function. It is called from the host (i.e., CPU) and runs on the device (i.e., GPU), as shown in Figure 3.9. It executes the complete domain grid in the GPU, which has been divided into a large number of GPU blocks. Each GPU block consists of a large number of threads for parallel computation.

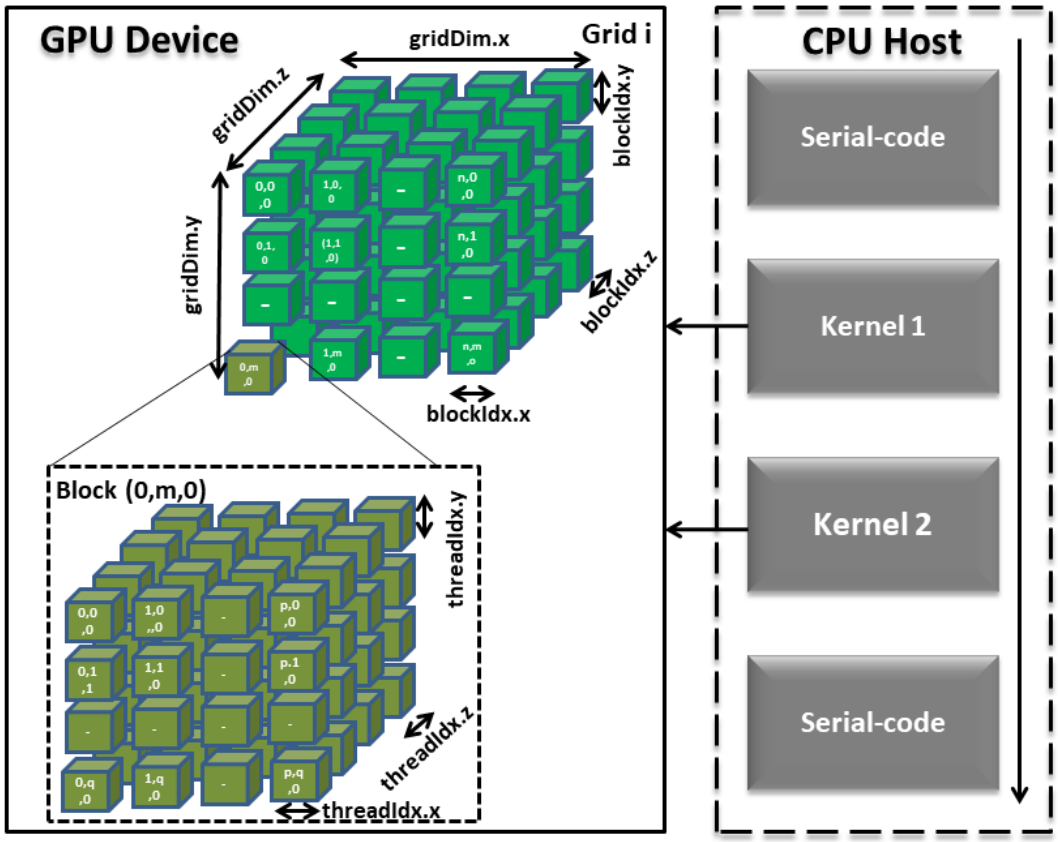

Figure 3.9 : Illustration of CUDA programming model in 3D.

Moreover, as illustrated in Figure 3.9, the meaning of the following terminologies are:

- *gridDim.x*, *gridDim.y*, and *gridDim.z* are the in-built commands used to define the number of blocks in the directions *x*, *y*, and *z*, respectively.

- *blockDim.x*, *blockDim.y*, and *blockDim.z* are the in-built commands used to provide block dimension, which means the number of threads each block contains in the direction *x*, *y*, and *z*, respectively.

- *blockIdx.x*, *blockIdx.y*, and *blockIdx.z* are the in-built commands that represents the block index (ID) in the *x*, *y*, and *z* direction, respectively.

- *threadIdx.x*, *threadIdx.y*, and *threadIdx.z* are the in-built commands for defining threads ID in each block in the *x*, *y*, and *z* direction, respectively.

The global thread ID in the particular direction can be calculated as:

- $i = blockIdx.x * blockDim.x + threadIdx.x;$

- $j = blockIdx.y * blockDim.y + threadIdx.y;$

- $k = blockIdx.z * blockDim.z + threadIdx.z;$

Furthermore, the block in the CUDA programming model runs parallel in different SMs, and the threads in each block run directly into CUDA cores. The important thing to understand is that the threads in each block can communicate with each other. However, threads in a different block cannot communicate. The more details can be found in Guide [2013].

3.3.3 LBM implementation on GPU cluster

The step by step procedure for the implementation of LBM algorithm on GPU architecture is given below:

- **step 1:** Allocate memory for the variables both on the host and device.

- **step 2:** Copy related variables from the host to device.

- **step 3:** Divide the domain into a combination of blocks and threads.

- **step 4:** Call the kernel function to perform different LBM operation, i.e, collision, streaming, boundary condition and updation of macroscopic variables.

- **step 5:** After completion of the simulation, transfer desired output files from device to host.

3.4 SUMMARY

In summary, this chapter conclude with the detailed description of the governing mathematical formulations of the popular SRT-LBM model for the different versions of 3D lattice structures. It has been described that the SRT-LBM model includes steps of collision and streaming in its expression. The LES turbulence model in the frame of LBM is described in detail, explaining the filtered equation of SRT-LBM to model the turbulent flow, along with the Smagorinsky SGS model to resolve the small-scale turbulent structures. The chapter provides the complete derivation of the incorporation of LES turbulence model in the LBE. The chapter also includes the description of the different types of boundary conditions in LBM, such as on-site velocity boundary condition, bounce-back method, and immersed boundary method. Lastly, the chapter illustrates the implementation of the LBM algorithm on the GPU platform.

...

4
Turbulent Flow Simulation over a Bluff Body

In this chapter, a set of numerical simulations using LBM are presented to test and compare the of different velocity distribution models of LBM and boundary conditions on the turbulent flow pattern. Hence, two studies have been performed on the benchmark case of turbulent flow past over a bluff body. First, how the different discrete velocity models of LBM affect the turbulent flow behavior past over a bluff body is explored. Second, the changes observed on the flow pattern on implementing different boundary conditions on the bluff body to achieve a no-slip condition are demonstrated.

The present work aims to address the aforementioned problems. A detailed discussion on the simulation methodology is presented in the next section. Our key contributions for this chapter are:

- Investigation of the efficiency of various 3-D discrete velocity models of LBM for the simulation of turbulent flow past over a bluff body.
- Comparison of two different boundary conditions for benchmark problem of turbulent flow simulation past a square cylinder.
- Implementation of the LBM algorithm on the GPU parallel environment using CUDA programming model.

In this chapter, the first problem is addressed by assessing the comparison of the discrete velocity models (D_3Q_{15}, D_3Q_{19}, and D_3Q_{27}) of the LBM for the simulation of turbulent flow over a bluff body. The second study reports the comparison of the modified bounce-back (BB) method and immersed boundary (IB) method for the treatment of no-slip boundary conditions for the same benchmark case of turbulent flow simulation over a bluff body.

The remainder of the chapter is organized as follows: Section 4.1 provides a comprehensive overview of the simulation geometry and the flow conditions used in the present thesis work. The numerical results are presented in Section 4.2. Section 4.3 summarizes and highlighting the key points of the chapter.

4.1 SIMULATION DOMAIN AND FLOW CONDITIONS

In this section, the geometry of the simulation domain and other flow conditions to study the turbulent flow over a bluff body using LBM are illustrated. Figure 4.1 shows the schematic representation of the flow domain. It consists of a square cylinder (diameter, d = 10 mm) confined in a rectangular duct. The cylinder has complete spans in the duct. The flow is described in the Cartesian coordinate system, where the x-axis is the streamwise dimension, the y-axis is the cross-stream dimension, and the z-axis is the spanwise dimension. In this work, the streamwise, cross-stream, and spanwise dimensions are $20d$, $5d$, and $3d$, respectively. The inflow condition has a mean velocity of U_m, with a thin boundary layer (6% of channel height, H). Random fluctuations are added to the mean velocity for inflow turbulence seeding. The random fluctuations are 6%

of U_m in RMS magnitude. The Reynolds number, defined as $Re_d = U_m d/\nu$ (where ν is the physical kinematic viscosity of the working fluid (i.e. water), is 3000 and the blockage ratio d/H is 20%. The cylinder is placed at the center of the duct and a distance of $0.6H$ from the inlet. A similar flow configuration experimentally studied by Nakagawa *et al.* [1999] for the channel flow. Later, Kim *et al.* [2004] numerically studied the particular flow configuration using a finite volume approach based on LES.

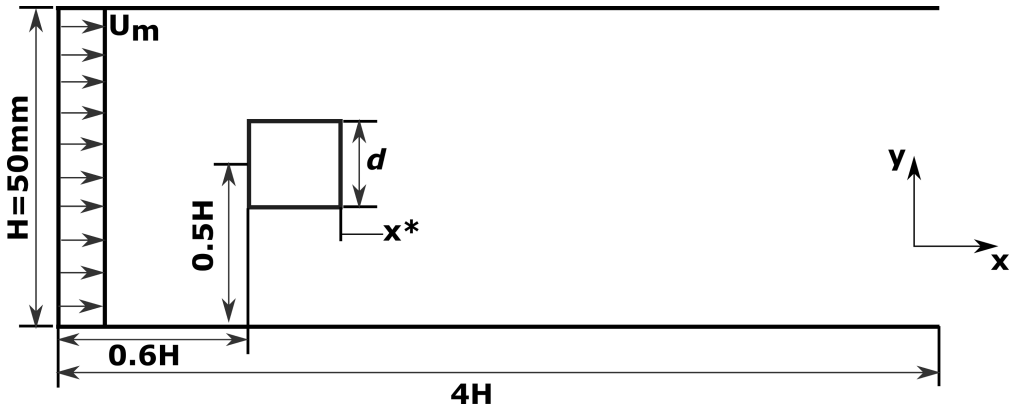

Figure 4.1 : Schematic representation of the flow domain.

In this study, the LES method is used to model the turbulent flow. The Smagorinsky SGS scheme has been used for subgrid-closure with a Smagorinsky constant (C_s) of 0.2 [Koda and Lien, 2015]. The uniform computational grid has $800\times200\times120$ nodes in the streamwise, cross-stream, and spanwise direction, respectively [Koda and Lien, 2015]. Simulations have run for a total of 1 million time-steps, and the turbulent statistics have averaged after every 1000 time-steps. The no-slip boundary conditions have been implemented on the walls of the rectangular duct and cylinder walls using a full way bounce-back rule [Agarwal and Prakash, 2018]. For the inlet, "on-site" velocity boundary conditions have been used, and at the outlet, constant pressure is applied [Agarwal, 2020; Hecht and Harting, 2010; Zou and He, 1997]. A detailed explanation for the boundary conditions is presented in Section 3.2.

4.2 RESULTS AND DISCUSSION

4.2.1 Effect of Discrete Velocity Models of LBM

In this subsection, the results of the effect of 3-D discrete velocity models of LBM (D_3Q_{15}, D_3Q_{19}, and D_3Q_{27}) on the turbulent flow over a bluff body are discussed. The details about the models are presented in Section 3.1. Figure 4.2 shows the instantaneous streamwise velocity component at a spanwise cross-section for all the discrete velocity models used in this study. The formation of vortices at the downstream face of the cylinder and the location of turbulent wakes can be visualized. The visualization plot shows that the diffusion of eddies reduces the turbulent intensity of wakes away from the downstream face of the cylinder. Here as we move away from the downstream face of the cylinder, small-scale eddies inside the turbulent wake start to diffuse in large-scale eddies and results in the growth of larger lumps of wakes with less intensity.

Figure 4.3 presents the profile of time-and spanwise-averaged streamwise velocity along the centerline (z=0) from the downstream face of the cylinder for the D_3Q_{15}, D_3Q_{19}, and D_3Q_{27} discrete velocity models of LBM (represented by red, green and blue markers respectively). The notation $< \cdot >$ denotes time-and spanwise-averaging. The obtained results are compared with the experimental results conducted by Nakagawa *et al.* [1999] and FVM-based numerical simulation

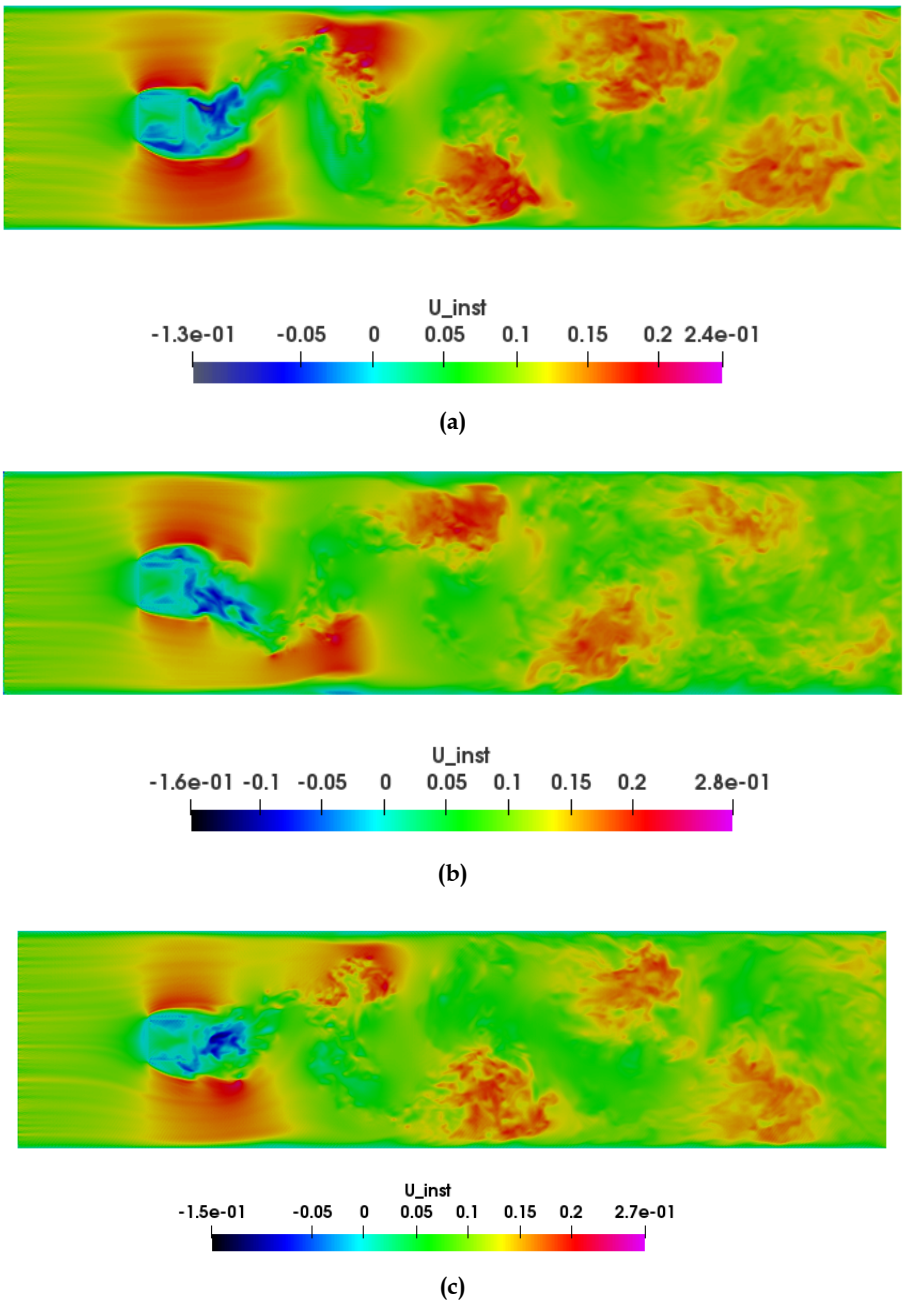

Figure 4.2 : Flow behavior of instantaneous streamwise velocity for (a) D_3Q_{15}, (b) D_3Q_{19}, and (c) D_3Q_{27} velocity models.

results of Kim *et al.* [2004]. All numerical procedures shown in this study are showing a similar pattern except for minor differences in the numerical value. The results show the asymptotic behavior for all studies on all downstream locations beyond $x^*/d \approx 2.4$ (where x^* is the streamwise distance from the downstream face of the cylinder) because no vortices have been identified. In contrast, some deviations have been observed before this downstream location, which is more prevalent up to $x^*/d \approx 0.8$ due to the presence of strong vortices in this region, as shown in Figure 4.2. The deviation in the present study and experiment has been expected because of the boundary condition assumption applied in other studies. The present study assumes the finite depth of the duct, whereas, in other studies, it is assumed to be an infinite channel that affects the velocity

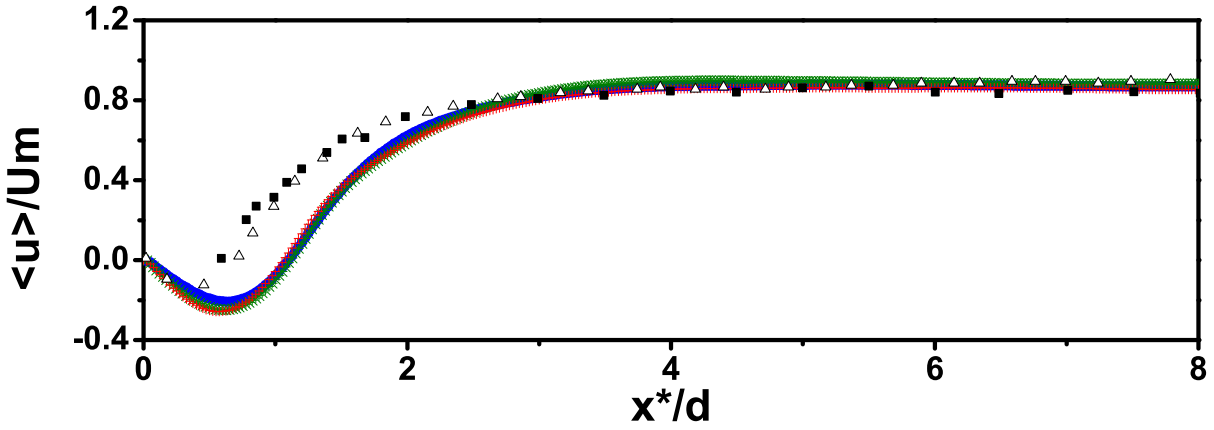

Figure 4.3 : Centerline distribution of mean streamwise velocity (red plus : D_3Q_{15}, green asterisk : D_3Q_{19}, blue open circle : D_3Q_{27}, open triangle : Kim *et al.* [2004], filled square: Nakagawa *et al.* [1999]).

profile and intensity of the vortices. Finite duct assumption would lead to a lower velocity at the spanwise faces of the duct with a no-slip boundary condition leading to a higher velocity at the center location for fixed Re_d = 3000. Moreover, finer grid resolution near the downstream face of the cylinder may result in more accurate agreement with data available in the literature [Nakagawa *et al.*, 1999; Kim *et al.*, 2004]. While comparing present results with them, we found that near the downstream face of the cylinder the agreement between LBM results and experimental data is significantly large. This may be due to the impact of cylinder edge on the flow field, resulting in an increase in velocity just before upstream in the experimental observations. This phenomenon is ignored in the present simulation, and it has been assumed to have a smooth transition from inlet to upstream face and up to past the cylinder [Agarwal, 2020].

Figure 4.4 presents the profiles of mean streamwise velocity at the different streamwise locations. The results are drawn for half of the y-axis (i.e., from $y = 0$ to $y = H/2$) due to symmetry in the y-axis. In Figure 4.4(a), the results show the lower velocity close to $y = 0$ for the present study. This is due to the high-intensity vortices, which can be seen at that location, as evident in Figure 4.2. Furthermore, its negative velocity leads to a decrease in the calculation of mean streamwise

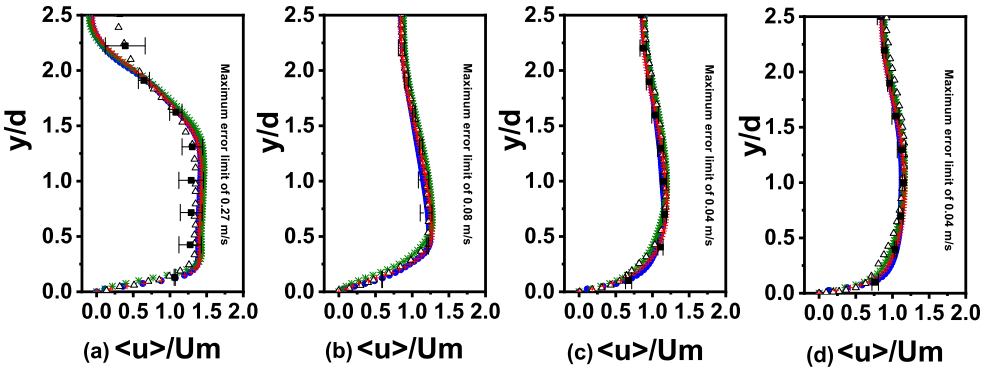

Figure 4.4 : Profiles of mean streamwise velocity (red plus : D_3Q_{15}, green asterisk : D_3Q_{19}, blue open circle : D_3Q_{27}, open triangle : Kim *et al.* [2004], filled square: Nakagawa *et al.* [1999]) : (a) x^*/d = 1.0, (b) x^*/d = 3.5, (c) x^*/d = 6.0, (d) x^*/d = 8.5.

velocity. However, the momentum far away from the location ($y = 0$) for fixed Reynolds number, *Re*, increased to counter the momentum at a location near to ($y = 0$), which gives rise to the intense vortices just behind the downstream face of the cylinder. Moreover, the lower mean streamwise velocity has been observed near the center ($y = H/2$) to counter the intense vortices again. The results for other figures away from the downstream face of the cylinder, the effect of the vortices diminishes, and all studies give the same results as expected.

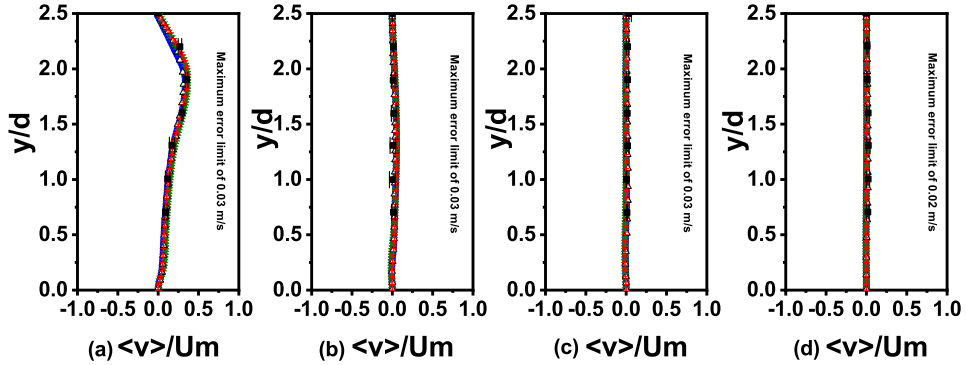

Figure 4.5 : Profiles of mean normal velocity (red plus : D_3Q_{15}, green asterisk : D_3Q_{19}, blue open circle : D_3Q_{27}, open triangle : Kim *et al.* [2004], filled square: Nakagawa *et al.* [1999]) : (a) x^*/d = 1.0, (b) x^*/d = 3.5, (c) x^*/d = 6.0, (d) x^*/d = 8.5.

Figure 4.5 shows the profile of mean normal velocity. The results show that far from downstream cylinder face, small scale eddies are diffused into large scale eddies, it becomes easy for any numerical schemes to capture moment accurately, as evident in Figure 4.5(d). The moment in the perpendicular direction to the flow should follow the net-zero moment transfer for which all studies agree far away from the cylinder, but just after the downstream face of the cylinder, the deviation on moment transfer is plotted in Figure 4.5(a). And, it has been found that the D_3Q_{27} velocity model gives slightly better results in the high turbulent region just after the downstream face of the cylinder.

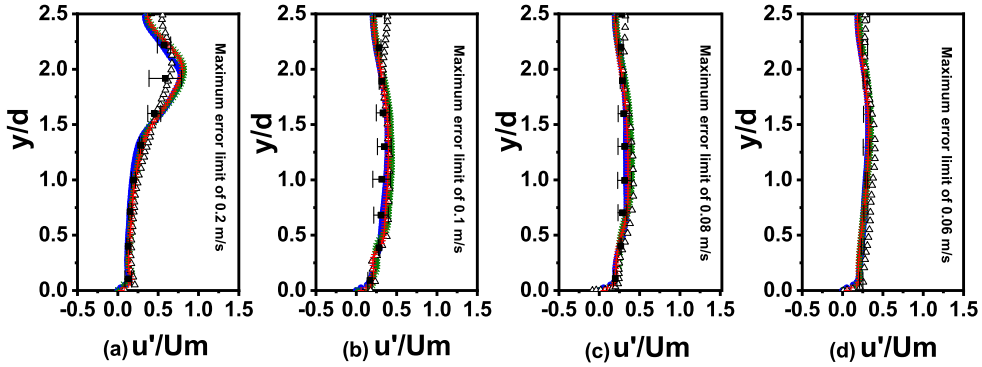

Figure 4.6 : Profiles of RMS streamwise velocity fluctuations (red plus : D_3Q_{15}, green asterisk : D_3Q_{19}, blue open circle : D_3Q_{27}, open triangle : Kim *et al.* [2004], filled square: Nakagawa *et al.* [1999]) : (a) x^*/d = 1.0, (b) x^*/d = 3.5, (c) x^*/d = 6.0, (d) x^*/d = 8.5.

Similar observations have been made for RMS streamwise velocity fluctuations and normal velocity fluctuations, as shown in Figures 4.6 and 4.7. D_3Q_{27}, velocity model, shows the less

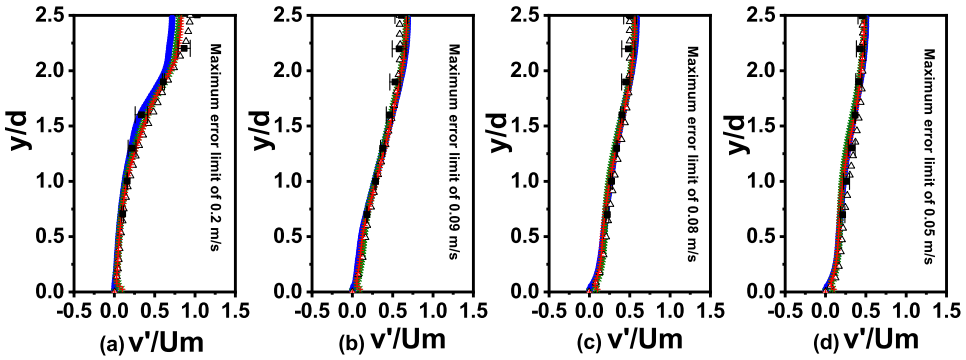

Figure 4.7 : Profiles of RMS normal velocity fluctuations (red plus : D_3Q_{15}, green asterisk : D_3Q_{19}, blue open circle : D_3Q_{27}, open triangle : Kim *et al.* [2004], filled square: Nakagawa *et al.* [1999]) : (a) x^*/d = 1.0, (b) x^*/d = 3.5, (c) x^*/d = 6.0, (d) x^*/d = 8.5..

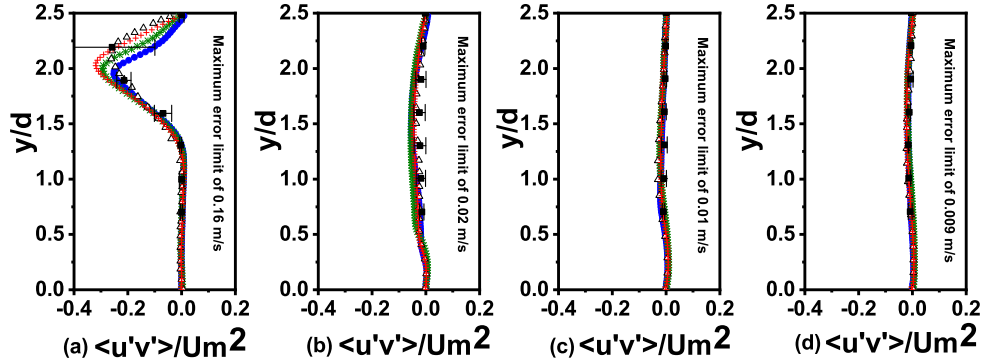

Figure 4.8 : Profiles of Reynolds shear stress (red plus : D_3Q_{15}, green asterisk : D_3Q_{19}, blue open circle : D_3Q_{27}, open triangle : Kim *et al.* [2004], filled square: Nakagawa *et al.* [1999]) : (a) x^*/d = 1.0, (b) x^*/d = 3.5, (c) x^*/d = 6.0, (d) x^*/d = 8.5.

randomness in velocity values for the perpendicular direction of flow near the downstream face of the cylinder compared to other discrete velocity models (i.e., D_3Q_{15} and D_3Q_{19}); however, the results predicted similar flow pattern away from the downstream face of the cylinder for all the discrete velocity models. Reynolds shear stress, which is responsible for drag force on a body, is plotted in Figure 4.8. All schemes predict similar observations far from the flow field with deviations among them near the downstream face of the cylinder. Stress has expected to be highest at the lower edge of the cylinder for an inviscid flow, which is perfectly captured by the present study for the D_3Q_{27} velocity model. Also, it is already mentioned above that the high-intensity vortices have been observed at the center location near the downstream face of the cylinder resulting in the high gradient in velocity vector, which further gives a considerable large shear stress value at that location. Earlier studies by Nakagawa *et al.* [1999] and Kim *et al.* [2004] show a lag in capturing the stress, but overall stress distribution is consistent with the D_3Q_{27} scheme, whereas other velocity models in the present study give over prediction of shear stress distribution. The more isotropic nature of the D_3Q_{27} scheme leads to the stress distribution similar to earlier studies.

Results for drag coefficient derived from shear stress are tabulated in Table 4.1. Results show good agreement between the present study for D_3Q_{27} velocity model and studies performed by Kim *et al.* [2004] for the calculation of drag force in the presence of turbulent flow past a bluff body (here referred to as a square cylinder).

Table 4.1 : Comparison of drag coefficient

Boundary Conditions	Grid Dimension	$\bar{C}_D$
D_3Q_{15}	800×200×120	2.4893
D_3Q_{19}	800×200×120	2.5216
D_3Q_{27}	800×200×120	2.7508
Kim *et al.* [2004]	-	2.76

The present study shows that the LBM method can be implemented fairly to predict turbulent flow in a closed system of fluid flow for a bluff body as an obstruction. LBM is quite able to capture small-scale flow phenomena and large-scale eddies in a turbulent flow. The method can adequately identify the region of vortices and turbulent wake with its intensity. Since the LBM scheme can be effectively implemented for a highly parallelized computing environment due to its local collision operations, the code used in this study has been evaluated for its performance on GPU accelerated parallel environment for all the discrete velocity models and results are presented in Table 4.2. The computational time taken by all the discrete velocity models (D_3Q_{15}, D_3Q_{19}, D_3Q_{27}) concerning the number of threads per block on the GPU cluster has been presented. As the maximum number of threads per block for NVIDIA Tesla P100 is 1024, simulations were performed by varying the number of threads per block (i.e., 1, 8, 64, and 512). The results were collected after 1000 time steps. The MLUPS has been calculated for a varying number of threads per block to measure the performance for all the discrete velocity models. The MLUPS can be calculated with expression given as:

$$MLUPS = \frac{n_x \times n_y \times n_z \times no.\ of\ iterations}{10^6 \times t_r} \tag{4.1}$$

where, n_x, n_y and n_z are the domain sizes in x, y, and z-dimension and t_r is the simulation run time.

The results for the computational efficiency of the discrete velocity models can also be observed in Figure 4.9. As shown in Figure 4.9, the difference between MLUPS values for all the discrete velocity models with a single thread per block is less compared to multiple threads in a block. The result shows that with an increasing number of threads per block, the difference between the MLUPS value among the discrete velocity models increases. Also, one can easily visualize from the plot that increasing the number of velocities deteriorates the computational performance as expected.

4.2.2 Effect of Boundary Conditions

Here, the effect of the modified BB method and IB method for the treatments of the no-slip boundary condition is presented. A particular explicit diffuse direct-forcing immersed boundary-lattice Boltzmann method (IB-LBM) is adopted for the present work. The details and formulation for the BB and IB method are presented in Section 3.2. In this work, the cheap-clipped fourth-order polynomial function proposed by Deen *et al.* [2004] as discussed in Section 3.2.2 is used to mapped unforced velocities at the Eulerian grid nodes on boundary nodes and for distribution of boundary forces on the Eulerian nodes.

Table 4.2 : Computational efficiency of discrete velocity models on GPU cluster

Velocity Model	Threads per block	Computation time (s)	MLUPS
D_3Q_{15}	1	964	19.92
	8	212	90.57
	64	145	132.41
	512	102	188.23
D_3Q_{19}	1	1025	18.73
	8	244	78.69
	64	184	104.35
	512	138	139.13
D_3Q_{27}	1	1452	13.22
	8	320	60.00
	64	262	73.28
	512	178	107.86

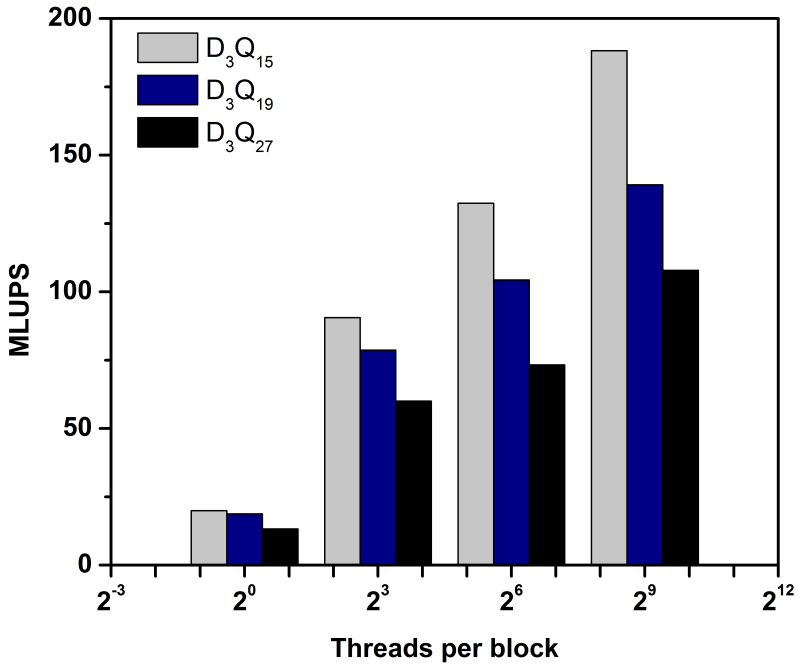

Figure 4.9 : GPU performance of discrete velocity.

Figure 4.10 presents the profile of streamwise velocity along the centerline (z = 0) from the downstream face of the cylinder. The results obtained from BB and IB are in fair agreement with the experimental measurement of Nakagawa *et al.* [1999], and LES results of Kim *et al.* [2004]. However, it can be seen that near the downstream face of the cylinder, results show a slight divergence from the experimental and numerical results [Nakagawa *et al.*, 1999; Kim *et al.*, 2004].

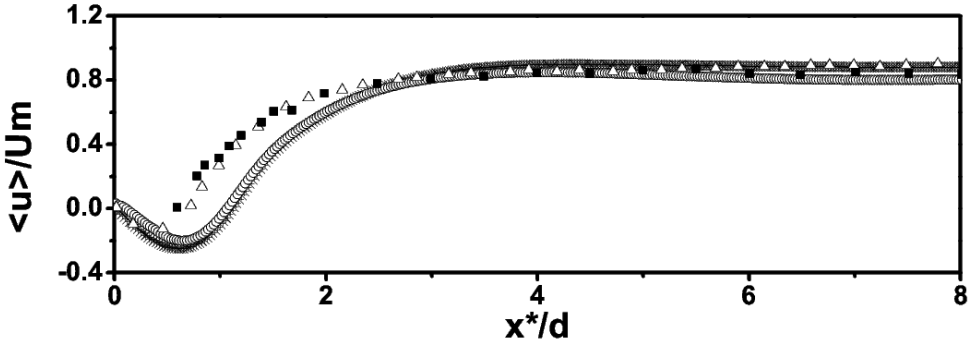

Figure 4.10 : Centerline distribution of mean streamwise velocity (asterisk : BB, open circle : IB, open triangle : Kim *et al.* [2004], filled square : Nakagawa *et al.* [1999]).

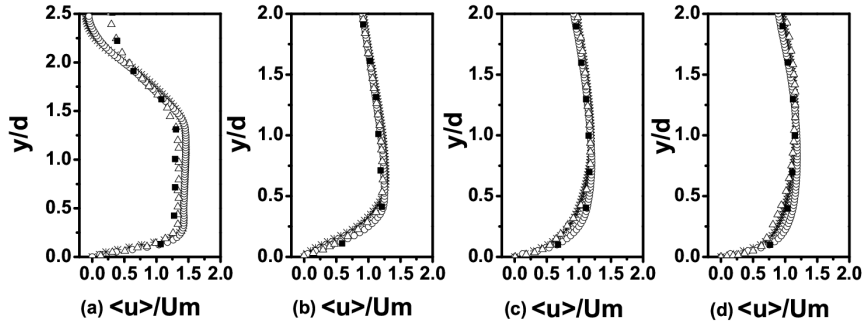

Figure 4.11 : Profiles of mean streamwise velocity (asterisk : BB, open circle : IB, open triangle : Kim *et al.* [2004], filled square : Nakagawa *et al.* [1999]) : (a) x^*/d = 1.0, (b) x^*/d = 3.5, (c) x^*/d = 6.0, (d) x^*/d = 8.5.

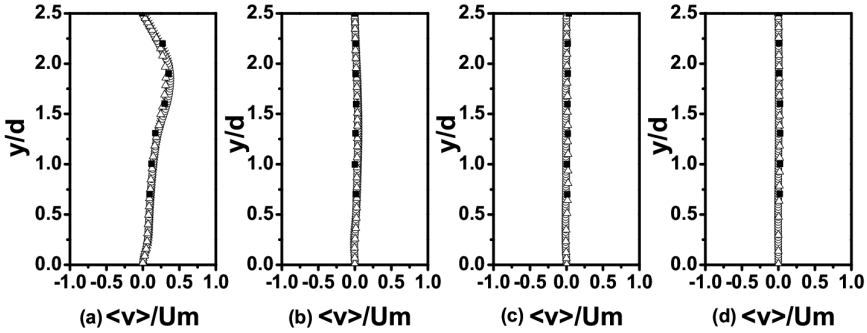

Figure 4.12 : Profiles of mean normal velocity (asterisk : BB, open circle : IB, open triangle : Kim *et al.* [2004], filled square : Nakagawa *et al.* [1999]) : (a) x^*/d = 1.0, (b) x^*/d = 3.5, (c) x^*/d = 6.0, (d) x^*/d = 8.5.

Profiles of time-and spanwise-averaged mean velocities, turbulent fluctuations, and Reynolds shear stress are shown in Figures 4.11-4.15, respectively, for different streamwise location (x*/d = 1.0, 3.5. 6.0, 8.5). In Figure 4.11(a), a similar deviation has been observed in the mean streamwise velocity near the downstream face of the cylinder for both BB and IB methods. The

other figures show excellent agreement with the literature [Nakagawa *et al.*, 1999; Kim *et al.*, 2004] away from the cylinder face. The results for mean normal velocity shown in Figure 4.11 presents a good match for both BB and IB methods with experimental measurements and LES results. Moreover, it can be seen from Figures 4.11 and 4.12 for both BB and IB methods that the mean streamwise velocity is much affected by the pair of vortices formed behind the cylinder compared to mean normal velocity.

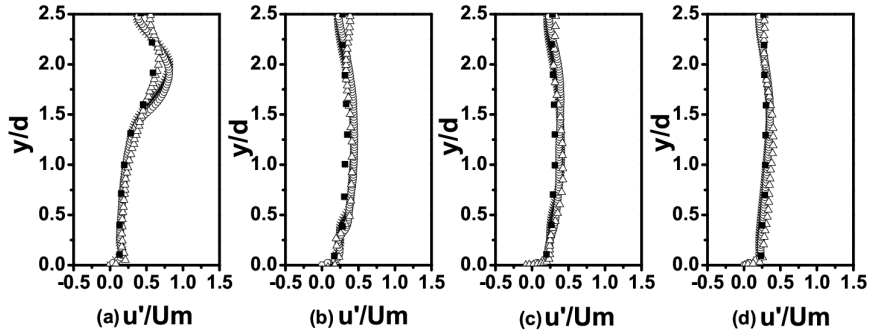

Figure 4.13 : Profiles of RMS streamwise velocity fluctuations (asterisk : BB, open circle : IB, open triangle : Kim *et al.* [2004], filled square : Nakagawa *et al.* [1999]) : (a) x^*/d = 1.0, (b) x^*/d = 3.5, (c) x^*/d = 6.0, (d) x^*/d = 8.5.

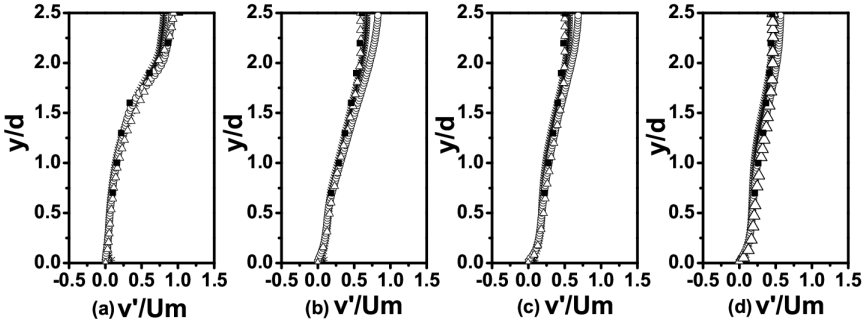

Figure 4.14 : Profiles of RMS normal velocity fluctuations (asterisk : BB, open circle : IB, open triangle : Kim *et al.* [2004], filled square : Nakagawa *et al.* [1999]) : (a) x^*/d = 1.0, (b) x^*/d = 3.5, (c) x^*/d = 6.0, (d) x^*/d = 8.5.

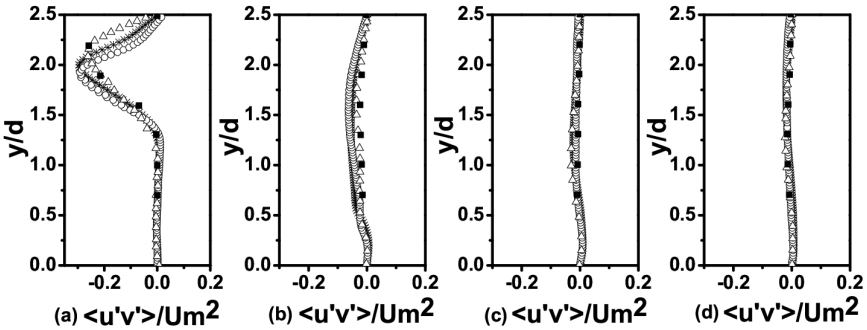

Figure 4.15 : Profiles of Reynolds shear stress (asterisk : BB, open circle : IB, open triangle : Kim *et al.* [2004], filled square : Nakagawa *et al.* [1999]) : (a) x^*/d = 1.0, (b) x^*/d = 3.5, (c) x^*/d = 6.0, (d) x^*/d = 8.5.

For the case of turbulent fluctuations, as shown in Figures 4.13 and 4.14, disagreement also

continues in the RMS streamwise velocity fluctuations near the downstream face of the cylinder are quickly recovered in the downstream direction away from the cylinder for both BB and IB method. Figure 4.15 shows profiles of Reynolds shear stress at a different streamwise location, and similar variation is observed with both BB and IB methods near the downstream face of cylinder compared to Nakagawa *et al.* [1999] and Kim *et al.* [2004] results. The results on other streamwise locations displayed excellent correspondence with literature data Nakagawa *et al.* [1999]; Kim *et al.* [2004].

The comparison of mean drag coefficient $\bar{C}_D$ is shown in Table 4.3. The table shows good agreement of the mean drag coefficient obtained from the BB method with the LES results of Kim *et al.* [2004]. However, a slightly higher value in the simulation of Kim *et al.* [2004] can be because of capturing the resistance of the flow field by the edge of the cylinder surface, which is absent in our study. The IB method over-predicted the mean drag coefficient. Further, the comparison of the BB and IB method based on computational efficiency is shown in Table 4.4. The computational time taken by both approaches concerning the number of threads per block on the GPU cluster is presented. The performance is measured from the MLUPS, and expression is given in Eqn. (4.1).

As seen in Table 4.4., the MLUPS numbers for the BB method are 65.01, 89.95, and 163.57, whereas

Table 4.3 : Comparison of drag coefficient

Boundary Conditions	**Grid Dimension**	$\bar{C}_D$
BB	800×200×120	2.52
IB	800×200×120	2.96
Kim *et al.* [2004]	-	2.76

Table 4.4 : Computational efficiency of BB and IB method on GPU cluster

Velocity Model	**Threads per block**	**Computation time** (s)	**MLUPS**
BB	8	295.34	65.01
	64	213.44	89.95
	512	117.37	163.57
IB	8	431.96	44.45
	64	327.79	58.57
	512	208.87	91.92

MLUPS numbers for the IB method are 44.45, 58.57, and 91.92 for 8, 64, and 512 threads per block, respectively. It shows that the computationally BB approach is faster than the IB method. It can also be observed from Table 4.4 that there is a difference of approx 32% in MLUPS of BB and IB method for 8 number of threads per block. This difference increases with the increasing number of threads per block (i.e., approx 34% for 64 number of threads per block and approx 44% for 512 number of threads per block). It summarizes that the difference in the computational performance of BB and IB on the GPU cluster is small for a lesser number of threads per block, while the increasing number of threads per block deteriorates the performance of the IB method compared to the BB method. For enhancing the computational performance of the IB method, the continuous transfer of variables from the host (i.e., CPU) to the device (i.e., GPU) and vice-versa must be avoided. This continuous transfer of data from the host to device and vice-versa is because the velocity components of surrounding fluid nodes across the boundary nodes are transferred from the device (i.e., GPU) to the host in order to calculate the forces at the boundary nodes on the host (i.e., CPU) architecture, and these forces then again transferred to the device for further simulation.

4.3 SUMMARY

In this chapter, the simulation of turbulent flow over a bluff body using LBM is presented. The chapter comprises the results of two studies. The first study reported the effect of 3D discrete velocity sets (i.e., D_3Q_{15}, D_3Q_{19}, and D_3Q_{27}) of LBM on the flow behavior of turbulent flow over a bluff body. However, the impact of the different boundary conditions (i.e., BB and IB) is explored in the second study. The simulations have been carried out for benchmark case of flow past a square cylinder confined in a rectangular duct at Re_d = 3000 for both the studies. LES approach has been used to simulate turbulent flow. The Smagorinsky SGS model is used to resolve the small-scale turbulent structures. The obtained simulation results for both studies are validated through the experimental and numerical results available in the literature. Moreover, a parallel computer code has been developed using CUDA programming model to run on a multicore GPU platform, and the computational performance has also been presented. For the first study, results are presented for the comparative assessment of 3D discrete velocity sets (i.e., D_3Q_{15}, D_3Q_{19}, and D_3Q_{27}) of LBM based on the accuracy and performance of the code in the GPU parallelized environment. The results obtained from LBM-LES are stable and in good agreement with the experimental data. Furthermore, results showed that the LBM method effectively captures the small-scale phenomenon and large-scale fluid properties. The obtained results depicted better accuracy for the D_3Q_{27} velocity model over other discrete velocity models at the cost of computation time. Parallelization of code reduces the computational cost drastically as more threads are available for computation. Computation time for the D_3Q_{27} velocity model has found almost 1.5 times the computation time of the D_3Q_{15} velocity model, and the ratio for computation times for both schemes widens more as the number of threads increases. The study suggests that the LBM can capture the turbulent flow even in the region of high Reynolds shear stress. The study provides insight for selecting the suitable LBM discrete velocity scheme based on the accuracy required and computational power needed, mainly for the simulation of benchmark problems of fluid flow such as flow past a single obstacle. In another study, the simulaions are performed to visualize the effect of boundary conditions on the flow behavior. The BB and IB method are taken into consideration for the simulation. The results obtained from both the boundary method are in nearly similar agreement with the experimental and numerical results obtained by other researchers in the past studies. However, from a computational perspective, the obtained results show that the bounce-back approach is computationally more efficient than the immersed boundary method. The above studies are intended to be expanded to simulate complex fluid dynamics problems on large domains, which will involve turbulent flow and fluid-structure interaction, and require high computational performance. The same are discussed in the subsequent chapter.

…

5

Effect of Baffles on the Flow Hydrodynamics of Dual-Rushton Turbine Stirred Tank Bioreactor

As presented in Chapter 4, the LBM can effectively predict turbulent flow passing through a stationary body in a closed system. The following work reports the extension of LBM application to model the turbulent flow in a complex geometry equipped with rotational objects. In this chapter, numerical simulations are performed to examine the effect of baffles on flow activity in a stirred tank bioreactor fitted with two six-blade Rushton turbines. The simulations are performed for three different geometries of stirred tank reactors, differentiated based on the impeller clearance. The study shows the impact of baffles on all the three employed geometries.

A detailed overview of the flow system is presented in the next section. Our major contributions for this chapter are:

- Investigate the influence of impeller clearance on the flow pattern in the stirred tank reactor equipped with dual-Rushton impellers.
- And, analyzing the impact of presence and absence of baffles on the flow behavior at different impeller clearance

The rest of the chapter is structured as follows: Section 5.1 details the information about the flow system used in the present work. An overview of the simulation methodology is presented in Section 5.2. Section 5.3 discusses the aspects of numerical setup. The numerical results are presented in Section 5.4. Section 5.5 summarizes the chapter.

5.1 FLOW SYSTEM

The simulation has been performed in a stirred tank reactor of standard configuration. It consists of a fully cylindrical tank of diameter, T with a flat base, open on top. The agitation in the reactor has provided with the two-Rushton impeller of diameter, D. The details of the tank geometry and the impeller are presented in Figure 5.1. The water has filled up to a height (H_w) equal to the tank diameter. The Reynolds number (Re), which fully determines the liquid flow behavior, is defined by $Re = \frac{ND^2}{\nu} \approx 40,000$, where N is the rotational speed of the impeller that is fixed at 250 (in rpm), and ν is the kinematic viscosity of the working fluid (i.e., water) [Derksen and Van den Akker, 1999]. The dimensional values are listed in Table 5.1 [Micale *et al.*, 1999]. A similar flow configuration was studied by Micale *et al.* [1999]. using the sliding-grid method with $k-\omega$ turbulence model to resolve the turbulent structures. Moreover, as the analysis explores the influence of baffles on the flow behavior, the simulation was conducted on the identical configuration of the stirred tank reactor, both in the presence and absence of baffles.

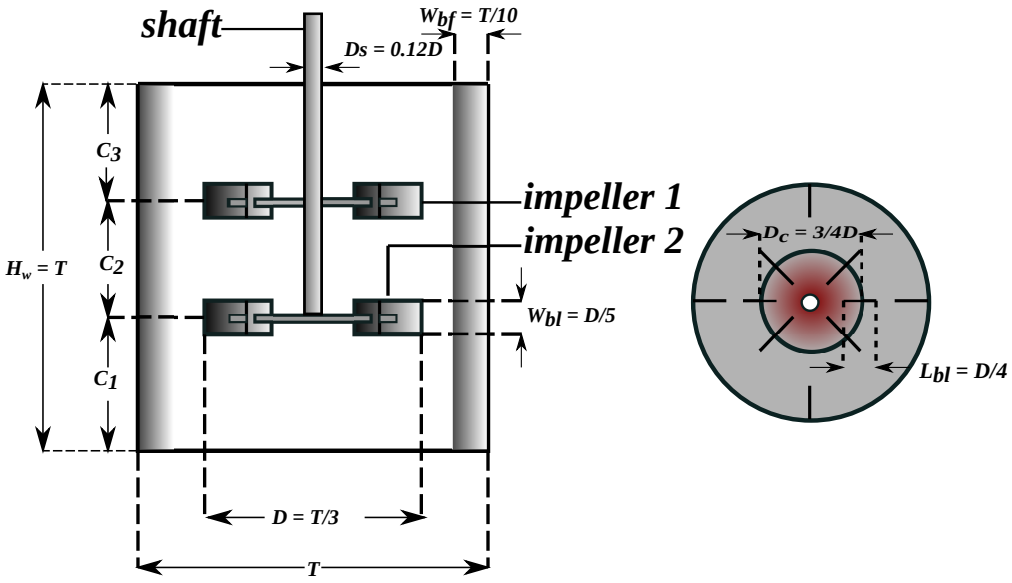

Figure 5.1 : Schematic representation of the flow domain

Table 5.1 : Reactor and impellers dimensions [Rutherford *et al.*, 1996]

	Case 1	Case 2	Case 3
Tank diameter, T (cm)	29.4	29.4	29.4
Water level, H_w (cm)	29.4	29.4	29.4
Water volume, V_w (l)	≈20	≈20	≈20
Baffle width , W_{bf} (cm)	2.94	2.94	2.94
Baffle length, L_{bf} (cm)	29.4	29.6	29.4
Number of baffles plate, N_{bf}	4	4	4
Impeller diameter, D (cm)	9.8	9.8	9.8
Shaft diameter, D_s (cm)	1.176	1.176	1.176
Number of blades, N_{bl}	6	6	6
Circular disk diameter, D_c, (cm)	7.35	7.35	7.35
Blade length, L_{bl} (cm)	2.45	2.45	2.45
Blade width, W_{bl} (cm)	1.96	1.96	1.96
Impeller clearance (cm)	C_1 = 0.25T	C_1 = 0.33T	C_1 = 0.15T
	C_2 = 0.50T	C_2 = 0.33T	C_2 = 0.50T
	C_3 = 0.25T	C_3 = 0.33T	C_3 = 0.35T

5.2 SIMULATION METHODOLOGY

In this work, LBM has been used to discretize the flow domain. The particular lattice Boltzmann (LB) scheme used in the present thesis work is SRT-LBM. The LES is used to model the turbulent flow and the Smagorinsky SGS model is employed to resolve the small-scale turbulent structures. The mathemtical formulation of the SRT-LBM method and the incorporation of LES model in LBM are detailed in Section 3.1.

5.3 ASPECTS OF NUMERICAL SETUP

A uniform, cubic computational grid of 150^3 has been defined for the simulation to discretize the fluid domain. The LES method is used in this analysis to model turbulent flow. For subgrid-closure, the SGS scheme was adopted with a Smagorinsky constant (C_s) of 0.1 [Smagorinsky, 1963]. The particular value of C_s = 0.1 is most commonly used for the shear-driven turbulence [Derksen, 2001]. The no-slip modified bounce-back boundary condition is imposed at the walls of the cube, whereas the free-slip boundary condition is defined at the top surface to represent the free surface, as discussed in Section 3.2. The cylindrical tank wall, the rectangular baffles, the revolving impellers, and the shaft are mounted inside the computational domain. The computational domain of these reactor components is represented as a set of points called control points. The distance between two control points at the reactor components is $0.6\Delta x$, where Δx is the grid spacing equal to $2.0 \times 10^{-3}\ m$. The total number of control points on the impeller surface was 9264, and the number of control points on the cylindrical tank wall was 116,250. The IB-LBM method presented in Section 3.2 is used to model the interaction between the reactor components and the fluid. For cylindrical tank walls and baffles, the boundary nodes have zero velocities. Moving parts are again treated as immersed boundaries but with non-zero velocities. The no-slip condition on the reactor components is maintained by using a two-way coupling approach. In this approach, the surrounding fluid velocity is interpolated onto the control points of the reactor components to measure the force applied by the fluid flow on the boundary surface, and then these forces are distributed back to the surrounding fluid nodes. Moreover, the interpolation between the surrounding fluid nodes and the control points of the reactor components is performed with the cheap-clipped fourth-order polynomial mapping function proposed by Deen *et al.* [2004] as described in Section 4.2. The computer code is developed to efficiently run on the GPU cluster for the execution of the simulations. The details of the implementation of code on the GPU parallel cluster are given in Section 3.3. The simulation starts with a stagnant liquid and proceeds with a time step of 100 μs. The simulation runs for 150,000-time steps, which represent 15s for the operation of the reactor in real-time [Agarwal *et al.*, 2021]. An interested reader, on the other hand, might refer to the major work of Bartels *et al.* [2002] to comprehend memory optimization in parallel-vector computers. The research article used two distinct ways of parallel-vector computing to run numerical simulations on stirred vessel flows at varying Reynolds numbers, one with shared memory and the other with distributed memory.

5.4 RESULTS AND DISCUSSION

The simulations findings demonstrate that the three distinct flow patterns observed rely on the location of impellers, as illustrated in Figure 5.2. Case 1 indicates a parallel flow pattern. Each of the impellers, i.e. upper and lower, generate two vortex rings in their vicinity. Hence, four vortex rings are formed in the parallel flow. The Case 2 shows a merging flow pattern. Here, the flow generated by the impellers merges at a halfway elevation between the upper and lower impeller with a formation of two large vortex rings. A diverging flow pattern is exhibited by Case 3 in which the lower impeller forces the flow stream towards the bottom of the tank. This is attributed to the low position of the impeller. As a result, a large vortex ring is formed near the lower impeller and two vortex rings are formed near the upper impeller.

5.4.1 Instantaneous Flow Field

Figure 5.3-5.5 show contour plots of instantaneous velocity magnitude at the upper impeller location for Case 1, Case 2, and Case 3 respectively, each containing baffles [Agarwal *et al.*, 2021] and without baffles case. For each case comprising baffles, the maximum velocity magnitude is observed near the impeller vicinity, which decreases with an increase in radial distance from the impeller.

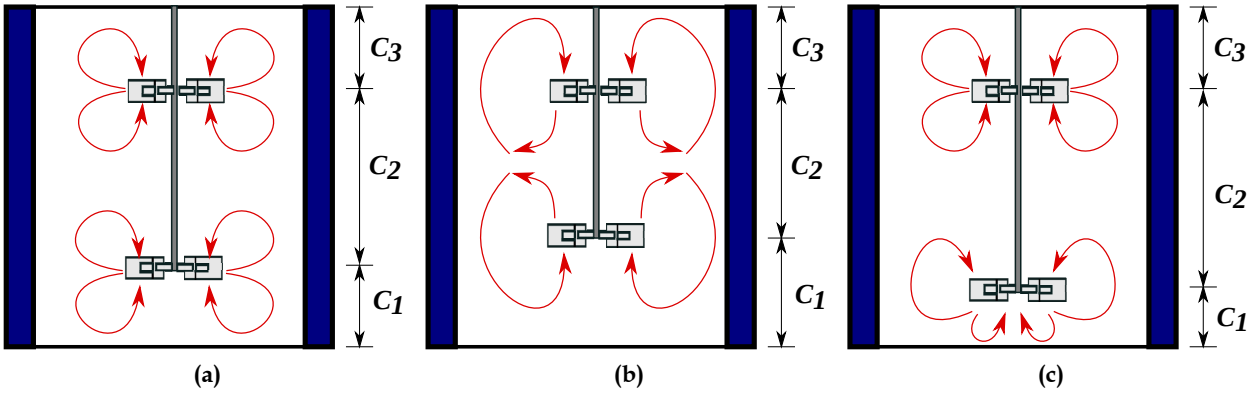

Figure 5.2 : Flow Patterns in the stirred tank reactor with dual-Rushton turbines a) Parallel flow, b) Merging flow, and c) Diverging flow for Case 1, Case 2, and Case 3 respectively in Table 5.1.

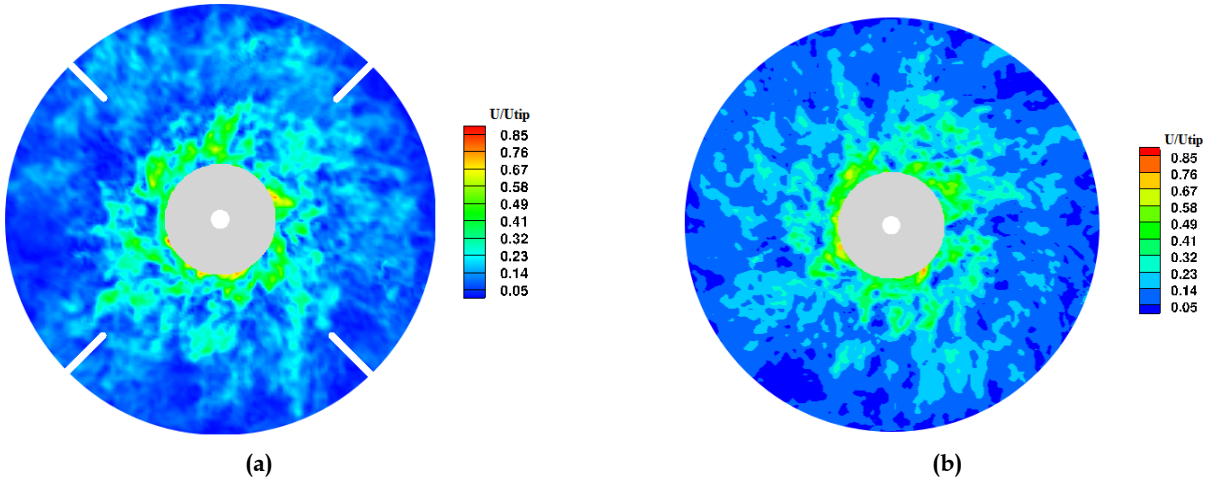

Figure 5.3 : Instantaneous velocity magnitude contour at upper impeller location for Case 1: (a) with baffles, (b) without baffles.

In Case 1, the velocity magnitude shows nearly a similar distribution, i.e., maximum velocity near impeller vicinity and stagnant zone domination near the reactor surface. However, in the Case 2 and Case 3, the situation differs.The velocity magnitude in the instances without baffles is significantly lower than in the baffled cases; this might be due to abrupt abnormalities forming at the tank's surface in the baffled cases. Furthermore, because of the no-slip boundary condition applied on the impeller surface, the greatest velocity magnitude is seen near the reactor surface, resulting in zero relative velocity between the impeller and the fluid particle at the impeller surface. As a result, as the impeller spins, the fluid around it rotates as well, resulting in a greater velocity magnitude closer to the reactor surface.

5.4.2 Phase-Averaged Flow Field

Figure 5.6 shows the contour plots of phase-averaged velocity magnitude at upper impeller location for Case 1, with baffles and without baffles. The phase-averaged velocity is a special

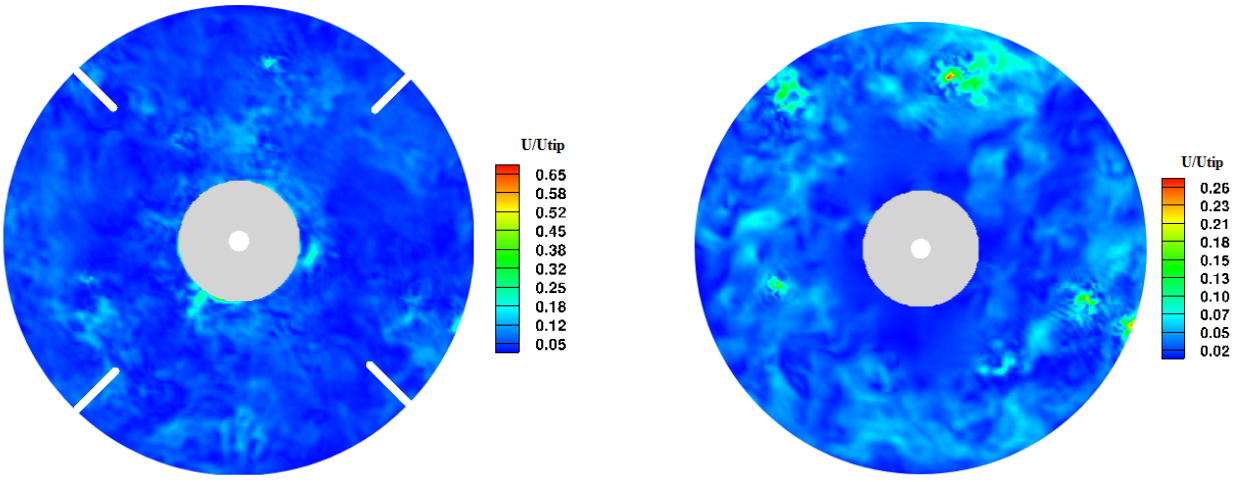

(a) (b)

Figure 5.4 : Instantaneous velocity magnitude contour at upper impeller location for Case 2: (a) with baffles, (b) without baffles.

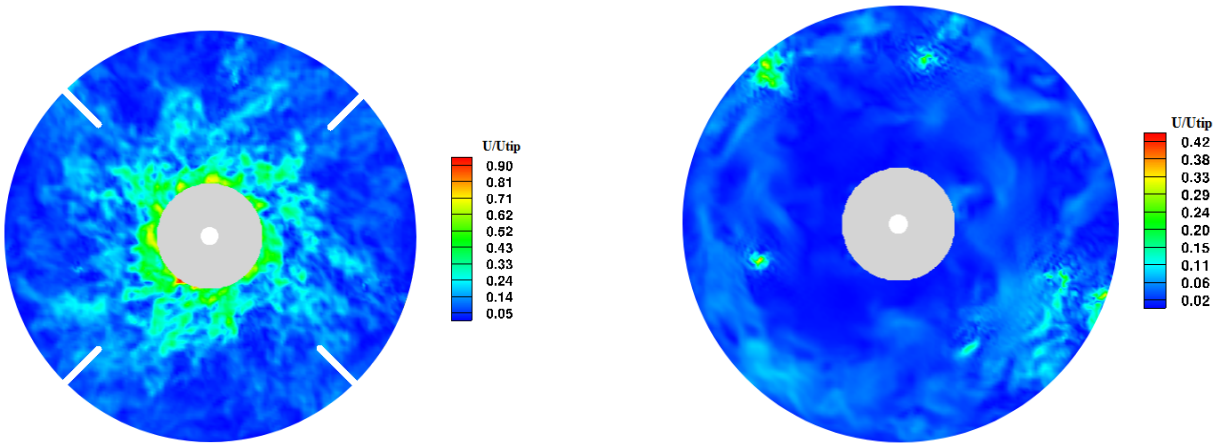

(a) (b)

Figure 5.5 : Instantaneous velocity magnitude contour at upper impeller location for Case 3: (a) with baffles, (b) without baffles.

case of ensemble averaging in which velocity is recorded at the same time during each impeller cycle and then averaged. The maximum phase-averaged velocity magnitude is observed near the impeller tip. Both the velocity contours seem to be identical in terms of velocity magnitude and its distribution. The maximum phase-averaged velocity magnitude is approximately 0.65 times than the linear velocity at the tip of the impeller blades U_{tip} for both the cases, i.e., with and without baffles. The linear tip velocity of the blades is equal to the rotational speed of the impeller (i.e., 250 rpm or 1.28 m/s). Moreover, the present study depicts that the tip velocity of the blades can only be used to make a qualitative estimate of the maximum fluid flow velocity magnitude.

Figures 5.7 and 5.8 show the contour plots of phase-averaged velocity magnitude at upper

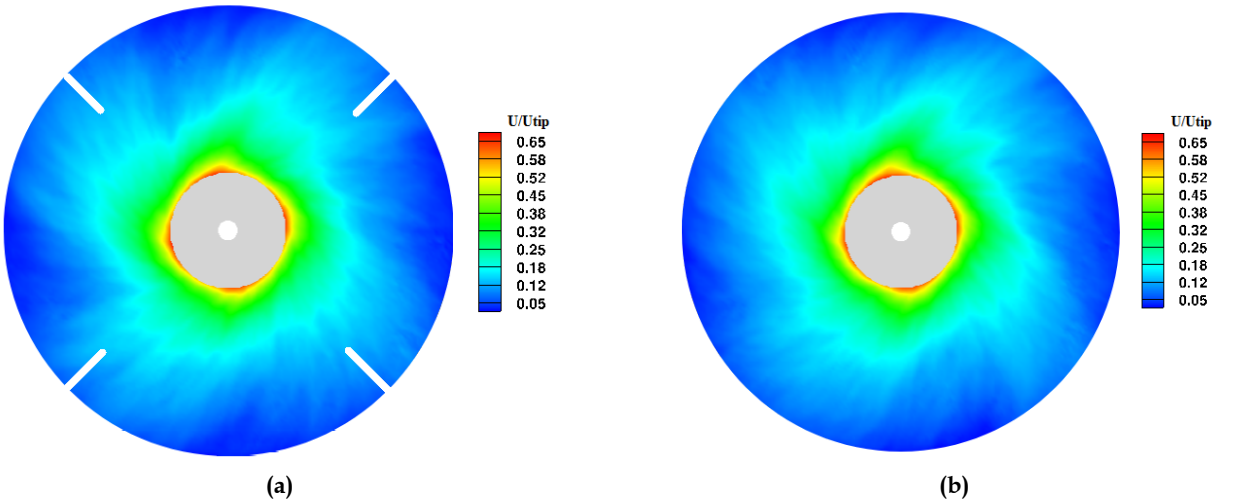

(a) (b)

Figure 5.6 : Phase-averaged velocity magnitude contour at upper impeller location for Case 1: (a) with baffles, (b) without baffles.

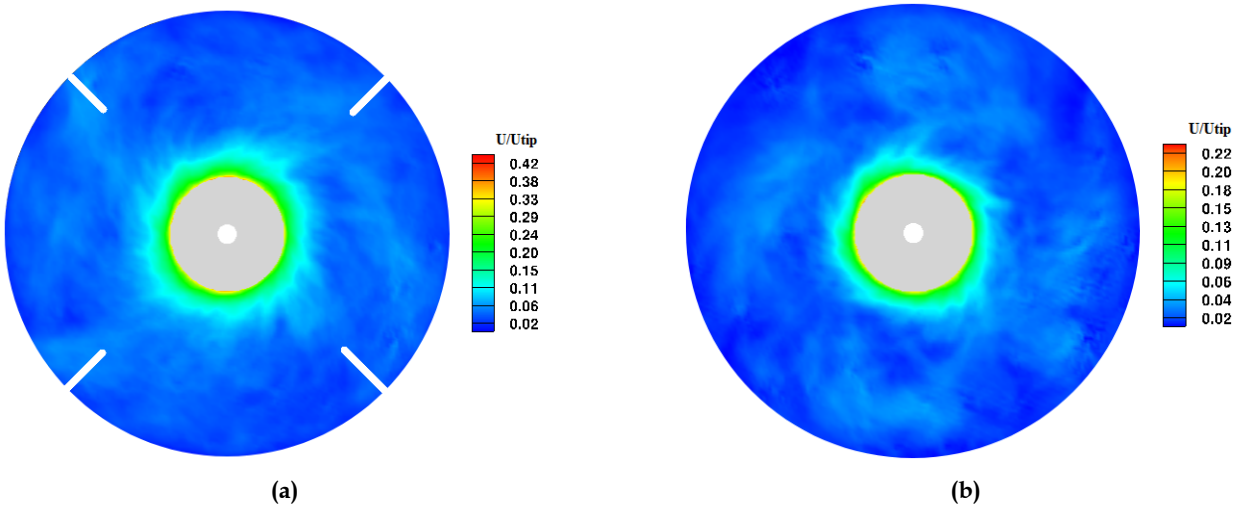

(a) (b)

Figure 5.7 : Phase-averaged velocity magnitude contour at upper impeller location for Case 2: (a) with baffles, (b) without baffles.

impeller location for Case 2 and Case 3 respectively, with baffles [Agarwal *et al.*, 2021] and without baffles. The velocity magnitude at the upper impeller is reduced as compared to the parallel flow. In Figure 5.7, the without baffles case is also showing the same behavior but with a smaller velocity magnitude. The average velocity magnitude is maximum at the impeller vicinity, which reduces towards the reactor surface. The case with baffles shows a higher velocity magnitude with a reduced stagnant zone. In Figure 5.8, the stagnant region is less than that of the above two cases for the without baffles case. As discussed above, the parallel, merging, and diverging flows depend on the distance between the upper and lower impeller blades and the distance between the lower impeller blades from the bottom of the tank. Moreover, as far as the stagnant region area is concerned, it could be due to the strong swirling flow characteristics of Case 3 as compared to

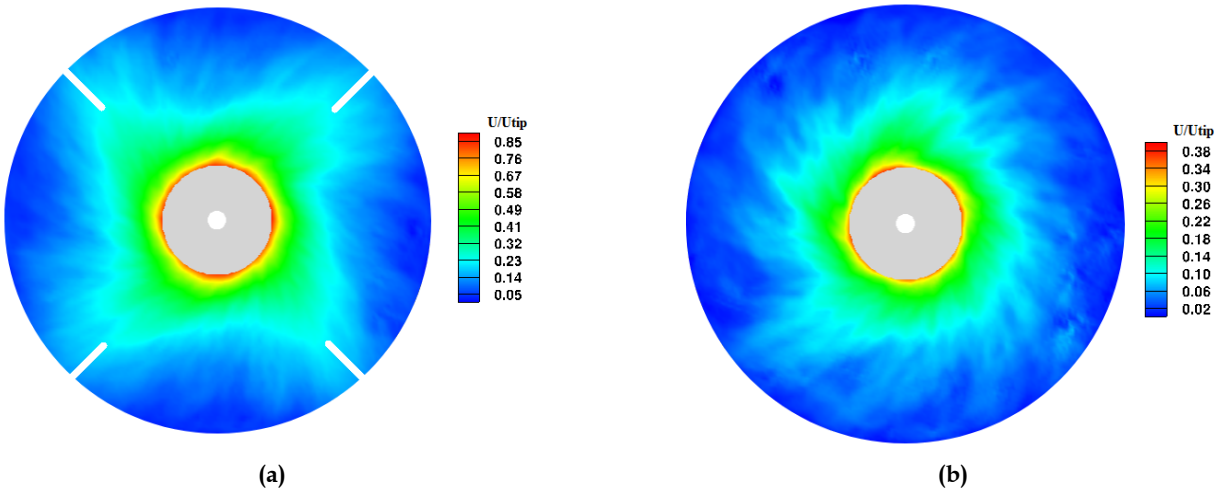

(a) (b)

Figure 5.8 : Phase-averaged velocity magnitude contour at upper impeller location for Case 3: (a) with baffles, (b) without baffles.

Case 1 and Case 2 [Li *et al.*, 2012].

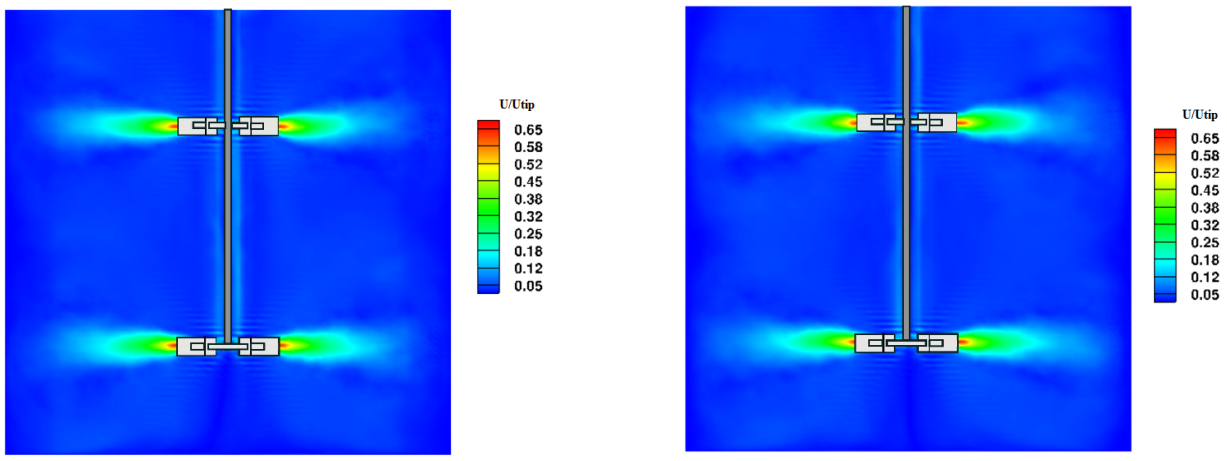

(a) (b)

Figure 5.9 : Phase-averaged velocity magnitude contour at $\theta = 0^\circ$ for Case 1: (a) with baffles, (b) without baffles.

Figure 5.9 shows the contour plots of phase-averaged velocity magnitude at θ=0° for Case 1. The maximum velocity magnitude is near the vicinity of both the upper and lower impellers. In both the cases i.e. with and without baffles, the velocity magnitudes are showing the same spread. Most of the contour plot is showing dominance of dead zone or stagnation zone. The stagnant zone is undesirable as the energy dissipation takes place in a smaller volume. In both cases, i.e., with and without baffles, the velocity contours are nearly identical. Nonetheless, the primary purpose of using baffles in the reactor is to avoid the swirl motion of the fluid in agitation. The baffles in the reactor convert the swirl motion of the fluid in the desired flow pattern. It converts the rotational flow of fluid to an axial flow, resulting in proper mixing. However, for the parallel flow bioreactor, the flow pattern for both with and without baffles' cases is similar. Hence bioreactors

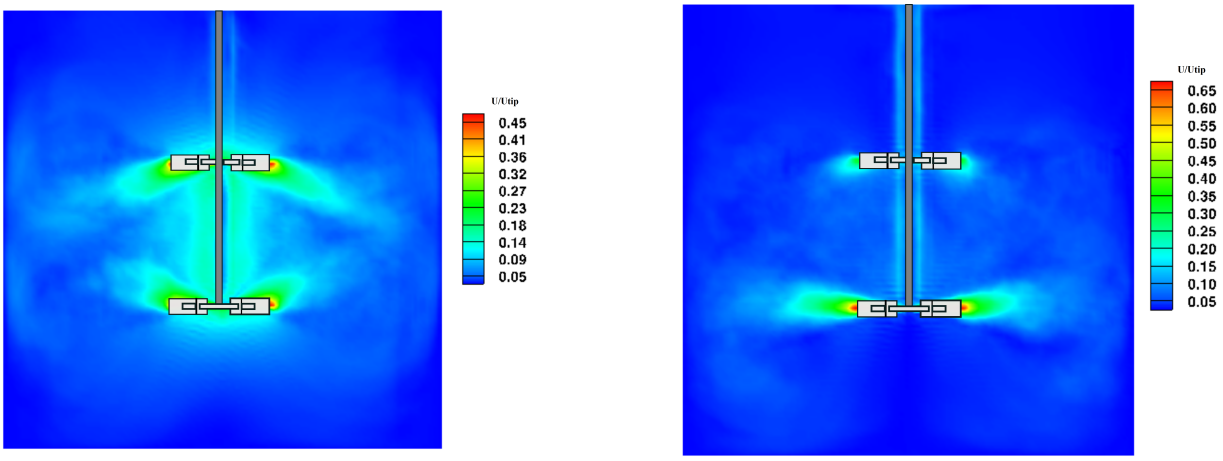

(a) (b)

Figure 5.10 : Phase-averaged velocity magnitude contour at $\theta = 0^{\circ}$ for Case 2: (a) with baffles, (b) without baffles.

without baffles can be chosen over the baffled bioreactor to reduce the material requirement for its manufacturing. Moreover, by reducing the material requirement, the manufacturing cost of the bioreactor also decreases. Figure 5.10 shows the contour plot of phase-averaged velocity magnitude at θ=0° for Case 2. The vortices are mixing in both the cases, with and without baffles. However, the mixing is stronger in the 'with baffles' case than the 'without baffles' one. The stagnant zone is also reduced in this case as compared to the parallel flow i.e. Case 1. However, the stagnant zone is dominant in the case without baffles. Hence, the case with baffles will exhibit better mixing. Figure 5.11 shows the contour plot of phase-averaged velocity magnitude at θ=0° for Case 3 [Agarwal *et al.*, 2021]. The development of vortex can be seen at the bottom having a good spread. It is desirable in terms of mixing. However, the mixing of upper and lower vortices is not observed here. The magnitude of velocity is higher in baffle case but the spread of vortex is better in the latter case. The stagnant zone is reduced as compared to Case 1, especially at the bottom side of the reactor.

Figure 5.12 shows the comparison of axial profiles of phase-averaged radial velocity in a plane midway between baffles at different radial locations for Case 1. The simulation results are compared with the experimental data of Rutherford *et al.* [1996]. The results are in excellent agreement with the experimental data and seem nearly overlapping at all the radial positions considered for the simulations. The effect of baffles is not significant, and the axial velocity profiles for all the radial positions are following the same profile.

Similarly, the comparison of axial profiles of phase-averaged radial velocity in a plane midway between baffles at different radial locations for Case 2 is shown in Figure 5.13. The results are showing a similar trend away from the impellers but near the vicinity of the impeller, the LBM results slightly under predict the experimental measurements. The 'without baffles' case is quite unable to predict the velocity profile, especially near the upper impeller at all the radial positions. The double-peak shape is not exhibited by the simulations without baffles. Figure 5.14 shows the comparison of axial profiles of phase-averaged radial velocity in a plane midway between baffles at different radial locations for Case 3 [Agarwal *et al.*, 2021]. The 'with baffles' simulation cases are slightly over predicting the experimental measurements near the impeller vicinity. The diverging nature of flow at the bottom impeller can be seen with the increasing radial position. Here, the LBM

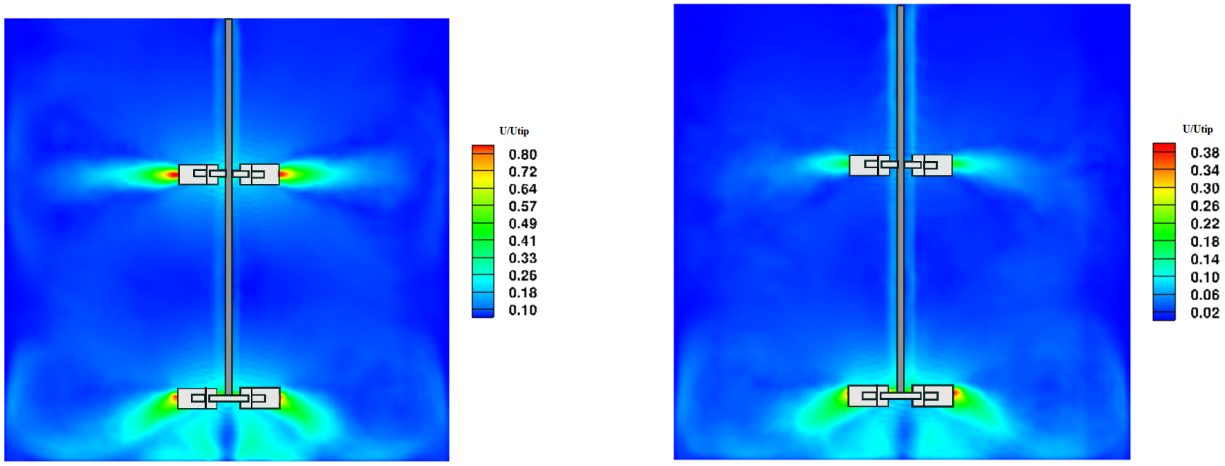

(a) (b)

Figure 5.11 : Phase-averaged velocity magnitude contour at $\theta = 0^{\circ}$ for Case 3: (a) with baffles, (b) without baffles.

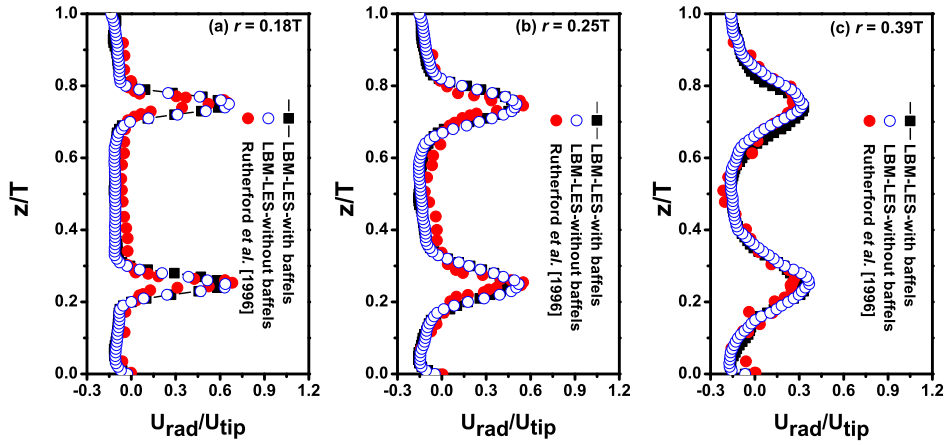

Figure 5.12 : Comparison of axial profiles of phase-averaged radial velocity in a plane midway between baffles at different radial locations for Case 1.

simulations for the 'with baffles' cases are showing better agreement with the experimental data. Additionally, the 'without baffles' case is also simulated for a comparison which shows a lower velocity magnitude at the upper impeller location for all the radial positions. This could be due to the placement of the impellers. The lower impeller of Case 3 is located close to the bottom of the tank, and the distance of the upper impeller from the top of the water level is more comparable to the other two cases (Case 1 and 2). It results in strong swirling flow characteristics for Case 3, and the presence of baffles breaks the swirling flow that leads to increased turbulence at all the radial locations of the upper impeller, resulting in higher velocity magnitude. However, the absence of baffles deteriorates the turbulence level, which in turn decreases the velocity magnitude.

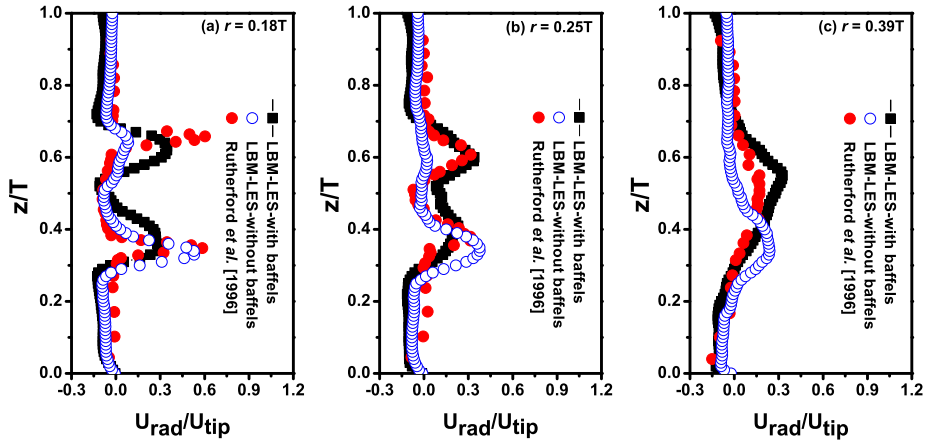

Figure 5.13 : Comparison of axial profiles of phase-averaged radial velocity in a plane midway between baffles at different radial locations for Case 2.

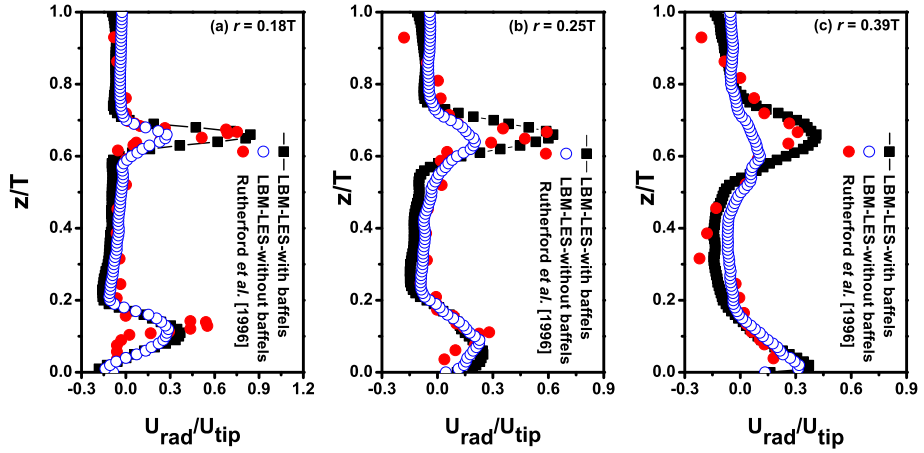

Figure 5.14 : Comparison of axial profiles of phase-averaged radial velocity in a plane midway between baffles at different radial locations for Case 3 [Agarwal *et al.*, 2021].

5.4.3 Turbulent Kinetic Energy

Figure 5.15 shows the comparison of axial profiles of TKE in a plane midway between baffles at different radial locations for Case 1. As shown in Figure 5.15, the kinetic energy is maximum at the impeller tips due to high-velocity magnitude. Both the 'with and without baffles' cases are slightly over-predicting the turbulent kinetic energy compared to the experimental data, especially at the smaller radial position. As the radial position increase, the results match with a relatively lower deviation than before.

Similarly, for Case 2 as shown in Figure 5.16, the double peaks are observed for the baffles case at the radial location close to the impellers. The results are in good comparison with the experimental data. Moreover, the without baffles case under-predicated the turbulent kinetic energy at the upper impeller; however, at the lower impeller, results are slightly over-predicted. Furthermore, at the radial location away from the impellers locations, the with baffles case are in

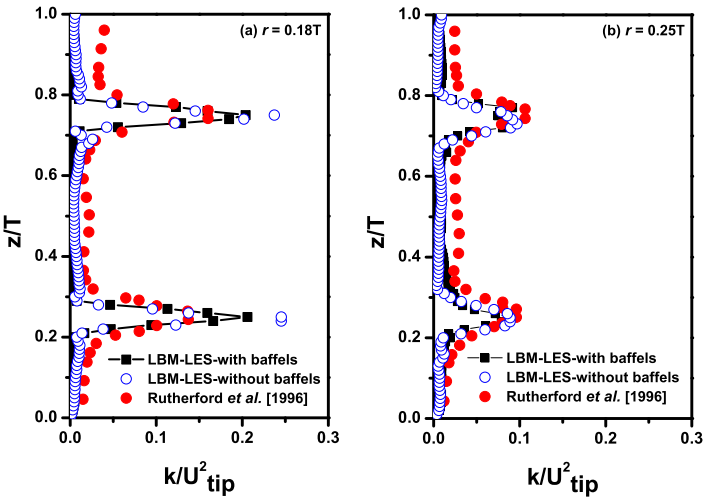

Figure 5.15 : Comparison of axial profiles of turbulent kinetic energy in a plane midway between baffles at different radial locations for Case 1.

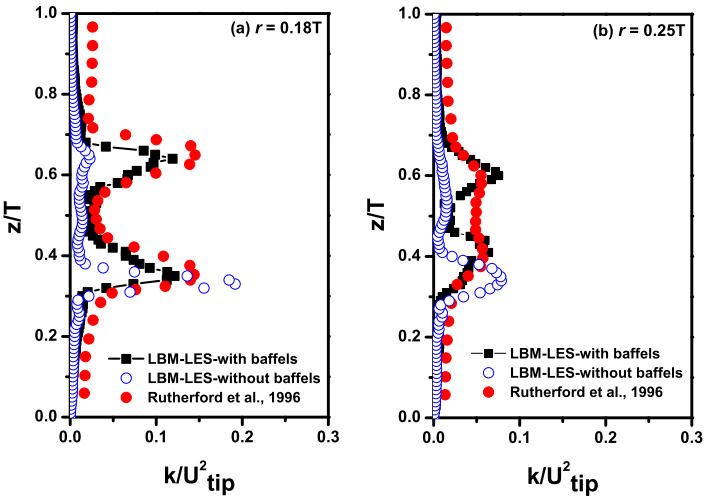

Figure 5.16 : Comparison of axial profiles of turbulent kinetic energy in a plane midway between baffles at different radial locations for Case 2.

close agreement with the experimental results, except in the region between the two impellers, and without baffles case shows similar under-predication at the upper impeller, and a slight shift is observed in the peak at the lower impeller. In Case 3, the double peaks are exhibited near the impellers. However, the simulation results are slightly over-predicting the experimental data, especially near the upper impeller. The without baffles case also shows nearly a similar behavior near the lower impeller, but the turbulent kinetic energy has less magnitude near the upper impeller. Among the three cases, Case 1, i.e., parallel flow, depicts nearly the similar profile of velocity magnitudes and turbulent kinetic energy for both the simulation cases of with and without baffles and are in excellent agreement with the experimental data.

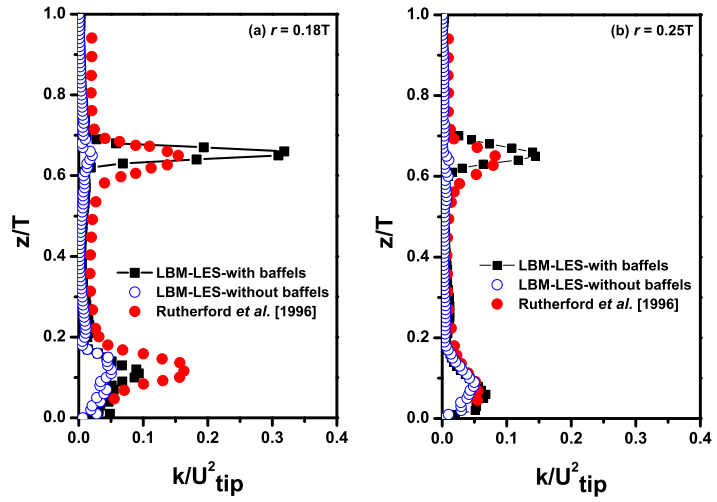

Figure 5.17 : Comparison of axial profiles of turbulent kinetic energy in a plane midway between baffles at different radial locations for Case 3

5.5 SUMMARY

The chapter presented an overall framework to scrutinize the effects of baffles on the flow hydrodynamics of the stirred tank reactor equipped with dual-Rushton turbines at different impeller clearance. The study reported the results for the placement of impellers at different locations along with the presence and absence of baffles in the reactor. The study used LBM as a numerical approach to discretize the fluid domain. LES is used to model the turbulent flow, and small-scale turbulent structures are resolved by the Smagorinsky SGS model. The obtained results are compared and validated with the experimental findings reported in the literature. The results show a good agreement between the reported experimental data and the performed simulations using the LBM-LES model. The results show that in the absence of baffles, the magnitude of instantaneous velocity, phase averaged velocity, and turbulent kinetic energy is less for diverging and merging flow in the absence of baffles. One interesting finding of this study revealed that the presence or absence of baffles does not affect the velocity and turbulent kinetic energy in the parallel flow arrangement. It affirms that the baffled design can be avoided in the case of parallel flow to reduce manufacturing costs and save material. The outcomes presented in this chapter demonstrated that LBM, along with the modeling of turbulent flow past over a stationary object in a closed system, is also suitable to accurately predict the turbulent flow behavior in complex geometry equipped with rotational components.

…

6
Conclusions and Future Recommendations

The research work starts with the objective of validating LBM for LES simulation of turbulent flows in various flow domains. In this direction, the thesis contributes to the effect of boundary conditions and discrete velocity models in LBM and effect of baffles on hydrodynamics of stirred tank reactor. The presented research works also depict the advantage of LBM for solving fluid flow problems compare to other traditional CFD solvers. Moreover, a novel highly parallelized LBM-LES solver has been developed for efficient computation on a multi-threaded GPU platform. This chapter highlights the significant conclusions drawn from the current thesis and suggests the scope of future research work in the relevant field of research.

6.1 CONCLUSIONS

The investigations performed in this thesis are categorized into three sections: A) effect of the discrete velocity model, and B) effect of boundary conditions in LBM on turbulent flow simulation past over a bluff body followed by C) effect of baffles on the flow hydrodynamics of stirred tank reactor. The conclusions from each of these studies are summarized in the following paragraphs

6.1.1 Effect of Discrete Velocity Models

In the first study of the thesis, work has been performed to show the effect of various discrete velocity models on the turbulent flow pass over a bluff body. The different 3D discrete velocity models (i.e., D_3Q_{15}, D_3Q_{19}, and D_3Q_{27}) are taken into consideration. The flow domain used in the study is the benchmark flow problem of flow past a square cylinder confined in a rectangular duct. The obtained results provide information about the accuracy and computational efficiency of each discrete velocity model. The results show that D_3Q_{27} provides better accuracy compared to other discrete velocity models for the simulation of turbulent flow past an obstacle in a closed system. However, the model lags in terms of computational efficiency with other velocity models.

6.1.2 Effect of boundary conditions

In the second study of the thesis, the research work investigates the effect of boundary conditions in LBM on turbulent flow behavior past an obstacle. The study presents a comparative analysis of the modified BB and IB methods used to implement no-slip boundary conditions on the boundary nodes of an obstacle (here, a square cylinder). The results obtained for different turbulent statistics are validated with the existing experimental and other numerical results in the literature and show an excellent agreement against them. However, a slight divergence is observed in all the turbulent parameters at the streamwise location near the downstream face of the cylinder, both for the BB and IB method. Moreover, the results also show that the IB method over-predicted the mean drag coefficient ($\overline{C}_D$) and computationally expensive than the modified BB method.

6.1.3 Effect of baffles on flow hydrodynamics of stirred tank reactor

The thesis further studies the effect of baffles on flow behavior inside the stirred tank reactor. The flow system consists of a stirred tank reactor equipped with 6-blade dual-Rushton impellers. LBM is used to discretize the fluid domain and LES for the modeling of turbulent motions. The influence of cylindrical walls, baffles, and revolving shafts and impellers on the fluid flow is modeled using the IB method. The results are reported for phase averaged velocities and TKE in the presence and absence of baffles. Moreover, the simulations have been performed at three different locations of the placement of impellers on the shaft. The three different locations of the impellers produced three different flow patterns. They can be categorized as parallel flow, merging flow, and diverging flow. The results obtained are well agreed with the experimental data available in the literature. Furthermore, the research finds an interesting fact that in parallel flow, the presence and absence of baffles in the reactor configuration do not impact the flow properties. However, for the other two cases, i.e., merging and diverging flow pattern, the magnitude of both the flow properties, phase-averaged radial velocity, and TKE decrease in the absence of baffles.

6.2 RECOMMENDATIONS FOR FUTURE WORKS

The research work proposed in the present thesis allows formulating future objectives. Some of the recommendations are listed below:

i. The present thesis investigated the viability of the SRT-LBM model for the turbulent flow simulation. The work shows that SRT-LBM can effectively predict the turbulent flow characteristics in various flow domains, like turbulent flow past over a bluff body confined in a closed system and flow behavior in stirred tank reactor. The work can be extended for applications in other fields, where the turbulent flow plays an important role, such as aerospace engineering, chemical engineering, water resource engineering, ocean engineering, and others.

ii. The thesis work presented the results with SRT-LBM. The model works well for the high Reynolds number flows, only when some turbulence model can be incorporated in the frame of LBM. As in the present thesis, the LES model is used with LBM for turbulent flow modeling. However, the SRT-LBM model shows instability for high Reynolds number flows when DNS will be used to model turbulence eddies. Thus, alternative LBM models such as MRT, TRT, and others can be used for turbulent flow simulation to resolve the eddies up to the smallest-length scale with DNS.

iii. In this thesis, a study is reported to show the effect of baffles on the flow hydrodynamics of stirred tank reactors fitted with dual-Rushton impellers. Further, we would like to extend the work for investigating the effect of other reactor components such as blades, impeller geometry, and height to width ratio of the reactor on flow parameters.

iv. The stirred tank reactors are used for a for a broad range of applications including such as mixing, fermentation, polymerization, chemical reaction kinetics, flocculation, and others [Li *et al.*, 2012]. Moreover, the stirred tank reactor performs various operations such as homogenization, blending of miscible liquid, dispersion of gases or immiscible fluids in liquids, heat and mass transfer, suspension of solid particles, etc. And, all these operations are directly influenced by the flow behavior of the fluid inside the reactor [Kerdouss *et al.*, 2006; Escamilla-Ruíz *et al.*, 2017]. E.g., one of the multiple flow-associated processes, mixing, is utterly dependent on the flow behavior of the fluid. However, in the present thesis work, the study has been performed on stirred tank reactor only for the liquid phase hydrodynamics. This work can be extended to simulate multi-physical processes involved in the stirred tank reactor for its optimization and scale-up.for liquid flow hydrodynamics.

...

References

Agarwal, A. (2020), "Modification of On-Site Velocity Boundary Condition in LBM for D3Q27 Lattice Structure", *Transactions of the Indian National Academy of Engineering*, pp. 1–11 2020

Agarwal, A. and Prakash, A. (2018), "Comparative study of boundary conditions in lbm for incompressible laminar flow", *in International conference on mathematical modelling and scientific computation*, pp. 241–251, Springer 2018

Agarwal, A., Singh, G., and Prakash, A. (2021), "Numerical investigation of flow behavior in double-rushton turbine stirred tank bioreactor", *Materials Today: Proceedings* 2021

Agrawal, A., Djenidi, L., and Antonia, R. (2006), "Investigation of flow around a pair of side-by-side square cylinders using the lattice Boltzmann method", *Computers & fluids*, Vol. 35, No. 10, pp. 1093–1107 2006

Aidun, C. K. and Clausen, J. R. (2010a), "Lattice-Boltzmann method for complex flows", *Annual review of fluid mechanics*, Vol. 42, pp. 439–472 2010a

Aidun, C. K. and Clausen, J. R. (2010b), "Lattice-Boltzmann method for complex flows", *Annual Review of Fluid Mechanics*, Vol. 42, pp. 439–472 2010b

An, B., Bergadà, J., Mellibovsky, F., and Sang, W. (2020), "New applications of numerical simulation based on lattice Boltzmann method at high Reynolds numbers", *Computers & Mathematics with Applications*, Vol. 79, No. 6, pp. 1718–1741 2020

Ayranci, I., Machado, M. B., Madej, A. M., Derksen, J. J., Nobes, D. S., and Kresta, S. M. (2012), "Effect of geometry on the mechanisms for off-bottom solids suspension in a stirred tank", *Chemical Engineering Science*, Vol. 79, pp. 163–176 2012

Bakker, R. (1995), "Laser-Doppler measurements in a baffled stirred tank reactor with a disc turbine. Experimental data to appear in his Ph. D", Ph.D. thesis, thesis, Delft University of Technology, the Netherlands 1995

Bartels, C., Breuer, M., Wechsler, K., and Durst, F. (2002), "Computational fluid dynamics applications on parallel-vector computers: computations of stirred vessel flows", *Computers & fluids*, Vol. 31, No. 1, pp. 69–97 2002

Behrend, O. (1995), "Solid-fluid boundaries in particle suspension simulations via the lattice Boltzmann method", *Physical Review E*, Vol. 52, No. 1, p. 1164 1995

Benzi, R. and Succi, S. (1990), "Two-dimensional turbulence with the lattice Boltzmann equation", *Journal of Physics A: Mathematical and General*, Vol. 23, No. 1, p. L1 1990

Benzi, R., Succi, S., and Vergassola, M. (1992), "The lattice Boltzmann equation: theory and applications", *Physics Reports*, Vol. 222, No. 3, pp. 145–197 1992

Bespalko, D. J. (2011), "Validation of the lattice Boltzmann method for direct numerical simulation of wall-bounded turbulent flows", Ph.D. thesis, Queen's University 2011

Bhatnagar, P. L., Gross, E. P., and Krook, M. (1954), "A model for collision processes in gases. I. Small amplitude processes in charged and neutral one-component systems", *Physical Review*, Vol. 94, No. 3, p. 511 1954

Bonvillani, P., Ferrari, M., Ducrós, E., and Orejas, J. (2006), "Theoretical and experimental study of the effects of scale-up on mixing time for a stirred-tank bioreactor", *Brazilian Journal of Chemical Engineering*, Vol. 23, No. 1, pp. 1–7 2006

Broadwell, J. E. (1964), "Study of rarefied shear flow by the discrete velocity method", *Journal of Fluid Mechanics*, Vol. 19, No. 3, pp. 401–414 1964

Chen, S. and Doolen, G. D. (1998), "Lattice Boltzmann method for fluid flows", *Annual Review of Fluid Mechanics*, Vol. 30, No. 1, pp. 329–364 1998

Chen, S., Chen, H., Martnez, D., and Matthaeus, W. (1991), "Lattice Boltzmann model for simulation of magnetohydrodynamics", *Physical Review Letters*, Vol. 67, No. 27, p. 3776 1991

Chen, S., Martinez, D., and Mei, R. (1996), "On boundary conditions in lattice Boltzmann methods", *Physics of fluids*, Vol. 8, No. 9, pp. 2527–2536 1996

Cheng, J., Grossman, M., and McKercher, T., *Professional CUDA c programming*, John Wiley & Sons 2014

Chikatamarla, S., Frouzakis, C., Karlin, I., Tomboulides, A., and Boulouchos, K. (2010), "Lattice Boltzmann method for direct numerical simulation of turbulent flows", *Journal of fluid mechanics*, Vol. 656, pp. 298–308 2010

Chunmei, P., Jian, M., Xinhong, L., and Zhengming, G. (2008), "Investigation of fluid flow in a dual Rushton impeller stirred tank using particle image velocimetry", *Chinese Journal of Chemical Engineering*, Vol. 16, No. 5, pp. 693–699 2008

Cornubert, R., d'Humières, D., and Levermore, D. (1991), "A Knudsen layer theory for lattice gases", *Physica D: Nonlinear Phenomena*, Vol. 47, No. 1-2, pp. 241–259 1991

Deen, N. G., van Sint Annaland, M., and Kuipers, J. (2004), "Multi-scale modeling of dispersed gas–liquid two-phase flow", *Chemical engineering science*, Vol. 59, No. 8-9, pp. 1853–1861 2004

Derksen, J. (2001), "Assessment of large eddy simulations for agitated flows", *Chemical Engineering Research and Design*, Vol. 79, No. 8, pp. 824–830 2001

Derksen, J. and Van den Akker, H. (1998), "Parallel simulation of turbulent fluid flow in a mixing tank", *in International Conference on High-Performance Computing and Networking*, pp. 96–104, Springer 1998

Derksen, J. and Van den Akker, H. E. (1999), "Large eddy simulations on the flow driven by a Rushton turbine", *AIChE Journal*, Vol. 45, No. 2, pp. 209–221 1999

Derksen, J., Kooman, J., and Van den Akker, H. (1997), "Parallel fluid flow simulations by means of a lattice-Boltzmann scheme", *in International Conference on High-Performance Computing and Networking*, pp. 524–530, Springer 1997

Derksen, J., Doelman, M., and Van den Akker, H. (1998), "Three-dimensional phase-resolved LDA experiments in the impeller region of turbulently stirred tank", *in Int. Symp. on Applications of Laser Techniques to Fluid Mechanics*, pp. 233–250 1998

d'Humieres, D. (1994), "Generalized lattice-Boltzmann equations", *Progress in Astronautics and Aeronautics*, Vol. 159, pp. 450–450 1994

d'Humières, D. (2002), "Multiple–relaxation–time lattice Boltzmann models in three dimensions", *Philosophical Transactions of the Royal Society of London A: Mathematical, Physical and Engineering Sciences*, Vol. 360, No. 1792, pp. 437–451 2002

d'Humieres, D., Lallemand, P., and Frisch, U. (1986), "Lattice gas models for 3D hydrodynamics", *EPL (Europhysics Letters)*, Vol. 2, No. 4, p. 291 1986

d'Humières, D., Bouzidi, M., and Lallemand, P. (2001), "Thirteen-velocity three-dimensional lattice Boltzmann model", *Physical Review E*, Vol. 63, No. 6, p. 066702 2001

Eggels, J. and Somers, J. (1995), "Numerical simulation of free convective flow using the lattice-Boltzmann scheme", *International Journal of Heat and Fluid Flow*, Vol. 16, No. 5, pp. 357–364 1995

Eggels, J. G. (1996), "Direct and large-eddy simulation of turbulent fluid flow using the lattice-Boltzmann scheme", *International Journal of Heat and Fluid Flow*, Vol. 17, No. 3, pp. 307–323 1996

Escamilla-Ruíz, I., Sierra-Espinosa, F., García, J., Valera-Medina, A., and Carrillo, F. (2017), "Experimental data and numerical predictions of a single-phase flow in a batch square stirred tank reactor with a rotating cylinder agitator", *Heat and Mass Transfer*, Vol. 53, No. 9, pp. 2933–2949 2017

Fernandino, M., Beronov, K., and Ytrehus, T. (2009), "Large eddy simulation of turbulent open duct flow using a lattice Boltzmann approach", *Mathematics and Computers in Simulation*, Vol. 79, No. 5, pp. 1520–1526 2009

Feuchter, C., Wagner, O., Stief, A., and Beisswenger, T. (2019), "Turbulent flow simulations around a surface-mounted finite cylinder using an entropic multi-relaxation lattice Boltzmann method", *Fluid Dynamics Research*, Vol. 51, No. 5, p. 055509 2019

Frisch, U., Hasslacher, B., and Pomeau, Y. (1986), "Lattice-gas automata for the Navier-Stokes equation", *Physical Review Letters*, Vol. 56, No. 14, p. 1505 1986

Gillissen, J. and Van den Akker, H. (2012), "Direct numerical simulation of the turbulent flow in a baffled tank driven by a Rushton turbine", *AIChE Journal*, Vol. 58, No. 12, pp. 3878–3890 2012

Ginzbourg, I. and Adler, P. (1994), "Boundary flow condition analysis for the three-dimensional lattice Boltzmann model", *Journal de Physique II*, Vol. 4, No. 2, pp. 191–214 1994

Ginzburg, I. and d'Humieres, D. (2003), "Multireflection boundary conditions for lattice Boltzmann models", *Physical Review E*, Vol. 68, No. 6, p. 066614 2003

Ginzburg, I., Verhaeghe, F., and d'Humieres, D. (2008a), "Study of simple hydrodynamic solutions with the two-relaxation-times lattice Boltzmann scheme", *Communications in Computational Physics*, Vol. 3, No. 3, pp. 519–581 2008a

Ginzburg, I., Verhaeghe, F., and d'Humieres, D. (2008b), "Two-relaxation-time lattice Boltzmann scheme: About parametrization, velocity, pressure and mixed boundary conditions", *Communications in Computational Physics*, Vol. 3, No. 2, pp. 427–478 2008b

Grunau, D., Chen, S., and Eggert, K. (1993), "A lattice Boltzmann model for multiphase fluid flows", *Physics of Fluids A: Fluid Dynamics*, Vol. 5, No. 10, pp. 2557–2562 1993

Guide, D. (2013), "Cuda c programming guide", *NVIDIA, July*, Vol. 29, p. 31 2013

Gunstensen, A. K., Rothman, D. H., Zaleski, S., and Zanetti, G. (1991), "Lattice Boltzmann model of immiscible fluids", *Physical Review A*, Vol. 43, No. 8, p. 4320 1991

Guo, Z. and Shu, C., *Lattice Boltzmann method and its applications in engineering*, Vol. 3, World Scientific 2013

Guo, Z., Zheng, C., and Shi, B. (2002), "Discrete lattice effects on the forcing term in the lattice Boltzmann method", *Physical review E*, Vol. 65, No. 4, p. 046308 2002

Hamane, D., Guerri, O., and Larbi, S. (2015), "Investigation of flow around a circular cylinder in laminar and turbulent flow using the Lattice Boltzmann method", *in AIP Conference Proceedings*, Vol. 1648, p. 850094, AIP Publishing LLC 2015

Han-Taw, C. and Jae-Yuh, L. (1993), "Numerical analysis for hyperbolic heat conduction", *International Journal of Heat and Mass Transfer*, Vol. 36, No. 11, pp. 2891–2898 1993

Hardy, J., Pomeau, Y., and De Pazzis, O. (1973), "Time evolution of a two-dimensional classical lattice system", *Physical Review Letters*, Vol. 31, No. 5, p. 276 1973

Hardy, J., De Pazzis, O., and Pomeau, Y. (1976), "Molecular dynamics of a classical lattice gas: Transport properties and time correlation functions", *Physical Review A*, Vol. 13, No. 5, p. 1949 1976

Hartmann, H., Derksen, J., Montavon, C., Pearson, J., Hamill, I., and Van den Akker, H. (2004), "Assessment of large eddy and RANS stirred tank simulations by means of LDA", *Chemical Engineering Science*, Vol. 59, No. 12, pp. 2419–2432 2004

He, X. and Luo, L.-S. (1997), "Theory of the lattice Boltzmann method: From the Boltzmann equation to the lattice Boltzmann equation", *Physical Review E*, Vol. 56, No. 6, p. 6811 1997

Hecht, M. and Harting, J. (2010), "Implementation of on-site velocity boundary conditions for D3Q19 lattice Boltzmann simulations", *Journal of Statistical Mechanics: Theory and Experiment*, Vol. 2010, No. 01, p. P01018 2010

Higuera, F. and Jimenez, J. (1989), "Boltzmann approach to lattice gas simulations", *EPL (Europhysics Letters)*, Vol. 9, No. 7, p. 663 1989

Ho, J.-R., Kuo, C.-P., Jiaung, W.-S., and Twu, C.-J. (2002), "Lattice Boltzmann scheme for hyperbolic heat conduction equation", *Numerical Heat Transfer: Part B: Fundamentals*, Vol. 41, No. 6, pp. 591–607 2002

Hou, S., Sterling, J., Chen, S., and Doolen, G. (1994), "A lattice Boltzmann subgrid model for high Reynolds number flows", *arXiv preprint comp-gas/9401004* 1994

Hou, Y., Angland, D., Sengissen, A., and Scotto, A. (2019), "Lattice-Boltzmann and Navier-Stokes simulations of the partially dressed, cavity-closed nose landing gear benchmark case", *in 25th AIAA/CEAS Aeroacoustics Conference*, p. 2555 2019

Jahanshaloo, L., Pouryazdanpanah, E., and Che Sidik, N. A. (2013), "A review on the application of the lattice Boltzmann method for turbulent flow simulation", *Numerical Heat Transfer, Part A: Applications*, Vol. 64, No. 11, pp. 938–953 2013

Kajzer, A. and Pozorski, J. (2017), "Application of the Lattice Boltzmann Method to the flow past a sphere", *Journal of Theoretical and Applied Mechanics*, Vol. 55, No. 3, pp. 1091–1099 2017

Kang, S. K. and Hassan, Y. A. (2011), "A comparative study of direct-forcing immersed boundary-lattice Boltzmann methods for stationary complex boundaries", *International Journal for Numerical Methods in Fluids*, Vol. 66, No. 9, pp. 1132–1158 2011

Kao, P.-H. and Yang, R.-J. (2008), "An investigation into curved and moving boundary treatments in the lattice Boltzmann method", *Journal of Computational Physics*, Vol. 227, No. 11, pp. 5671–5690 2008

Kellay, H., Wu, X., and Goldburg, W. (1998), "Vorticity measurements in turbulent soap films", *Physical review letters*, Vol. 80, No. 2, p. 277 1998

Kerdouss, F., Bannari, A., and Proulx, P. (2006), "CFD modeling of gas dispersion and bubble size in a double turbine stirred tank", *Chemical Engineering Science*, Vol. 61, No. 10, pp. 3313–3322 2006

Kim, D.-H., Yang, K.-S., and Senda, M. (2004), "Large eddy simulation of turbulent flow past a square cylinder confined in a channel", *Computers & fluids*, Vol. 33, No. 1, pp. 81–96 2004

Kobayashi, H. (2005), "LES of MHD turbulent channel flows with a local SGS model based on coherent structures", *CTR Annual Research Briefs*, p. 235 2005

Koda, Y. and Lien, F.-S. (2015), "The lattice Boltzmann method implemented on the GPU to simulate the turbulent flow over a square cylinder confined in a channel", *Flow, Turbulence and Combustion*, Vol. 94, No. 3, pp. 495–512 2015

Koelman, J. (1991), "A simple lattice Boltzmann scheme for Navier-Stokes fluid flow", *EPL (Europhysics Letters)*, Vol. 15, No. 6, p. 603 1991

Kutay, M. E., Aydilek, A. H., and Masad, E. (2006), "Laboratory validation of lattice Boltzmann method for modeling pore-scale flow in granular materials", *Computers and Geotechnics*, Vol. 33, No. 8, pp. 381–395 2006

Lallemand, P. and Luo, L.-S. (2000), "Theory of the lattice Boltzmann method: Dispersion, dissipation, isotropy, Galilean invariance, and stability", *Physical Review E*, Vol. 61, No. 6, p. 6546 2000

Lallemand, P., d'Humieres, D., Luo, L.-S., and Rubinstein, R. (2003), "Theory of the lattice Boltzmann method: three-dimensional model for linear viscoelastic fluids", *Physical Review E*, Vol. 67, No. 2, p. 021203 2003

Lammers, P., Beronov, K., Volkert, R., Brenner, G., and Durst, F. (2006), "Lattice BGK direct numerical simulation of fully developed turbulence in incompressible plane channel flow", *Computers & fluids*, Vol. 35, No. 10, pp. 1137–1153 2006

Lavallee, P., Boon, J. P., and Noullez, A. (1991), "Boundaries in lattice gas flows", *Physica D: Nonlinear Phenomena*, Vol. 47, No. 1-2, pp. 233–240 1991

Li, Z., Hu, M., Bao, Y., and Gao, Z. (2012), "Particle image velocimetry experiments and large eddy simulations of merging flow characteristics in dual Rushton turbine stirred tanks", *Industrial & engineering chemistry research*, Vol. 51, No. 5, pp. 2438–2450 2012

Lu, Z., Liao, Y., Qian, D., McLaughlin, J., Derksen, J., and Kontomaris, K. (2002), "Large eddy simulations of a stirred tank using the lattice Boltzmann method on a nonuniform grid", *Journal of Computational Physics*, Vol. 181, No. 2, pp. 675–704 2002

Luo, L.-S., Liao, W., Chen, X., Peng, Y., Zhang, W. *et al.* (2011), "Numerics of the lattice Boltzmann method: Effects of collision models on the lattice Boltzmann simulations", *Physical Review E*, Vol. 83, No. 5, p. 056710 2011

Lyn, D. A., Einav, S., Rodi, W., and Park, J.-H. (1995), "A laser-Doppler velocimetry study of ensemble-averaged characteristics of the turbulent near wake of a square cylinder", *Journal of Fluid Mechanics*, Vol. 304, pp. 285–319 1995

Mayer, G. and Házi, G. (2006), "Direct numerical and large eddy simulation of longitudinal flow along triangular array of rods using the lattice Boltzmann method", *Mathematics and Computers in Simulation*, Vol. 72, No. 2-6, pp. 173–178 2006

McNamara, G. R. and Zanetti, G. (1988), "Use of the Boltzmann equation to simulate lattice-gas automata", *Physical Review Letters*, Vol. 61, No. 20, p. 2332 1988

Mei, R., Shyy, W., Yu, D., and Luo, L.-S. (2000), "Lattice Boltzmann method for 3-D flows with curved boundary", *Journal of Computational Physics*, Vol. 161, No. 2, pp. 680–699 2000

Menter, F. R. (1994), "Two-equation eddy-viscosity turbulence models for engineering applications", *AIAA journal*, Vol. 32, No. 8, pp. 1598–1605 1994

Micale, G., Brucato, A., Grisafi, F., and Ciofalo, M. (1999), "Prediction of flow fields in a dual-impeller stirred vessel", *AIChE journal*, Vol. 45, No. 3, pp. 445–464 1999

Mussa, A., Asinari, P., and Luo, L.-S. (2009), "Lattice Boltzmann simulations of 2D laminar flows past two tandem cylinders", *Journal of computational physics*, Vol. 228, No. 4, pp. 983–999 2009

Nakagawa, S., Nitta, K., and Senda, M. (1999), "An experimental study on unsteady turbulent near wake of a rectangular cylinder in channel flow", *Experiments in fluids*, Vol. 27, No. 3, pp. 284–294 1999

Noble, D. R., Chen, S., Georgiadis, J. G., and Buckius, R. O. (1995), "A consistent hydrodynamic boundary condition for the lattice Boltzmann method", *Physics of Fluids*, Vol. 7, No. 1, pp. 203–209 1995

NVIDIA, T. (2016), "P100 white paper", *NVIDIA Corporation* 2016

Pattison, M. J., Premnath, K. N., and Banerjee, S. (2009), "Computation of turbulent flow and secondary motions in a square duct using a forced generalized Lattice Boltzmann equation", *Physical Review E*, Vol. 79, No. 2, p. 026704 2009

Peng, C., Geneva, N., Guo, Z., and Wang, L.-P. (2018), "Direct numerical simulation of turbulent pipe flow using the lattice Boltzmann method", *Journal of Computational Physics*, Vol. 357, pp. 16–42 2018

Peng, Y. and Luo, L.-S. (2008), "A comparative study of immersed-boundary and interpolated bounce-back methods in LBE", *Progress in Computational Fluid Dynamics, an International Journal*, Vol. 8, No. 1-4, pp. 156–167 2008

Perumal, D. A. and Dass, A. K. (2015), "A Review on the development of lattice Boltzmann computation of macro fluid flows and heat transfer", *Alexandria Engineering Journal*, Vol. 54, No. 4, pp. 955–971 2015

Qian, Y. H. (1990), "Lattice gas and lattice kinetic theory applied to the Navier-Stokes equations", Ph.D. thesis 1990

Qian, Y.-H., d'Humières, D., and Lallemand, P. (1992), "Lattice BGK models for Navier-Stokes equation", *EPL (Europhysics Letters)*, Vol. 17, No. 6, p. 479 1992

Raabe, D. (2004), "Overview of the lattice Boltzmann method for nano-and microscale fluid dynamics in materials science and engineering", *Modelling and Simulation in Materials Science and Engineering*, Vol. 12, No. 6, p. R13 2004

Rushton, J. H., Costich, E. W., and Everett, H. J. (1950), "Power characteristics of mixing impellers", *Chemical Engineering Progress*, Vol. 46, No. 8, pp. 395–476 1950

Rutherford, K., Lee, K., Mahmoudi, S., and Yianneskis, M. (1996), "Hydrodynamic characteristics of dual Rushton impeller stirred vessels", *AIChE Journal*, Vol. 42, No. 2, pp. 332–346 1996

Sharma, K. V., Straka, R., and Tavares, F. W. (2019), "Lattice Boltzmann Methods for Industrial Applications", *Industrial & Engineering Chemistry Research*, Vol. 58, No. 36, pp. 16205–16234 2019

Shu, S. and Yang, N. (2018), "GPU-accelerated large eddy simulation of stirred tanks", *Chemical Engineering Science*, Vol. 181, pp. 132–145 2018

Skordos, P. (1993), "Initial and boundary conditions for the lattice Boltzmann method", *Physical*

Review E, Vol. 48, No. 6, p. 4823 1993
Smagorinsky, J. (1963), "General circulation experiments with the primitive equations: I. The basic experiment", *Monthly weather review*, Vol. 91, No. 3, pp. 99–164 1963
Srinivas, Y., Biswas, G., Parihar, A., and Ranjan, R. (2006), "Large-eddy simulation of high Reynolds number turbulent flow past a square cylinder", *Journal of engineering mechanics*, Vol. 132, No. 3, pp. 327–335 2006
Stephen B., P., *Turbulent Flows*, Cambridge University Press 2000
Succi, S., Benzi, R., and Higuera, F. (1991), "The lattice Boltzmann equation: A new tool for computational fluid-dynamics", *Physica D: Nonlinear Phenomena*, Vol. 47, No. 1-2, pp. 219–230 1991
Wang, X., Shangguan, Y., Onodera, N., Kobayashi, H., and Aoki, T. (2014), "Direct numerical simulation and large eddy simulation on a turbulent wall-bounded flow using lattice Boltzmann method and multiple GPUs", *Mathematical Problems in Engineering*, Vol. 2014 2014
Wei, Y.-K. and Hu, X.-Q. (2017), "Two-dimensional simulations of turbulent flow past a row of cylinders using lattice Boltzmann method", *International Journal of Computational Methods*, Vol. 14, No. 01, p. 1750002 2017
Wolfram, S. (1986), "Cellular automaton fluids 1: Basic theory", *Journal of statistical physics*, Vol. 45, No. 3, pp. 471–526 1986
Wu, H. and Patterson, G. (1989), "Laser-Doppler measurements of turbulent-flow parameters in a stirred mixer", *Chemical Engineering Science*, Vol. 44, No. 10, pp. 2207–2221 1989
Xinhong, L., Yuyun, B., Zhipeng, L., Zhengming, G., and Smith, J. M. (2008), "Particle image velocimetry study of turbulence characteristics in a vessel agitated by a dual Rushton impeller", *Chinese Journal of Chemical Engineering*, Vol. 16, No. 5, pp. 700–708 2008
Yasuda, T., Hashimoto, T., Tanno, I., Tanaka, Y., Minagawa, H., Morinishi, K., and Satofuka, N. (2014), "Efficient simulation for incompressible 3-dimensional turbulence flow using lattice Boltzmann model", *in Proceeding of the 8th international conference on computational fluid dynamics (ICCFD8)*, pp. 1661–1668 2014
Yasuda, T., Hashimoto, T., Tanno, I., Tanaka, Y., Minagawa, H., Morinishi, K., and Satofuka, N. (2017), "Effect of collision and velocity model of lattice Boltzmann model on three-dimensional turbulent flow simulation", *International Journal of Computational Fluid Dynamics*, Vol. 31, No. 4-5, pp. 258–268 2017
Zadghaffari, R., Moghaddas, J., and Revstedt, J. (2009), "A mixing study in a double-Rushton stirred tank", *Computers & chemical engineering*, Vol. 33, No. 7, pp. 1240–1246 2009
Ziegler, D. P. (1993), "Boundary conditions for lattice Boltzmann simulations", *Journal of statistical physics*, Vol. 71, No. 5, pp. 1171–1177 1993
Zou, Q. and He, X. (1997), "On pressure and velocity boundary conditions for the lattice Boltzmann BGK model", *Physics of fluids*, Vol. 9, No. 6, pp. 1591–1598 1997

Appendix A: Knowledge Dissemination

The following journals/book chapters/conference proceedings had been published from this thesis so far:

A1 INTERNATIONAL JOURNAL

1. Agarwal, A., Singh, G., and Prakash, A. (2021). Effect of baffles on the flow hydrodynamics of dual-Rushton turbine stirred tank bioreactor—a CFD study. *Brazilian Journal of Chemical Engineering*, 38(4), 849-863.

2. Agarwal, A., Gupta, S., and Prakash, A. (2021). A comparative study of three-dimensional discrete velocity set in LBM for turbulent flow over bluff body. *Journal of the Brazilian Society of Mechanical Sciences and Engineering*, 43(1), 1-11.

3. Agarwal, A. (2020). Modification of On-Site Velocity Boundary Condition in LBM for D_3Q_{27} Lattice Structure. *Transactions of the Indian National Academy of Engineering*, 1-11.

4. Agarwal, A., Gupta, S., and Prakash, A. (2020). A comparative study of bounce-back and immersed boundary method in LBM for turbulent flow simulation.*Materials Today: Proceedings*, 28, 2387-2392.

5. Agarwal, A., Singh, G., and Prakash, A. (2021). Numerical investigation of flow behavior in double-rushton turbine stirred tank bioreactor. *Materials Today: Proceedings*, 43, 51-57.

A2 BOOK CHAPTER

1. Agarwal, A., and Prakash, A. (2018). Comparative study of boundary conditions in LBM for incompressible laminar flow. In *Mathematical Modelling and Scientific Computing with Applications* (pp. 241-251). Springer, Singapore.

A3 CONFERENCE PROCEEDINGS

1. Agarwal, A., and Prakash , A. (2018). LBM-LES Simulation of Flow Past a Square Cylinder Confined in a Duct using GPU Parallel Computing. In *FMFP-2018, IIT Bombay conference proceeding*

2. Agarwal, A., and Prakash, A. (2016). Validation of LBM based on BGK on Poiseuille's Flow and Vortex Street in a Channel Flow. In *ACSM-2016, Bangkok conference proceeding*

A4 SOLVER DEVELOPMENT

1. Agarwal, A., B. Ravindra, and Prakash, A. **"CuLB-LES**: A GPU Parallelized Lattice Boltzmann Solver for Turbulent Flow Simulation (Documents Submitted to R&D IIT Jodhpur for Copyright-Approved in IIPMG Meeting)

Appendix B: Grid Independence Study

B1 TURBULENT FLOW OVER BLUFF BODY

To demonstrate the effect of different grid sizes on the benchmark case of turbulent flow over a bluff body. The simulations are carried out using the D_3Q_{19} discrete velocity model of LBM on two different grid sizes: $800 \times 200 \times 120$ and $1000 \times 200 \times 200$. The results for mean streamwise velocity, RMS streamwise velocity fluctuations, and Reynolds shear stress are presented.

As shown in Figures B1 and B2, the results obtained from a fine mesh of $1000 \times 200 \times 200$ for the mean streamwise velocity near the downstream face of the cylinder agree with the experimental results of Nakagawa *et al.* [1999] and the simulation results of Kim *et al.* [2004] better than the results obtained from a grid size of $800 \times 200 \times 120$. The same is discussed in the explanation of Figure 4.3, that finer mesh is expected to produce more accurate results near the downstream face of the cylinder.

Other results also show a similar pattern. The profiles of RMS streamwise velocity fluctuations and Reynolds shear stress (see Figure B3 and B4) show that near the downstream face of the cylinder, results obtained from fine mesh are in better agreement, but far from the downstream face of the cylinder, grid size has a negligible impact.

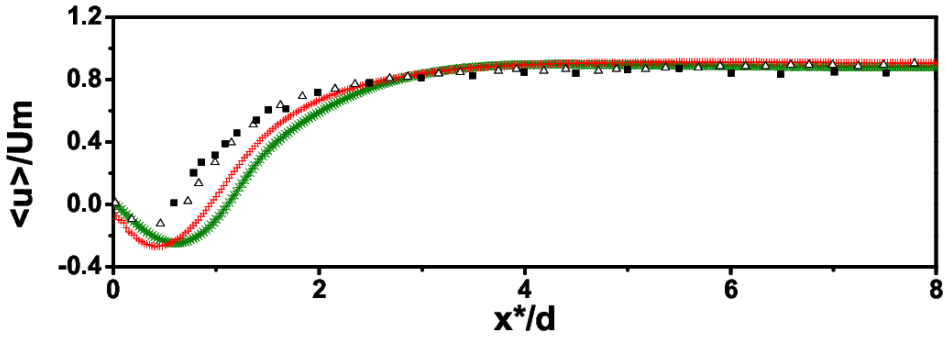

Figure B1 : Centerline distribution of mean streamwise velocity at different grid size (red plus : $1000 \times 200 \times 200$, green asterisk : $800 \times 200 \times 120$, open triangle : Kim *et al.* [2004], filled square: Nakagawa *et al.* [1999]).

B2 FLUID FLOW SIMULATION IN STIRRED TANK REACTOR

The preliminary results for axial profiles of phase-averaged radial velocity at different radial locations for Case 1 (i.e. parallel flow) for both baffles and without baffles are shown in Figure B5. The results depicted approximately similar results for 150^3 and 200^3 grid size and are in good agreement with the experimental data. However, the coarser grid size 100^3 under-predicted the results.

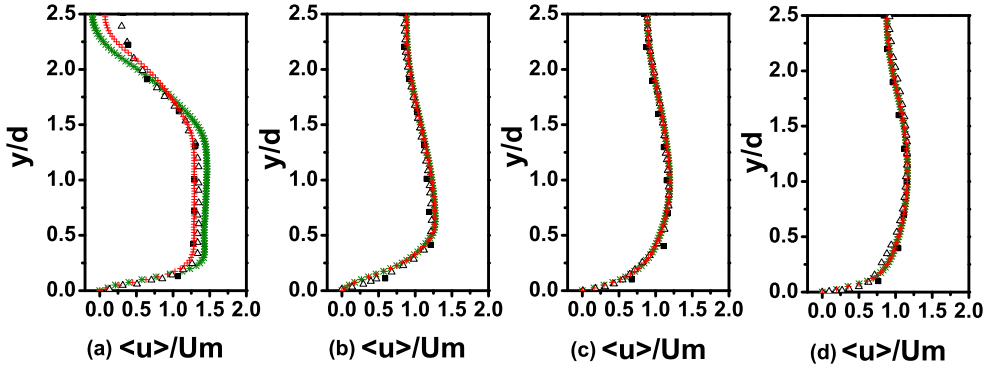

Figure B2 : Profiles of mean streamwise velocity at different grid size (red plus : $1000 \times 200 \times 200$, green asterisk : $800 \times 200 \times 120$, open triangle : Kim *et al.* [2004], filled square: Nakagawa *et al.* [1999]) : (a) x^*/d = 1.0, (b) x^*/d = 3.5, (c) x^*/d = 6.0, (d) x^*/d = 8.5.

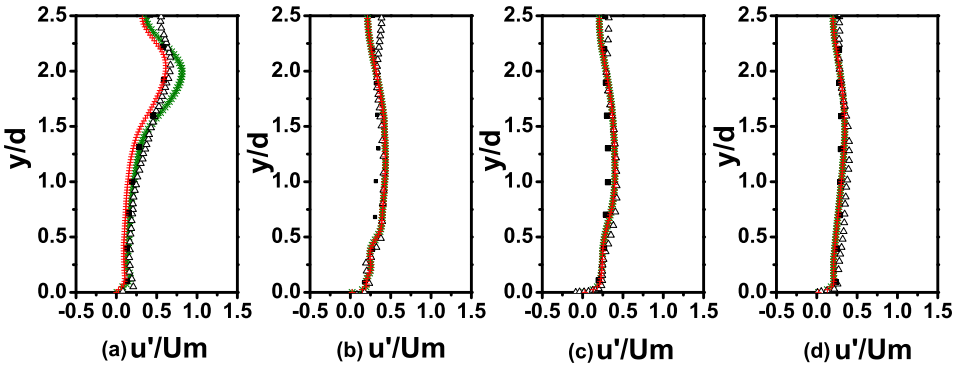

Figure B3 : Profiles of RMS streamwise velocity fluctuations at different grid size (red plus : $1000 \times 200 \times 200$, green asterisk : $800 \times 200 \times 120$, open triangle : Kim *et al.* [2004], filled square: Nakagawa *et al.* [1999]) : (a) x^*/d = 1.0, (b) x^*/d = 3.5, (c) x^*/d = 6.0, (d) x^*/d = 8.5.

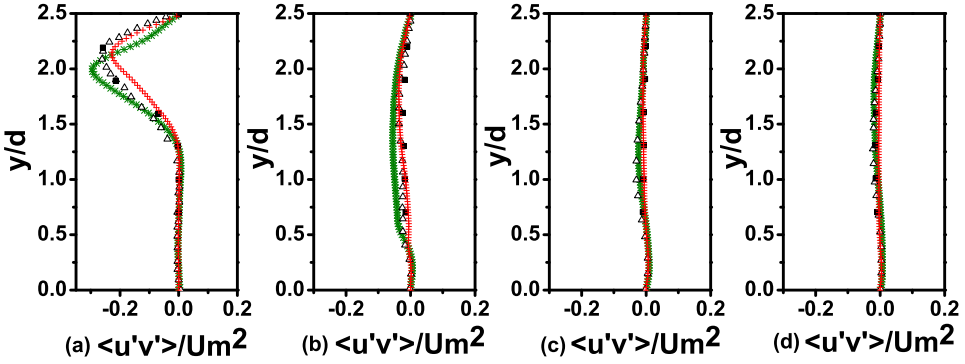

Figure B4 : Profiles of Reynolds shear stress at different grid size (red plus : $1000 \times 200 \times 200$, green asterisk : $800 \times 200 \times 120$, open triangle : Kim *et al.* [2004], filled square: Nakagawa *et al.* [1999]) : (a) x^*/d = 1.0, (b) x^*/d = 3.5, (c) x^*/d = 6.0, (d) x^*/d = 8.5.

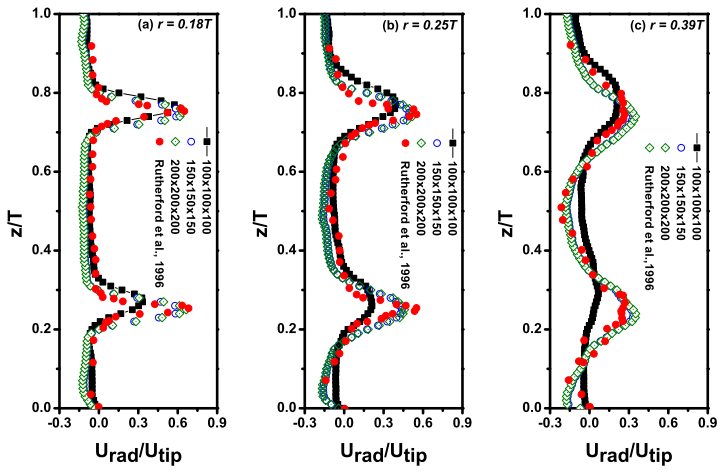

(a)

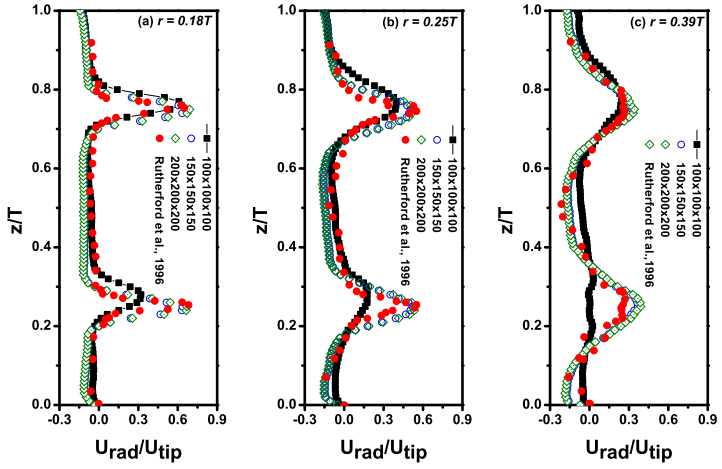

(b)

Figure B5 : Comparison of axial profiles of phase-averaged radial velocity at different radial locations for Case 1 at different grid sizes a) with baffles, and b) without baffles.